Politecnico di Bari

Repository Istituzionale dei Prodotti della Ricerca del Politecnico di Bari

Hybrid laser welding of stainless and high strength steels

This is a PhD Thesis

Original Citation:
Hybrid laser welding of stainless and high strength steels / Perulli, Patrizia. - (2020). [10.60576/poliba/iris/perulli-patrizia_phd2020]

Availability:
This version is available at http://hdl.handle.net/11589/189333 since: 2020-01-15

Published version
DOI:10.60576/poliba/iris/perulli-patrizia_phd2020

Publisher: Politecnico di Bari

Terms of use:

(Article begins on next page)

23 June 2026

Department of Mechanics, Mathematics and Management
MECHANICAL AND MANAGEMENT ENGINEERING
Ph.D. Program
SSD: ING-IND/16– Manufacturing technology and systems

Final Dissertation

Hybrid laser welding of stainless and high strength steels

---

by
Perulli Patrizia

Supervisors:

Prof. Giuseppe Casalino

Prof.ssa Paola Leo

Coordinator of Ph.D. Program:
Prof. Giuseppe Pompeo Demelio

Course n°32, 01/11/2016-31/10/2019

Politecnico di Bari

Department of Mechanics, Mathematics and Management
MECHANICAL AND MANAGEMENT ENGINEERING
Ph.D. Program
SSD: ING-IND/16– Manufacturing technology and systems

Final Dissertation

Hybrid laser welding of stainless and high strength steels

by

Perulli Patrizia :

Perulli Patrizia

Referees:

Prof. Fabrizia Caiazzo

Prof. Antonello Astarita

Supervisors:

Prof. Giuseppe Casalino

Prof.ssa Paola Leo

Coordinator of Ph.D. Program:

Prof. Giuseppe Pompeo Demelio

Course n°32, 01/11/2016-31/10/2019

INDEX

FIGURES

TABLES

NOMENCLATURE

Symbol	Reference	Unit
BPP	Beam parameter product	mm*mrad
Q_{laser}	Laser line energy	J/mm
Q_{arc}	Arc line energy	J/mm
LZ	Laser Zone	-
CZ	Crown Zone	-
DCZ	Depth of Crown Zone	-
DLZ	Depth of Laser Zone	-
σ_y	Yield stress	MPa
ε_{max}	Elongation	%
UTS	Ultimate Tensile Strength	MPa
IMC	Intermetallic compounds	-
E	Young module	GPa
A	Elongation	%
LOW	Laser Offset Welding	-
SFE	Stacking Fault Energy	mJm^{-2}
K	Thermal conductivity	W/mK
T_l	Liquidus Temperature	K
T_s	Solidus Temperature	K
q	Power density	W/m^3
T	Temperature	K
h	Heat transfer coefficient	W/m^2K
r_u	Conical heat source upper radius	m
r_i	Conical heat source lower radius	m
I	Arc current	A
η_a	Arc heat efficiency	-
c	Specific heat	$Jkg^{-1}°C^{-1}$
a_r	Double-ellipsoidal rear length	m
a_f	Double-ellipsoidal front length	m
b	Width double-ellipsoidal	m
d	Depth double-ellipsoidal	m
v	Welding speed	ms^{-1}
Q	Arc power	W
U	Arc voltage	V
f_f	Coefficient at front ellipsoid	-
f_r	Coefficient rear ellipsoid	-
ρ	Density	kg/m^3
σ	Stefan–Boltzmann constant	$Wm^{-2}K^{-4}$
ε	Emissivity	-
$\Delta\varepsilon^E$	Elastic strain	-
$\Delta\varepsilon^P$	Plastic strain	-
$\Delta\varepsilon^T$	Thermal strain	-
WCZ	Width of Crown Zone	-
DCZ	Depth of Crown Zone	-
DLZ	Depth of Laser Zone	-
WCZ	Width of Crown Zone	-

ABSTRACT

In manufactory industry, welding is a joining technology with noticeable properties. Among fusion welding technologies, laser welding employs high power laser beam with high density. Laser beam welding debuted several decades later, after the invention of the laser in 1960, and has demonstrated to be especially useful in high-speed, automated welding

The laser beam produces a reduced melting zone, which has always been seen positive for the industrial products. Low thermal distortion, high speed and little heat input per unit of volume can be reached by fiber laser with some limitations like crack susceptibility, porosity, strict tolerances for edges preparation, and high reflectivity [1-3]. Hybrid laser arc welding can overcome some of those limitations since its tendency to flexibility, low crack formation and porosity, high precision, narrow melting zones, high cooling and heating speeds, deep penetration [1, 4]. Mixing and diffusion phenomena can be controlled and that reduces the formation of intermetallic compounds in the case of dissimilar joints. In fact, dissimilar metal welding implicates joining two different metals or alloys by melting, which the addition of filler metal as an option. Among dissimilar metal weld, aluminum/steel (Al/Fe), advanced high strength steel (AHSSs) /austenitic stainless steel have increased the attention from aeronautical and automotive industry because of the properties such as reduced weight, good formability, high mechanical strength, and more [5, 6]. Dissimilar joining of hybrid Al-Fe structures is often challenging because of the inevitable formation of brittle intermetallic compounds (IMCs), which can compromise the mechanical properties of the weld due to their poor ductility. Therefore, it is necessary to limit their formation to obtain good quality welds.

The major goal of this thesis is to analyze the microstructural and mechanical aspects of dissimilar joints used in the automotive industry, which were welded by different laser techniques. Particularly, great importance was given to the microstructure of the fuse (FZ) and heat affect zones (HAZ), being those zones mainly associated to the mechanical behavior of the weld. The mechanical and microstructural aspect of the joint were related with the process parameters to study the defects and to obtain the better mechanical properties.

After the state-of-art on fusion welding processes, the research activity concerned the study of the fiber laser/TIG weldability of AISI 304 and AISI 410 stainless steel (SS), weldability of Twinning-induced plasticity steels (TWIP) and Dual Phase (DP) steel dissimilar joint by laser arc hybrid welding with austenitic filler and finally the assessment of weldability of TWIP and DP steels with AISI 316 stainless steel. Since the automotive industry has been reducing the vehicle weight and fuel consumption, advanced high strength steels and stainless steel can be help to this achievement.

Research activity concerned also the study of the laser welding of the annealed alloy AA5754 with austenitic stainless steel AISI 316. Particularly, the laser off-set welding (LOW) was used to limit the formation of brittle intermetallic compounds during the welding process. The laser beam was directed onto the stainless steel side of the butt weld at a small distance from the edge of the aluminum sheet. The keyhole formed and the full penetration was reached in the SS side of the weld. Thin layer of intermetallic compounds of different stoichiometry was found at the interfaces between SS and Al fusion zone (FZ).
Finite Element (FE) analysis was employed to evaluate both the temperature distribution, residual stress and distortions in the joints. Using Simufact commercial software, the numerical model of the joint was created and validated through the available experimental data. The target of this part of the research was to build a methodology to build a numerical model for laser and hybrid welding process, with a particular attention to the set-up of the heat source model [7].

1. CHAPTER: Laser-arc Hybrid welding of steels

1.1. Technology of Laser Welding

Welding is one of the most advantageous joining methods applicable in every industrial field. Laser, Light Amplification by Stimulated Emission of Radiation, is a high-power density heat source that has had increasingly success in many human field activities. Laser welding is mainly used for joining metals with a laser beam of high-energy density [1]. The advantages of this technology compared with other process are high quality and low distortion of joints, high precision, high performance, narrow heat affect zone (HAZ), high speed and good flexibility [14, 8]. The laser process in the automotive component manufacture covers engine parts, transmission parts, alternators, solenoids, fuel injectors, fuel filters, air conditioning equipment and air bags. For these applications, the advantage of laser welding is the ability to weld pre-machined precision components with limited heat input and negligible distortion [9]. This enables reducing vehicle weight and, consequently, fuel consumption. Moreover, this process shows good repeatability and it is easy to automate.

Laser welding has also some advantages respect to electron beam welding [10]. This is due mainly to the high productivity, the possibility of control of quality of the component during the process and consequently reducing the manufacturing cost [11, 12]. However, there is a need to spend a high amount of energy on component preparation and a high precision of component manipulation [13].

1.1.1. Fundamental principles of the laser device

Laser is the acronym of Light Amplification by Stimulated Emission of Radiation, in opposition to sunlight, which is emitted spontaneously. The term “laser light” represents a part of the electromagnetic spectrum of energy, although the laser source does not always emit visible electromagnetic radiation, as it may range from ultraviolet to infrared radiations [14].

It is important, to describe the physical principle on which lasers is based. Atoms and molecules possess certain energy levels that are discrete. In general, when electron jumps from a higher energy level to a lower energy level, it emits photon (particle of light). The lowest possible energy level is known as “fundamental state,” while higher energy levels are called the excited states [15, 16]. There are three ways in which a photon can interact with atoms: absorption, spontaneous emission, and amplification (Fig. 1).

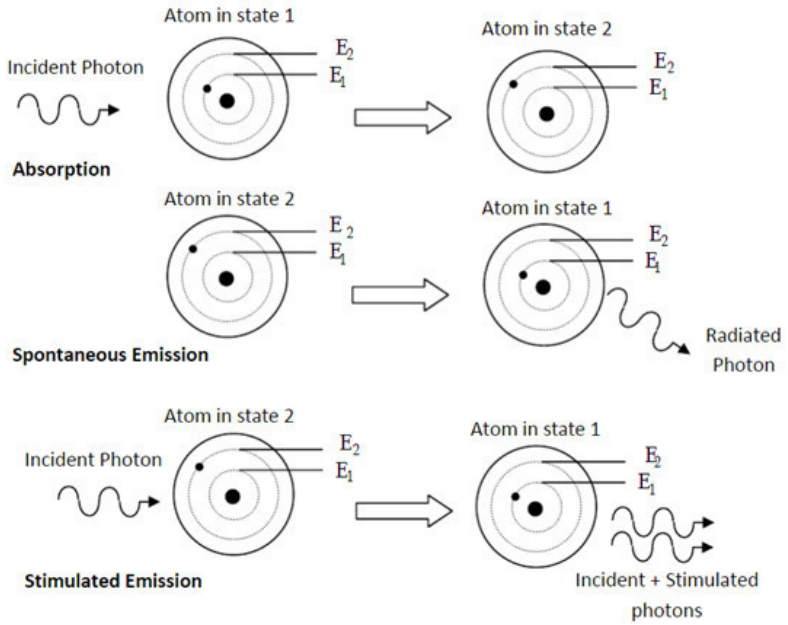

Fig. 1 *Representation for Absorption, Spontaneous and Stimulated Emission [16].*

The laser consists, as simplified presentation, of a chamber containing the active medium, an excitation source (for example high powered flash lamp or electrical current) and two mirrors [17] as shown in Fig. 2.

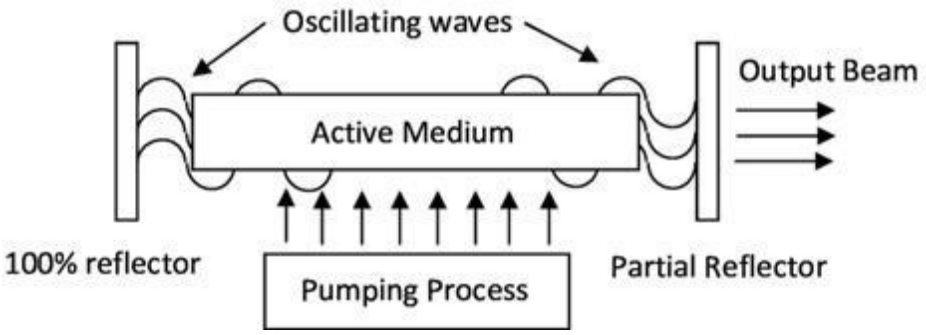

Fig. 2 *Schematic representation of a basic laser [16].*

The chamber (see Fig. 2) comprises two parallel mirrors on each side, one of which is fully reflective and the other only partial reflective. Within this chamber, the active medium, can be a solid, liquid, or gas that defines the wavelength produced by the laser.

Initially, the active medium's electron absorbs a certain amount of energy from the electromagnetic waves, causing the jump of the electrons in the higher energy level (Fig. 1).

Atoms or molecule can only stay in an excited level for a short time, so the excited electrons return to their fundamental state releasing energy, equal to the difference between the two energy levels, in form of photon. This emission of photons is incoherent and occurs in all directions. This is the spontaneous

emission process. This process is typical of light observed in nature. When the photon collides an atom or molecule in the state already excited, it can stimulate the return to the low energy level and the emission of a new photon. In this process, the emission is called stimulated. The photon has the same energy, frequency, and direction of the excited atom, which is a fundamental property of the laser light.

However, if the higher energy level has atoms in greater quantity than the lower energy state, the light in the system undergoes a net increase in intensity. This a condition for the generation of laser light within an optical chamber. A system of mirrors can accelerate the stimulated emission and facilitates the amplification phase through multiple reflections (see Fig. 2).

1.1.1.1. Properties of laser beam

A generic light source, as the sun or a filament lamp, produces incoherent emission of light characterized by variable wavelengths, while the beam generating from the laser source has properties that distinguish it from a common heat source. The monochromaticity is the fundamental property of laser beam that is the radiations have all the same wavelength. Coherency is another important property of laser. All the electromagnetic waves are in the same phase, while the ordinary light source emit light in every direction due to the irregular spontaneous emission. Laser emits light with small divergence angle. This small divergence property is due to a high collimated beam, which means that the laser light doesn't lose its intensity at a distance. This property describes the directionality of laser beam. This is a direct consequence of the fact that the resonant cavity permits only the propagation of the waves along the optical axis.

It is important to analyze a parameter of the laser beam, that is, the so called "transverse mode". The transverse mode gives information of the power distribution in the transverse section of the beam. Moreover, the transversal oscillation mode within the cavity of the laser are precisely described by TEM (Transverse Electric and Magnetic Modes). The power distribution is Gaussian type when a laser beam will have TEM_{00} transient oscillation mode type. Particularly in Fig. 3. different types of transverse mode are showed. In the case of laser welding, however, several oscillation modes can be used in addition to TEM_{00}.

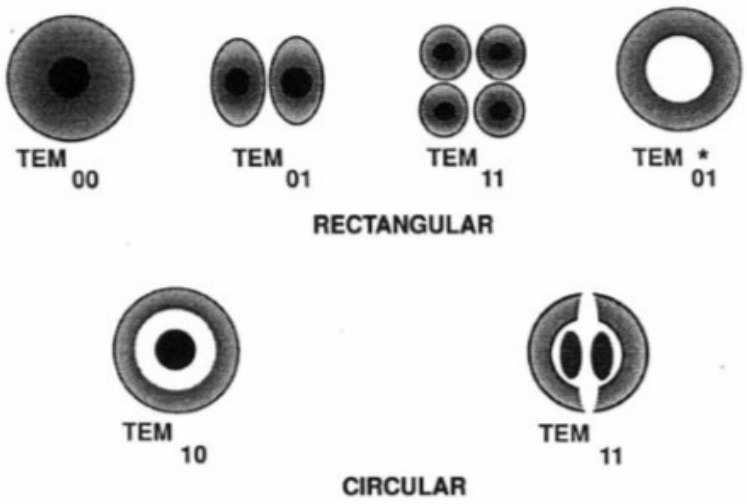

Fig. 3 *Mode patterns [18].*

Laser beam quality is quantified by the beam parameter product (BPP), it follows that the higher the beam parameter product, the lower is the beam quality. The BPP of a laser beam is determined as the product of beam radius, measured at the beam waist, and the beam divergence half-angle, measured in the far field. BPP of actual and non-Gaussian beam is greater than that of the Gaussian beam. Therefore, the beam propagation ratio M^2 is often used as a relative measure of laser beam quality; it is defined as the ratio between a BPP of the real beam and a BPP of an ideal Gaussian beam at the same wavelength. For the Gaussian beam, M^2 is one, whereas real beams are characterized by $M^2 > 1$. The value of parameter M^2 for a laser beam depends on the laser type [18, 19].

1.1.1.2. Laser source

On industrial scale, the laser can have two different operating modes: Continuous Wave laser (CW) and Pulsed Wave laser (PW). In the former, the source releases the laser beam with a constant power value over time, since the photon pumping process is continuous. In the latter, the pumping occurs at very rapid regular interval (see Fig. 4).

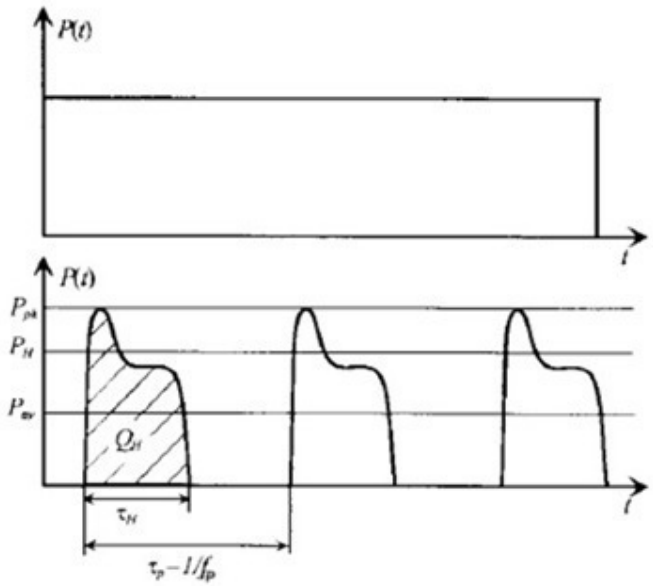

Fig. 4 *Continuous Wave laser (CW) and Pulsed Wave laser mode [17].*

Lasers are classified into different types based on the type of laser medium employed: solid, gaseous and semiconductor. The different type of medium defines the specific energetic source of the pumping. The Table in Fig. 5 show the different types of laser for welding.

Types of laser	Laser characteristics
CO_2 laser	Wavelength: 10.6 μm; far-infrared ray Laser media: CO_2-N_2-He mixed gas (gas) Average power [CW]: 50 kW (Maximum) (Normal): 1–15 kW
Lamp-pumped YAG laser	Wavelength: 1.06 μm; near-infrared ray Laser media: Nd^{3+}:$Y_3Al_5O_{12}$ garnet (solid) Average power [CW]: 10 kW (cascade-type max & fiber-coupling max) (Normal): 50 W–7 kW (Efficiency: 1–4%)
Laser diode (LD)	Wavelength: 0.8–1.1 μm; near-infrared ray Laser media: InGaAsP, etc. (solid) Average power [CW]: 10 kW (stack-type max.), 15 kW (fiber-delivery max.) Merits: Compact, and high efficiency (20–60%)
LD-pumped solid-state laser	Wavelength: about 1 μm; near-infrared ray Laser media: Nd^{3+}:$Y_3Al_5O_{12}$ garnet (solid), etc. Average power [CW]: 13.5 kW (fiber-coupling max.) [PW]: 6 kW (slab-type max.)
Disk laser	Wavelength: 1.03 μm; near-infrared ray Laser media: Yb^{3+}:YAG or YVO_4 (solid), etc. Average power [CW]: 16 kW (cascade-type Max.) Merits: Fiber delivery, high brightness, high efficiency (15–25%)
Fiber laser	Wavelength: 1.07 μm; near-infrared ray Laser media: Yb^{3+}:SiO_2 (solid), etc. Average power [CW]: 100 kW (fiber-coupling max.) Merits: Fiber delivery, high brightness, high efficiency (20–30%)

Fig. 5 *Types and characteristics of laser [19].*

Two of the most popular industrial lasers are Carbon Dioxide lasers (CO_2) and Nd:YAG lasers. The CO_2 laser is a molecular gas laser based on a gas mixture which contains carbon dioxide (CO_2), helium (He), nitrogen (N_2). In CO_2 laser, the wavelength is 10.6 μm long and the energy required for pumping is

provided by direct (DC) or alternating (AC) electric discharges. The output power can reach 20 kW in continuous mode and 10 MW in impulse mode. This type of laser is commonly used for welding steels or for high-grade metals. The main disadvantage in CO_2 laser welding is the long wavelength of the laser beam. Other problems of this type of laser are high reflectivity onto metals and the expensive materials, which are essential for the optics.

The Nd:YAG laser is a solid-state laser in which the medium is made of a neodymium ions (N_d) present in small concentrations in the YAG (Yttrium-Aluminum Garnet, $Y_3Al_5O_{12}$) crystal. When the crystal is activated by N_d ions, the excitation is then executed by flash lamps that pump the photon. Nd:YAG lasers emit typically light at mid-infrared wavelength (1.06 μm). The shorter wavelength offers some important advantages in the industrial applications as the beam can be carried out through optical fibers and focused with ordinary lenses [4].

The power can range from approximately 100 W to over 5 kW in continuous wave. In the pulsed range, it is capable of pulse durations from 15μs to >20ms, peak powers up to 18kW and pulse energies up to 100J (ideal for the complete range of laser processing applications).

For a long time, high-power diode laser (HPDL) systems were limited to low output powers and low beam qualities. In HPDL, their resultant focal intensities only permitted welding applications in the heat conduction mode. Nowadays, thanks to the continuous progress in the laser beam power and beam quality let to HPDLs that can be used also in keyhole mode [4].

For this laser, the beam quality is like that that of Nd:YAG laser. The produced wavelength of HPDL depends on the material properties of the semiconductor, the temperature and the driving current. HPDL systems are particularly suitable in robotic industrial for their compact size and low weight.

Most recently, promising disc and fiber laser systems as special types of diode-pumped solid-state lasers with characteristic geometries of the laser active medium (disc and fiber, respectively) have been developed. Fiber lasers (FL) and the disc laser (DL) have the potential to be a disruptive technology as compared to existing industrial laser technology. These lasers simultaneously offer high optical output powers, high conversion efficiencies, high beam qualities and a short emission wavelength around 1 μm, (see Table in Fig. 6).

	CO_2 laser	Nd:YAG laser (lamp-pumped)	Nd:YAG laser (diode-pumped)	Disc laser	Fibre laser	Diode laser (fibre-coupled)
Lasing medium	Gas mixture	Crystalline rod	Crystalline rod	Crystalline disc	Doped fibre	Semiconductor
Emitted wavelength (μm)	10.6	1.06	1.06	1.03	1.07	0.808–0.98
Power efficiency (%)	10–15	1–3	10–30	10–20	20–30	35–55
Maximum output power (kW)	20	6	6	8	50	8
BPP at 4 kW (mm mrad)	4	25	12	2	0.35	44
M^2 at 4 kW	1.2	75	35	6	1.1	150
Fibre beam delivery	No	Yes	Yes	Yes	Yes	Yes
Typical fibre diameter at 4 kW (mm)	–	0.6	0.4	0.1–0.2	0.03–0.1	0.4
Mobility	low	low	low	low	high	high
Maintenance interval (h)	1000	500	10 000	>25 000	>30 000	>25 000

Fig. 6 *Feature for typical materials processing laser sources [4].*

There are several advantages of fiber and disc lasers compared to other welding technology [4, 20-22]. These lasers exhibit a stable power, mode and pulse shape, high efficiency and roughness. Moreover, disc and fiber lasers are progressively requested for several welding purpose [4].
Usually is used the diode-pumped laser-active medium Yb:YAG with a laser wavelength of 1.03 μm. Fiber laser multimode systems provide high power as up to 50 kW, single-mode fiber lasers are today available up to 5 kW. The active gain medium of fiber laser is usually an optical fiber doped with Yb with wavelengths in the range 1.06 to 1.07 μm.
Generally, each industrial application needs to be evaluated for determining what is the best laser, which depends on wavelength, peak power, pulse length, flexibility, BPP, initial cost, operating cost, etc.

1.1.2. Welding mechanism: conduction mode and keyhole mode

Conduction mode and keyhole mode are two types of heating utilized to represent the resulting melting of the metal during laser welding process. These welding modes are due to different power densities, which are defined as the power of the laser beam divided by the area of the focused laser spot. During conduction joining the laser beam is focused to give a power density on the order of 10^3 Wmm^{-2}. Conduction mode is used to create a joint without vaporization. In conduction mode welding, weld penetration is reached by the heat of the laser conducting down into the metal from the surface are usually wider than deeper [17, 19, 23].
In keyhole welding, the laser beam is focused with a high-power density onto the component surface, which vaporizes (i.e. the power density, for steel, is about 10^6 Wmm^{-2}). In the keyhole mode, a narrow deep vapor cavity or keyhole is developed both by recoil pressure due to the evaporation and by multiple internal reflection of the beam. The keyhole is surrounded by fusion material and it is preserved during welding process by equilibrium between the forces produced by vapor pressure and those applied by the surrounding melted material. In that welding condition, a narrow weld with a high aspect ratio (defined as the ratio between depth and width) is obtained [24-26]. During the keyhole formation, the laser absorption is extremely high due to multi-reflection inwards, so deep penetration welding is considered as an efficient joining process.
A bright plume of evaporated metallic atoms and vapors is expelled from laser-irradiated part. Spattering of melt metal due to a strong stream of the ejected plume can happen from the inlet of the keyhole [27, 28]. In Fig. 7 are schematically illustrated the fusion zone profile of several heat source densities, so the geometry of weld is strictly connected to the power density [29].

Process	Heat Source Intensity (Wm^{-2})	Condition	Fused Zone Profile
Flux-shielded arc welding	5×10^{6} to 5×10^{8}		
Gas-shielded arc welding	5×10^{6} to 5×10^{8}	Normal current	
		High current	
Plasma	5×10^{6} to 5×10^{10}	Low current	
		High current	
Electron beam and laser	10^{10} to 10^{12}	Defocused beam	
		Focused beam	

Fig. 7 *Typical heat sources intensity and geometry of fusion zone obtained at respective power densities [1].*

1.1.2.1. Keyhole stability and formation

The study of the physical mechanisms is paramount to the ability of control the weld quality in many industrial applications [30, 31]. In keyhole mode, a deep keyhole is formed by the material evaporation. When the temperature increases drastically, the liquid metal starts to evaporate rapidly, the plasma ionizes. High temperature vapor and plasma tend to expand, producing recoil force pushing the liquid down and produce the keyhole. This is the leading force to the formation and preservation of the keyhole. In particularly four force operating on the keyhole walls. Here follow the forces that are involved in the formation of the keyhole. Eq. 1 shows the pressure balance acting on the keyhole wall [18, 32, 33]:

$$P_{abl} + \delta P_g = P_w \qquad \text{Eq. 1}$$

Where, P_{abl} [N/m^2] defines the recoil pressure, which is also named ablation pressure since the evaporation jet produces an ablation pressure on the surface.

δP_g represents the excess vapor pressure within the keyhole and it is due to the gas flow out of the keyhole. It can be defined as in Eq. 2, where d represent the thickness of the works piece and r is the radius of keyhole.

$$\delta P_g \approx \frac{1}{3} mnu^2 \left(\frac{d}{r}\right)^2 \qquad \text{Eq. 2}$$

Laplace's formula, displays the pressure due to the surface tension (Eq. 3):

$$P_w = \frac{W}{r} \qquad \text{Eq. 3}$$

where [34] W is the surface tension coefficient. Other terms such as the hydrostatic and hydrodynamic pressures due to the melt can be ignored for a workpiece thickness d≤1 cm and for low welding speeds [35]. In the equation of pressure balance, the pressure terms on the left side act to open the keyhole and those of the right-side act to close the keyhole.

The plot of the pressure terms on the left- and right-hand sides of equation as functions of the keyhole radius is showed in Fig. 8. The sum of ablation pressure and excess vapor pressure shows a maximum value in the graph.

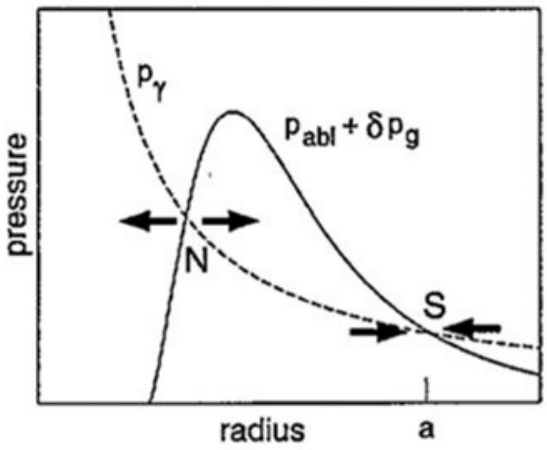

Fig. 8 *Trend of ablation pressure together with excess pressure and surface tension [34].*

N and S points are the intersection of the pressure terms curves on the left- and right-hand sides of equation, respectively. These points determine the equilibrium point of the keyhole radius. To the left of the equilibrium state N, the surface tension pressure exceeds the ablation pressure. Therefore, the keyhole tends to close itself and this leads to a collapsing keyhole. Consequently, point N is unstable and point S is stable.

1.1.2.2. Welding metallurgy

The microstructure obtained by laser welding is highly influenced by the high solidification rate, typical of laser welding. Welding process identified different zones at welding bead. Those different zones are associate with various transformations on equilibrium phase diagrams and are regulated for non-equilibrium cooling and heating effects [1, 36]. Three different zones are detected in laser welding (see Fig. 9).

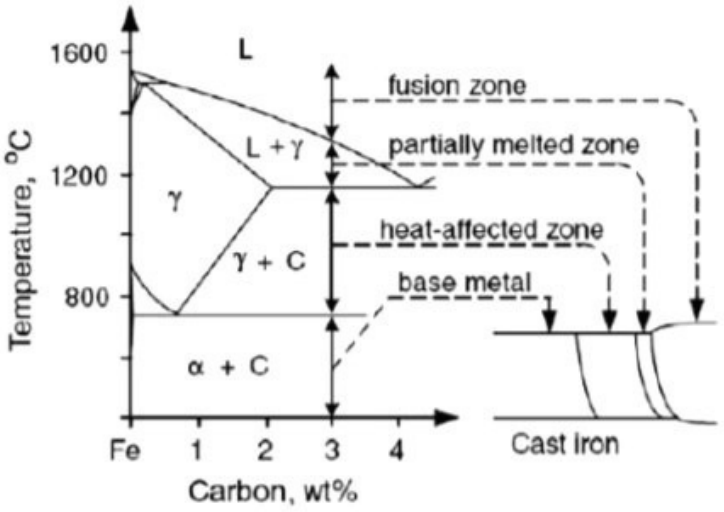

Fig. 9 *Different zones in a cast iron during welding process [37].*

The fusion zone or weld metal is designed as FZ is the region of the weld that totally melts during the welding process.

It is important to understand the properties of the final weld, because it can quite different in structure and properties from the base material. Clearly, if filler is employed in making the weld, the structure and composition, and consequently the properties, of the FZ can be completely different than the base material, due to different the composition of the filler and base material is and on how much dilution occurred.

In 1976, Savage et al. [38, 39] suggested numerous changes to the terminology used to represent fusion weld microstructure zones.

At the outward of the fusion boundary is a narrow zone, called unmixed (UMZ) that consists of melted and re-solidified base metal that does not mix with the filler metal. In some alloy systems, the UMZ can show microstructures and properties especially when dissimilar filler metals are employed.

In proximity of the fusion zone is a narrow zone named partially melted zone (or PMZ) where the temperature of the base material due to welding thermal cycle rise to between the liquidus temperature ($T_{liquidus}$) and the solidus temperature ($T_{solidus}$) for the alloy. The PMZ is important to the properties of the weld, as has exhibit some degree of melting and solidification, so different from the base material.

Somewhat farther away from the centerline of a fusion zone, there is a zone heated to near the solidus but never fused. This zone is called as the heat-affected zone (or HAZ).

Microstructure in the HAZ can be relatively complex, because it depends on both composition and thermal factors. The variable that can influence the HAZ microstructure are mainly welding process, material type heat input, and material condition prior to welding. The heat affected zone can highly modify the mechanical characteristic of the alloy.

Another zone observed during the welding process is the unaffected base material (UBM) or base material (BM). In this zone the heat from laser beam do not produce changes in properties and metallurgical structure.

The so-called "weld zone" include the fusion, partially melted (if any), and heat-affected zones, since this is the zone where base material structure and properties have been transformed by welding process.

Fig. 10 show the transverse section of a butt laser weld joint.

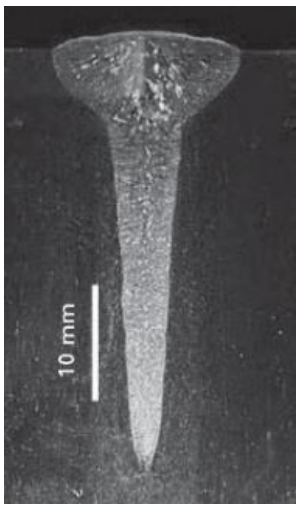

Fig. 10 *Cross-section of weld AISI 304 steel obtained with fiber laser [19]*

Laser beam has a high-power density, which enables to form a deeply penetrating weld pool. A narrow weld bead is obtained with a high aspect ratio, defined as the ratio between the depth and the width of the fusion zone. The laser joints have normally high aspect ratio.

Usually, laser welding is considered a rapid solidification process, which promotes the formation of non-equilibrium or metastable crystalline phases, a refinement of microstructure, such as, the size and shape of grains, and the shape and location of the phases present. In particular, several studies have observed that the faster solidification rate the better the weld strength and ductility [40]. Also, for laser welding, the principles of solidification determine the size and shape of the grains, the distribution of inclusions and porosity and segregation.

Rutter and Chalmers [1, 41] developed a theory to describe the stability of the liquid/solid interface, and to determine the eventually morphology. The stability of the solid-liquid interface is generally determined by the thermal and constitutional conditions, i.e. constitutional supercooling, that occur in the proximity of the interface [1, 42-44]. According to these conditions, the interface growth can occur by either planar, cellular, or dendritic growth (Fig. 11).

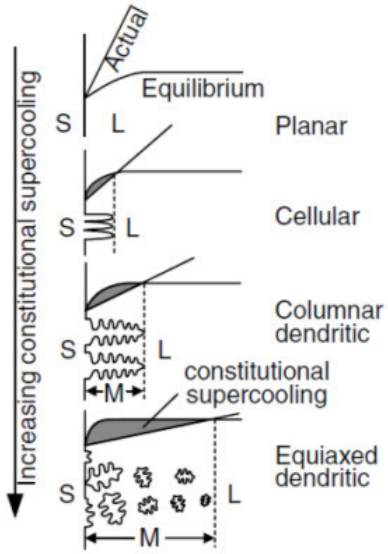

Fig. 11 *Schematic representation of interface morphology during solidification of an alloy [45].*

The criterion for constitutional supercooling for plane front instability can be mathematically stated as in Eq. 4 and Eq. 5 [44]:

$$\text{Condition for plane front stable} \rightarrow \frac{G}{R} > \frac{\Delta T}{D_L} \qquad \text{Eq. 4}$$

$$\text{Condition for planar instability} \rightarrow \frac{G}{R} < \frac{\Delta T}{D_L} \qquad \text{Eq. 5}$$

Fig. 12 displays the relationship between the ratio and the microstructural morphology. The instability results in the transition from planar to equiaxed dendrite. In the Fig. the ratio between G and R regulars the morphology of the solidification structure, while their product the size of the structure.

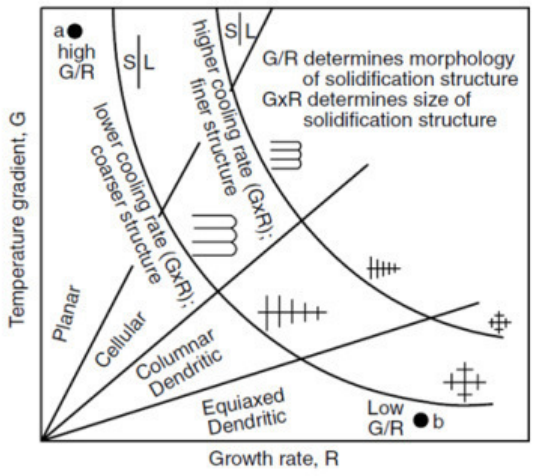

Fig. 12 *Representation of effect of temperature gradient G vs growth rate R on the morphology and size of solidification microstructure [45].*

Moreover, to control the properties of the weld metal, it is important to understand the change of the weld metal grain structure. Savage et al. [46] observed the effect of welding parameters (the heat input and the welding speed), on the weld metal grain structure. Fig. 13 shows that at low heat input and welding speed, the weld pool becomes elliptical in shape and the columnar grains curves in the welding direction. While at high heat input and welding speed, the shape of weld pool is teardrop and the columnar grains are straight. In both cases, grain growth initiates from the substrate at the fusion boundary and proceeds toward the weld centerline. While with high heat input and welding speed, the grain can nucleate in the bulk weld metal [47].

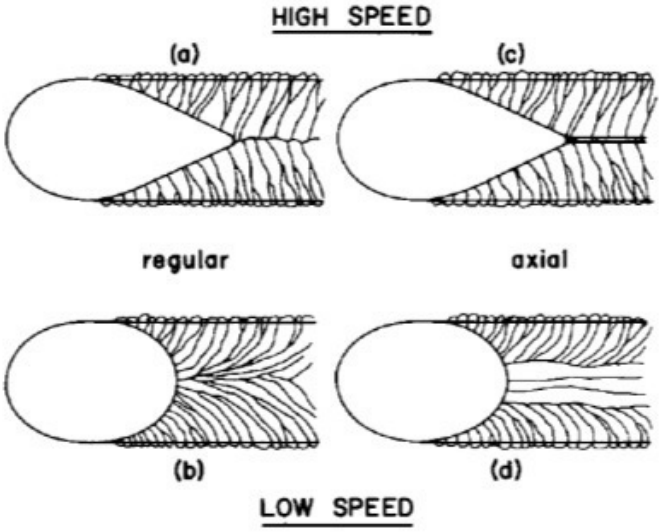

Fig. 13 *Effect of welding parameters on grain structure [45].*

Furthermore, it is important to consider the effect of welding parameters on the heterogeneous nucleation, hence on the grain morphology.

Kato et al. [48], Arata et al. [49], Ganaha et al. [50], and Kou and Le [47] observed in commercial Aluminum alloys that higher heat input and welding speed increase the formation of equiaxed grains. The heat input and the welding speed are increased, the temperature gradient (G) at the end of the weld pool is diminished [51] (see Fig. 14).

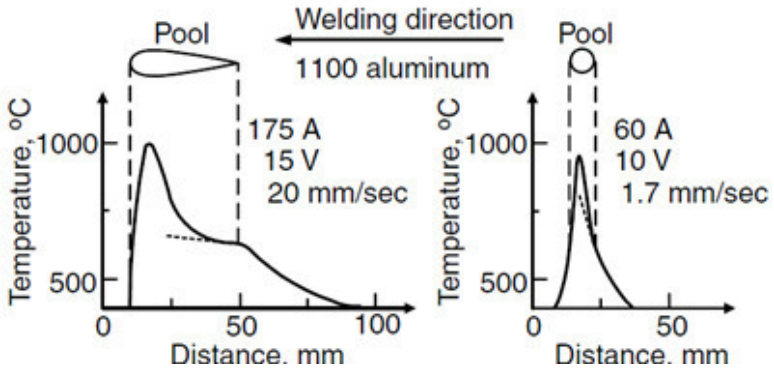

Fig. 14 *Influence of welding parameters on temperature gradient at weld pool end [45].*

1.1.2.3. Weld quality and weld defects

In weld application, quality is an important factor. Several defects and imperfections may occur due to the material and its composition, welding condition, and so on. Laser welding defects are divided into three groups: geometrical or appearance defects, internal, and property or quality defects [52, 53].

The common geometrical defects are deformations or distortions, poor surface appearance, burn-through or drop- trough, undercutting, underfilling, reinforcement of weld or overlapping and humping [54]. The laser welding process can generate also internal or invisible defects and chemical inhomogeneities in the weld metal. In this classification hot and cold cracking, incomplete fusion or lack of fusion, incomplete penetration, inclusions, gas and solute segregation (microsegregation and macrosegregation) porosity are included [19].

Microsegregation essentially happens due to the fast solidification process in fusion welding particularly for laser beam welding of alloys [52, 53, 55]. Microsegregation can diminish significantly the mechanical characteristic of the weld, and it can have an important effect on the solidification cracking susceptibility of the joint. To avoid the reduction in hardness and strength due to the microsegregation, the solid solution heat treatment of the weld after laser beam welding can offer positive solution.

Macrosegregation is due to the partial weld pool mixing in the fusion zone. Generally, weld pool convection can usually mix the weld pool well to minimize macrosegregation across the resultant weld metal. Macrosegregation is observe in the weld fusion zone, in particularly this defect is present in laser welding of dissimilar materials [56] or using a filler wire different in chemical composition from the base metal [57]. In fact, in laser welding process, adequate mixing of a filler wire into the base metal is very difficult, and therefore the compositions of the bottom part of the weld fusion zone are approaching those of the base material [19, 45].

Porosity defect can be due to by the surface cleanness of the butt joint, gas, welding condition and the weld shielding. Although round gas pores can be casually distributed in the weld metal, they can also line up and produce bands of porosity, this condition is severe during weld metal solidification [58]. To avoid the formation of pores several measures can be performed, comprising keyhole laser welding under the appropriate conditions, welding with a shallow, stable keyhole or heat-conduction type welding, selection

of a suitable shielding gas for the material. In welding process, it is important to remark the effect of the thermal cycle due to high power laser welding. The thermal cycle can cause different microstructure and therefore different mechanic characteristics in the HAZ.

1.1.2.4. Residual stresses and distortions in weldments

Residual stresses remain in a body after that all the external loads are suppressed. Moreover, if the weld has previously been subjected to non-uniform temperature changes, residual stresses are often called thermal stresses. The Fig. 15 shows the distributions of the residual stress in the welding direction (σ_x) and temperature changes during the welding cycle.

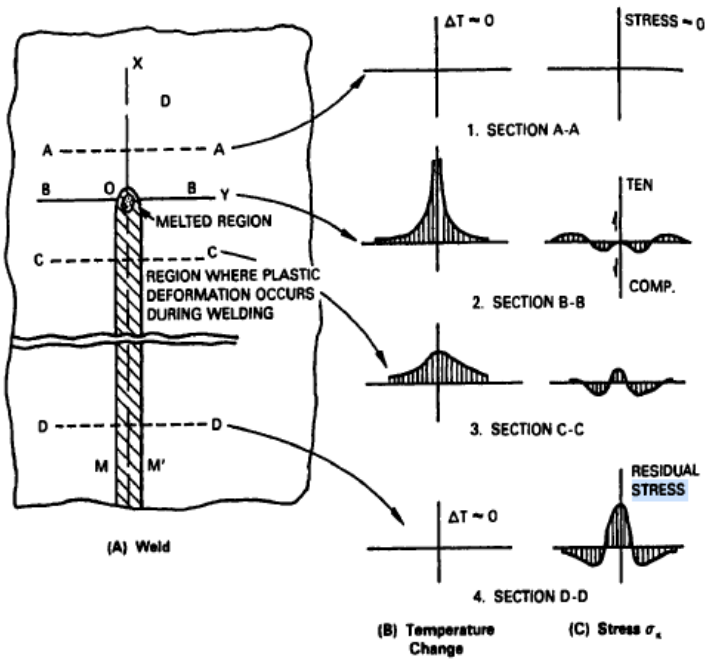

Fig. 15 *Profiles of temperature and residual stress profiles during welding and after cooling [19].*

The zone where plastic deformation occurs is the crosshatched area M–M', and it corresponds to the fusion and heat affected zone. Section A–A is far away from the heat source, so the temperature is zero, while section B-B is situated in the middle of the heat source. From section B-B the temperature distribution becomes less steep in section C-C. The temperature is constant far away from the heat source, see section D–D. In section A–A where the temperature doesn't change, the longitudinal stresses σ_x is nil. In the region B-B the material melts and the weld pool does not have strength to support external load so σ_x is close to zero. In the region where the metal is solid, near the weld pool stresses are compressive (σ_x is negative) due to the adjacent metal that does not permitting the expansion of these areas. After solidification in the section D-D, both weld metal and the adjacent base metal have an inclination to contract generating high tensile stresses and compressive stresses in regions away from the weld.

The characteristic distribution of longitudinal (σ_x) and transverse (σ_y) residual stresses in butt weld, after cooling is showed in Fig. 16.

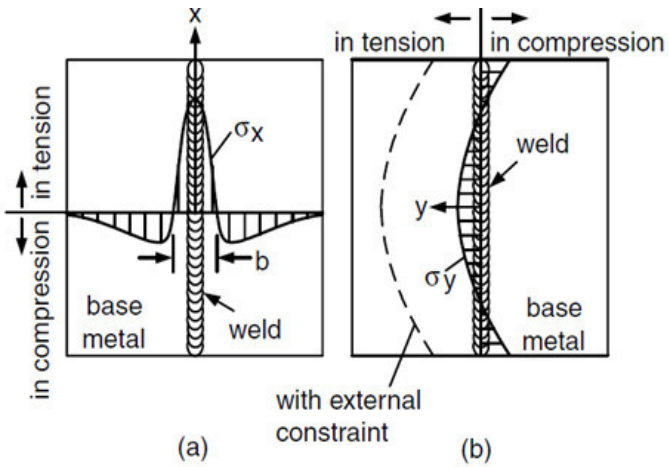

Fig. 16 *Characteristic distributions of longitudinal (σ_x) and transverse (σ_y) residual stresses in butt weld [19].*

For the longitudinal stresses, the trend is alike that above described. Low magnitude of transversal tensile stress formed in the middle area of the weld, where the cool base material, away from the butt joint, restrains thermal contraction in the transverse section.

Moreover, in the weld welding can observe three fundamental dimensional changes. 1) The transverse shrinkage that occurs perpendicular to the weld line; 2) the longitudinal shrinkage that occurs parallel to the weld line; 3) the angular change that consists of rotation that occurs around the weld line (Fig. 17).

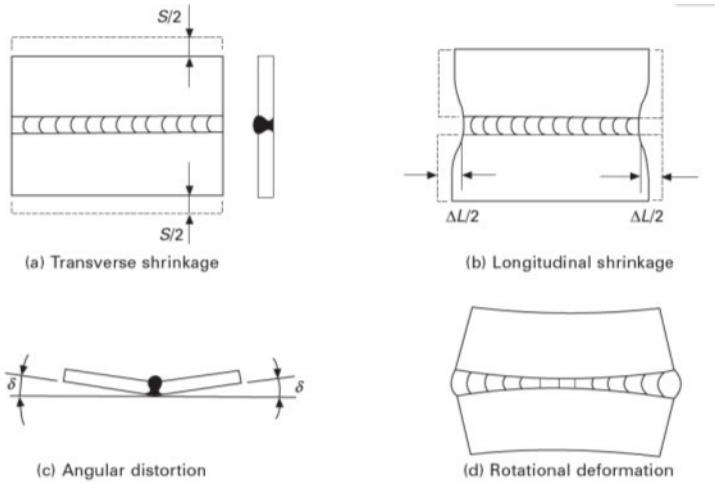

Fig. 17 *Typical distortion in the weld: transverse shrinkage, longitudinal shrinkage, angular distortion and rotational deformation [1].*

Transverse shrinkage that occurs is influenced by the size (width and volume) of the weld and, so, heat input, joint configuration and the thermophysical properties of the base material. In general, longitudinal shrinkage in a weld joint is typically much less than transverse shrinkage (typically 1/1000 of the weld

length). Moreover, angular distortion is the consequence of non-uniformity of transverse shrinkage through the thickness. Angular distortion is mainly a function weld cross-sectional shape.

1.1.3. Laser welding: advantages, disadvantages and application

Laser beam welding techniques promotes many possible advantages over conventional arc welding technologies. Keyhole mode executes deep penetration welds and to weld particularly thick substrates with a single weld pass, thus presenting fewer occasions for defects.

Laser welding use a controlled beam which permits low net heat input that can product in considerably reduced distortion [59].

Laser welding offer several advantages as: low heat distortion, high welding speed and high weld quality, high weld aspect ratio, low distortion, manufacturing flexibility and ease of automation [60, 61]. In particular, Nd:YAG and CO_2 lasers are being generally used in the manufactory industries and aerospace sectors. Especially, the fiber laser offset welding is an innovative technique, which has revealed to be also adequate for dissimilar weld [62, 63]. The main disadvantages of laser welding are due the higher cost of laser equipment than conventional arc welding. Moreover, due to the fast cooling rates cracking, liquation cracking, hot cracking or formation of brittle microstructures can occur. Other disadvantages of this technology are the difficult melting of highly thermal conductive metals, the small gap tolerance, and the formation of porosity in deeply penetrated weld fusion zone. Moreover, it is not safe to employ laser welding technology in portable or manual operations [4].

1.2. Joints configuration

The type of joint is mainly determined by the geometric conditions, limits of the structure or the type of loading. Moreover, the choice of the joint type is affected by the type of mechanical load (for example uniaxial, biaxial, or triaxial; static or dynamic; tension, compression, torsion or bending), the cost and accessibility for inspection. Fig. 18 shows the principal types of welds.

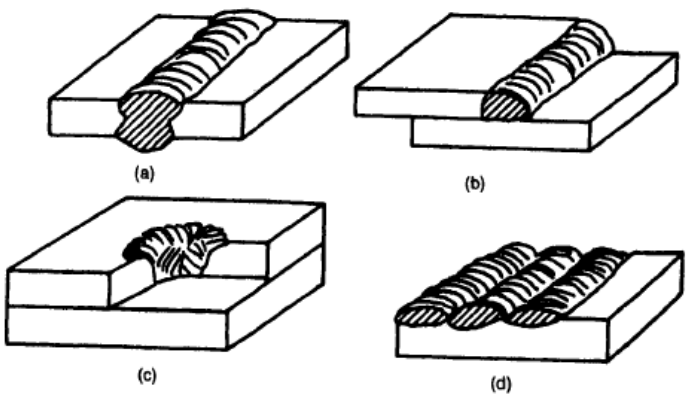

Fig. 18 *Joints configuration: (a) butt, (b) fillet, (c) plug, and (d) surfacing [1].*

Generally, groove, fillet, and plug welds are employed for welding structural elements. While surfacing welds are employed for applying material to a workpiece by welding and preserving from wear and corrosion.

Five joint configurations for producing structures (1) butt joints, (2) corner joints, (3) edge joints, (4) lap joints, and (5) T joints, are shown in Fig. 19.

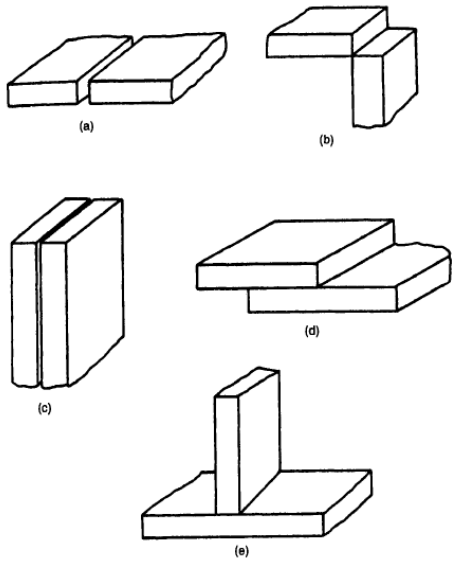

Fig. 19 *The five joint configurations for producing structures: (a) butt joint, (b) corner joint, (c) edge joint, (d) lap joint, and (e) T joint [1].*

Moreover, there are typical weld joints variations. For example, butt joints are also named square butts or straight butts when they are obtained from joint elements prepared (before welding) with square or straight. Alignment of butt joints is crucial due to the small focal spot size; consequently, joint preparation must be precise. In butt joint, the gap must be sufficiently small so the beam cannot pass straight through the weld.

However, overlap joints can have single or double fillets. While, T joints can be made using double fillets, single or double bevels.

1.3. Laser welding of dissimilar metals

Dissimilar laser welding includes different basic elements (e.g. aluminum and steel, magnesium and steel) and different classes of materials (e.g. aluminum and CFRP). Dissimilar welds are increasingly employed in the industrial field (petrochemical, chemical and electronics) in order to offer economic advantages and to improve performance compared to components made of a single material [64]. Dissimilar welds can be obtained in a variety of different metals and welding processes like laser, arc, and friction stir welding, as well as by hybrid process like laser-arc hybrid welding. However, the advantages of combinations of different materials may be numerous, dissimilar welds can offer several problems due to different materials properties, which have a significant effect on both the connection process and the final

properties of the joint. Principally, this problem arise from the difference between the thermal expansion coefficients, causing distortion and residual stresses in the weld. Moreover, the joining of different materials implicates the development of improper microstructures and second phases (e.g., chemical segregations intermetallic compounds, martensite) in the fusion and heat affected zone, which have a negative effect on weld strength. The limited solubility of the dissimilar joints results in brittle intermetallic compounds (IMCs). The formation of this layer is promoted by diffusion, since it is an important driving mechanism for phase formation [65]. Thus, the development of Al–Fe phases shows a key role in realizing an a connection between the two different metals, however the generation of IMCs results in brittleness and degrades the strength of the weld [66]. Some authors study the welding conditions which minimize the growth of brittle phases. Meco et al., studied the evolution and distribution of IMCs associated with the thermal cycle [67]. Gao et al. observed that the non-uniformity in the thickness and the irregular shape of the interface growth with the heat input [68]. Casalino et al. investigate the effect of laser offset welding (LOW) on the IMC layer. In this study was demonstrated the weldability of titanium and aluminum by LOW method [69]. The it has been demonstrated that this technique restricted the growth of an IMC layer and promoted the diffusion through the liquid-solid boundary. This method was employed for several dissimilar welds [62, 63, 69].
Moreover, the mechanical properties of dissimilar welds are severely related to the development of IMC layer, and to its morphology. In fact, the interface zone with its steep property gradient is frequently connected with crack initiation or crack propagation.

1.4. Hybrid laser-arc welding

Hybrid laser-arc welding (HLAW) is an advanced welding process, that has been development in the last decade [71, 72]. Hybrid laser-arc welding is prominent joining process since it can compensate for the weaknesses in laser welding and arc welding by utilizing both features. Hybrid laser-arc welding combined two heat sources that act in the same time, principally laser beam welding and arc welding (Fig. 20). Hybrid welding provides many advantages over laser welding and arc welding alone [73, 74].

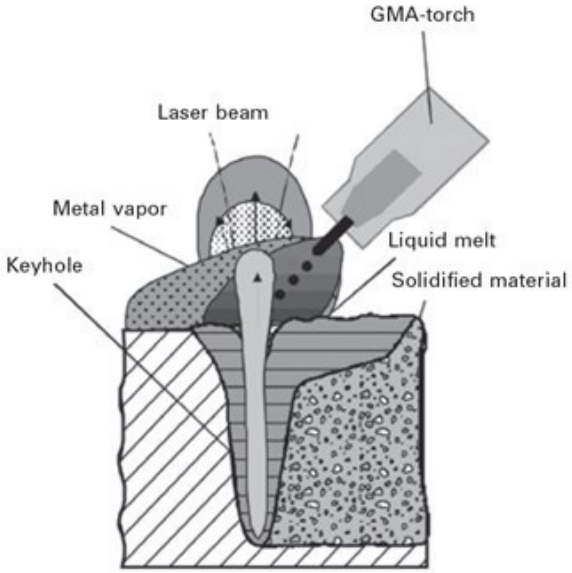

Fig. 20 Sketch of a hybrid *laser-arc welding technology [19].*

Hybrid laser-arc welding offer several advantages as high welding speed, deep penetration [75], excellent gap bridging ability [76, 77]. The formation of pores and cracks are reduced [78, 79]. Lastly, this process can be considered stable and efficient. This technology is first developed by Steen et al. [74, 80, 81]. The influence of parameters on penetration, speed and bridging in laser hybrid welding. In their study, a CO_2 laser was jointed with a tungsten inert gas (TIG) arc for welding and cutting applications. Japanese researchers formulated this study, but due to the expensive cost laser joining technique at that time [82], this technique was not developed into engineering applications. In the early 1990s, when laser source begins to be more accessible, combined welding processes using a high-power laser beam as the primary and an additional electric arc as the secondary heating source [80, 81] have been developed.

The heat sources, that is named the "primary source", used in hybrid welding are CO_2, Nd:YAG, and fiber lasers. The first two types are generally used for several applications, while the fiber laser, due to its high beam quality, is still in development for industrial applications. The arc heating source, that is named the "secondary source", used in hybrid welding are principally electric arcs.

In hybrid welding process, laser and arc are disposed in different way, in all case there is the formation of a common interaction zone. Mainly, laser and arc can act in the same points, in this condition there is not any distance between the two heat sources, or in two different points. In the last case, different configurations are obtainable: parallel or serial arrangement. In the last case the primary and secondary heating sources are moved along the same welding path with a definite working distance, and the secondary heating source can either lead or follow the primary heating source. In arc leading configuration, arc promotes a preheating of the region to be welded, rising the efficiency of the laser welding process because materials to be welded are locally preheated. In laser leading configuration, the arc promotes a short-time post-heat treatment of the weld that can modification the weld microstructure positively.

During the hybrid laser-arc welding process is important the interaction between arc and laser. Moreover, numerous studies have been established that the plume temperature is higher in hybrid welding process than in laser welding, and therefore, the plasma emission intensity growths with an increase in arc current. In hybrid laser-arc welding there are several process parameters: electric power parameters, laser beam parameters laser-arc interval, electrode diameter, welding speed, wire feed speed and shielding gas.

There are several combinations of laser and arc welding systems have been developed. GMAW (gas metal arc welding), MIG (metal inert gas) welding, is used as secondary heat source. The arc is produced between the consumable metal electrode and the work piece. During the welding process, the laser produces a keyhole, while the molten filler material incessantly fed from a spool helps to fill the root gap and ensures welding of the parts with higher gaps [83]. Moreover, the use of filler materials improves the mechanical properties and chemical composition of the weld [84]. Shielding gases are employed to isolate the molten weld pool from atmospheric contamination. It has a significant effect on process stability and the quality of welded joints.

According to the combination of various heat sources hybrid laser-arc welding can be includes: Gas Metal Arc Welding (GMAW), sometimes concerning metal inert gas (MIG) welding or metal active gas (MAG) welding, Gas Tungsten Arc Welding (GTAW) or Tungsten Inert Gas (TIG) and Plasma Arc Welding (PAW).

1.4.1. Gas Metal Arc Welding (GMAW)

The gas-metal arc welding (GMAW) (or metal-inert gas, MIG) process uses in general a continuous consumable solid wire electrode. GMAW includes a variety of components necessary to produce the arc. The power supply affords the electrical voltage and current indispensable to sustain the arc. The current is powered through cables to the contact tip situated in the welding torch, which offers a low resistance electrical connection to the consumable electrode filler wire.

The consumable filler wire is fed to the welding torch. The shielding gas is powered coaxially through the torch to guarantee suitable coverage for arc stabilization and process shielding. The torch can be employed either manually or automatically by robot. Fig. 21 shows a schematic of a typical GMAW process.

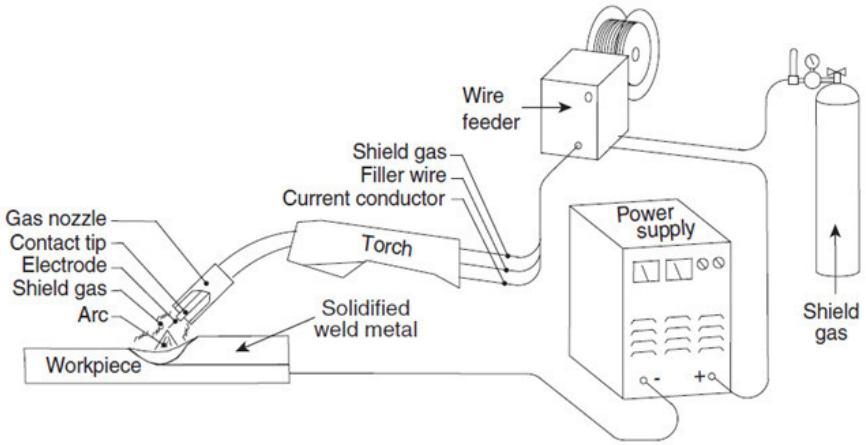

Fig. 21 *Schematic representation of a typical gas metal arc weld (GMAW) [4].*

Shield gas is fed between the consumable electrode and the metal component to weld. A variety of gas mixture can be used to stabilize the arc and, also to shield the molten weld pool from oxidation with the atmosphere and from other atmospheric impurities. The choice of shield gas is influenced by the types of alloy that are being joined, the weld transfer mode and the economics of the manufacturing process. In general, Argon (Ar) is a used component of shield gas mixtures for welding a variety of metals because it prevents oxidation of the molten weld pool of the hot metal as it solidifies and cools. A variety of other gases are CO_2 and oxygen (O_2). They are often used to joining ferrous alloys. However, CO_2 is low cost and its reactivity produces a wider and hotter arc that produces a deep penetration profile and often increased spatter. The use of oxygen promotes to oxidation of alloy contaminants, which can improve properties because they are discarded undesirable contaminants from the weld zone. However, oxygen promotes the formation of slag on the weld surface, which can be dangerous in some welding process. The selection of an appropriate shield gas for a given weld application is a delicate choice.

The consumable electrode is chosen to balance cost of the welding process with through quality requirements. The choice of electrode alloys and configurations are developed to provide a several beneficial functions, such as increasing feed ability and process stability, deoxidation and fed of weld pool contaminants and increased conductivity.

Gas-metal arc welding introduces numerous advantages relative to many other welding processes. Welding equipment can be quite inexpensive compared to other high cost welding processes like laser welding. Moreover, the simple process that is quite easy to learn and use, and yet also offers itself to mechanization or automation. The wire is powered from a roll, and consequently can offer longer length welds without error prone starts and stops, permitting faster deposition rates. However, this process, with suitable parameters and process conditions, is appropriate to the joining of a wide variety of metals.

However, the GMAW process presents several disadvantages as compared with other welding processes. Therefore, suitable parameter selection is sometimes difficult to realize, so there is a possibility of formation of weld spatter. Additionally, GMAW is not appropriate for the single pass weld of thick materials, and therefore multi-pass welds are often essential, so cause high heat input and important

consumption of filler wire material. In addition, the loss of a droplet of material from the electrode radically changes arc features, so produce in undesirable spatter formation.

1.4.2. Gas Tungsten Arc Welding (GMAW)

This welding technology uses a permanent, no-consumable tungsten electrode to produce an arc to a workpiece. The tungsten electrode is protected by an inert gas, such as argon or helium (or a mixture of the two), to avoid electrode degradation. The operator can add filler material to the molten weld pool, if necessary, through a wire feeding system or manually. Gas, powered through the welding torch, promotes the formation of the arc and shields the molten metal from atmospheric pollution.

The power supply produces the voltage and current (direct or alternating) essential to support the arc. The current is powered through cables to the tungsten electrode, positioned in the welding torch. Moreover, the other lead from the power source must join to the workpiece to complete the electrical circuit once the arc is established. A representative GTAW setup is shown in Fig. 22.

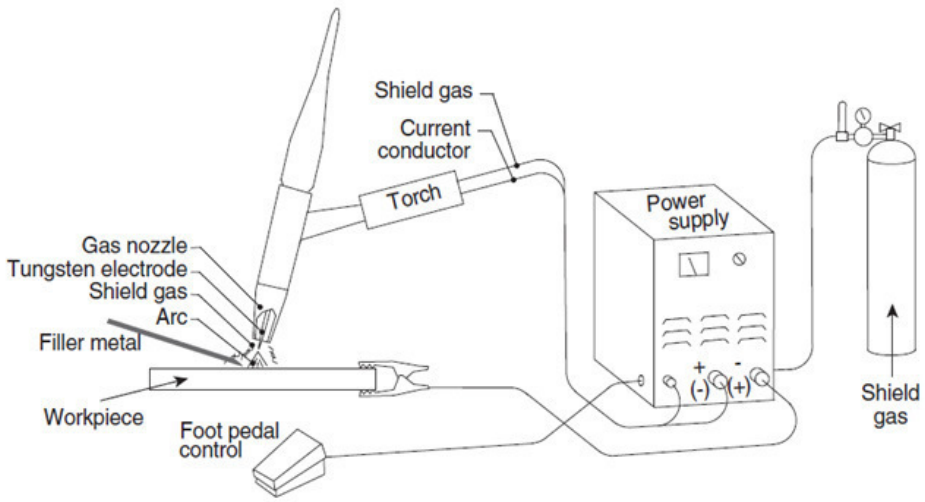

Fig. 22 *Schematic representation of a typical Gas Tungsten Arc Welding (GTAW) [4].*

The welding torch, which may be water cooled, not only contains the tungsten electrode, but also powered the shielding gas to offer adequate protection for process shielding and arc stabilization.

This technology joins more types of metals than GMAW and many other arc welding processes since the arc does not necessitate use of a consumable electrode. However, control of heat input permits to obtain narrow HAZ, which can product in improved mechanical properties of the weld. Additionally, the heat source control implies an excellent control of penetration and low distortion, so makes the process good for joining of thin materials. During the welding process, it is possible to obtain joints without slag because no flux is necessary.

Moreover, GTAW process produces a stable arc, and therefore are significantly reduced the formation of sparks or spatter. The GTAW technology is usually considered relatively clean, and an expert welder can obtain high quality joints.

However, this process produced generally low filler metal deposition and low speeds compared with GMAW because the filler material is powered in cold. When Gas Tungsten Arc Welding is utilized in an alternating current mode, such as usually used for aluminum joints, the process is relatively noisy and disturbing. Furthermore, tungsten inclusions are likely to occur.

1.4.3. Effect of welding parameters on hybrid laser-arc welding

In the combination of an arc and a laser beam in a hybrid welding technology, a wide variety of parameters must to be considered simultaneously. The influence of the hybrid laser-arc welding parameters is examined as follows.

1.4.3.1. Laser power

During hybrid laser-arc welding, laser power is responsible of the formation of the keyhole and guarantees the deep penetration welding [85-87]. In particular, it was established that the weld penetration increases with laser power [88, 89]. Moreover, filler wire feed rate is necessary to increased due to of high welding speed that can offer a decrease of weld width and weld penetration [85, 90-92]. Additionally, high welding speed may produce a lack of penetration of the joint, while, a low welding speed may produce a larger weld pool with incomplete decomposition [86].

1.4.3.2. Positioning of the laser beam and the electrode

In laser leading configuration larger width of arc zone, narrow width of laser zone, larger reinforcement height, and higher penetration depth [93] are observed. Particularly, the cross section morphology of joint observed for laser leading set up is ‘cocktail cup-shaped’, while for arc leading is ‘cone-shaped’ [93-95]. Furthermore, using laser leading process, the stability of the arc due to higher stability of the keyhole [96, 97] is detected.

Another important parameter concerning the double heat source arrangement is the distance between laser and arc [98, 99]. The laser to electrode separation distance is typically kept from 0 mm (for co-axial arrangement) to 5 mm (for paraxial arrangements), depending on the types of arc welding parameters, laser parameters, and materials used [97, 100].

1.4.3.3. Electrode angle

Electrode angle for arc source is in general 45–65° [89, 97, 101, 102] from the workpiece surface. This inclination allows the shielding gas exit from the torch nozzle to deflect the laser generated plasma from the fusion zone, rising the laser penetration of the joint. The laser beam is usually directed normal to the workpiece surface to achieve better penetration [102].

1.4.3.4. Shielding gas

Shielding gases is more important parameter in hybrid laser welding, due to its influence the weld profile, the arc characteristics, and on the mode of metal transfer [103]. The most employed gases in this processes are helium and argon [102, 104-107]. Moreover, a mixture of argon, helium and CO_2 is also used in CO_2 laser arc hybrid welding technology [99, 107]. Usually, helium warrants deeper penetration argon enhances the arc stability.

1.4.3.5. Wire feed rate

In general, unsuitable wire feed rate can produce lack of deposition or the supply of extra material [96, 108]. Nevertheless, when higher wire feed rate is employed, the higher current is necessary to increase the rate of deposition [102]. Effects of filler wire feed on the efficiency of laser welding.

1.4.3.6. Joint gap

When joint gap is up to 1 mm the welding speed can be growing [83] because the small weld gap facilitates the penetration, as more filler material reaches to the root of the weld. Usually, in laser welding the gap is up to 0.2–0.25 mm only, to avoid visible defects like incomplete weld bead or undercut. Instead, using hybrid laser-arc technology [83, 109] a weld gap of 1 mm can simply be welded.

1.4.3.7. Power regulation of the arc welding system

During the welding process, the current and voltage changes incessantly and their variations can affect the weld. Usually, current influences filler, the base materials and the rate of melting of the consumable electrode [108]. In general, constant voltage power supplies have been engaged in the of GMAW applications. The method of metal transfer in arc welding process is a significant factor. Usually, there are three different modes of metal transfer detected during arc welding: projected/spray transfer, gravitational/globular transfer, short-circuit transfer and rotating transfer (Fig. 1) [110].

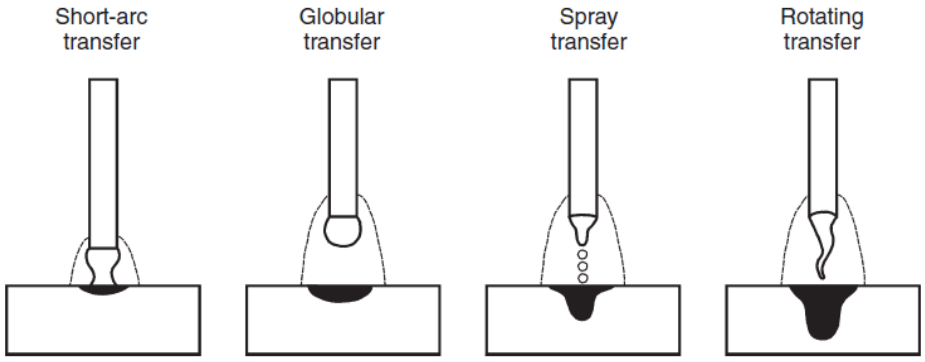

Fig. 23 *Metal transfer ways in GMAW [4].*

Short-circuiting occurs for low values of welding current and arc voltage. In these conditions, the arc regularly extinguishes while a short-circuiting bridge of molten material is obtained between electrode and weld pool. While the metal transfer into the molten base material is finished, the arc is revived again. This metal transfer way permits welding of thin materials without great distortion or residual stress in the fusion zone. The globular metal transfer way, in general, occurs during GMAW process with higher welding amperage and using CO_2 or a CO_2 rich gas mixture therefore metal is transfer in the form of large droplets with a diameter usually greater than the diameter of the electrode wire. The globular mode is restricted to welding ferrous materials with a thickness about 3 mm. During the spray transfer mode, the filler metal from the electrode is transferred in fine droplets. This transfer way is mainly used for welding of non-ferrous metals. However, this process permits to obtain good fusion and penetration characteristics, the good weld appearance and the absence of spatter during the welding process. Finally, during rotating metal transfer mode the filler wire electrode starts to rotate under the effect of the surrounding magnetic field. This process permits high deposition rates, consequently the rotating arc is difficult to controller, and, therefore, this metal transfer way is rarely executed.

1.4.3.8. Welding speed

Hybrid laser-arc welding process is characterized by higher welding speed, which increases the productivity. However, joint width and weld penetration are inversely executed by the welding speed [111-114]. Moreover, to overcome this problem, further laser power is necessary applied and the filler wire feed rate to be increased to preserve a constant volume of weld pool [114]. Consequently, the welding speed to filler wire feeding ratio is a significant factor for the stability of the keyhole and for the complete process [83]. Metallurgical defects within weldment can be observed due to the step temperature gradient at fusion zone [115]. Nevertheless, an increase in welding speed can reduce the thermal residual stress [116].

1.4.3.9. Weld configuration and edge preparation

In hybrid laser-arc welding process, joint configuration are butt, corner, edge, lap and tee joints. Moreover, in hybrid laser arc welding technology thin metal sheets or metal plates having thickness less than 6-8 mm can be simply welded without edge preparation. While, for thickness more than 6-8 mm the V or Y groove reminds the shape of a 'wine glass' or a 'funnel' [111, 116-118].

1.4.4. Weld appearance

The cross section of butt joints obtained with hybrid laser-arc technology is quite different from those obtained from other traditionally welding, due to the application of the two heat sources. The weld cross sections joined by HLAW presents the classic "wine-cup" shape with an upper zone denoted as "Crown Zone" (CZ), and a narrow lower Laser Zone (LZ) [93, 119]. The two zones exhibited different characteristic and morphology due to the influence of the two heat source powers. Mainly, the laser beam, being the laser focused in keyhole mode, principally controls the LZ shape. While the torch controls the CZ shape, being arc welding generally a superficial heating source. Fig. 24 shows a typical cross butt section obtained with of hybrid laser-arc welding.

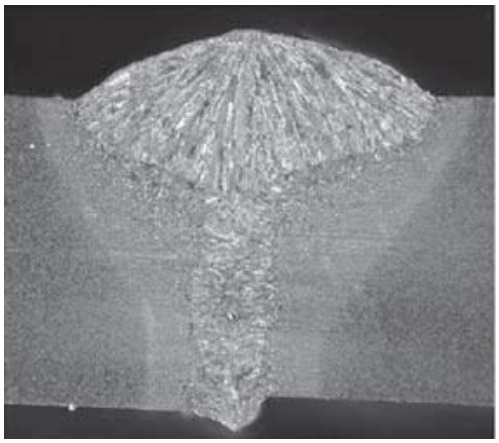

Fig. 24 *Typical cross section obtained with hybrid laser-arc technology [4].*

HLAW is described by different zones, depending on the heat from which is employed. These zones are fusion zone, partially melted zone and heat affected zone, but their morphology depends principally from material and from another factor.

1.4.5. HLAW applications

Hybrid arc-laser welding offers many advantages over traditional welding technology. Among this, low distortion, high-speed seam welding and single-pass welding in large thickness, easy automation [4], [120]. This technology has become more and more applied in many fields such as aerospace, automotive, shipbuilding oil and pressure vessel industries. In general, hybrid arc-laser welding is now making a

significant influence on the medium and heavy section welding industry. Principally this technology has been used initially in the shipbuilding industry. Another general application of hybrid laser-arc welding process is the welding of tanks, containers and tubes. This technology has been used in the automotive industry for several applications, for example in joining tailored blanks and lap joints in car body. In automotive industries, the driving force for the employed of HLAW process are the low energy input, higher welding speed and reduce distortion. Volkswagen and Audi have utilized this technology in the production lines.

1.5. Hybrid laser-arc welding of dissimilar metals

Hybrid laser arc welding combines the advantages of laser and arc welding and eliminates the disadvantages, so, the joints exhibits less distortions, a narrow heat affected zone, high welding speed, arc stability [4]. It has confirmed to be appropriate for dissimilar welding of steels and of steels and aluminum alloys [121].

Casalino et al., investigated the effect of the post weld heat treatment of AA5754 after fiber arc laser welding [122].

Spena et al., examined the weldability of high strength steels for automotive application by hybrid laser-arc welding. Dual phase (DP) steel and twinning-induced plasticity (TWIP) steel were joined by laser arc hybrid welding. For DP/TWIP steel the austenitic filler wire (316-Si/SKR-Si) was chosen to avoid manganese segregations and martensite in the fusion zone and consequently, improve the weld strength [123].

Moreover, fiber laser system offers high optical output power and high conversion efficiency, high beam qualities and a short emission wavelength around 1 μm. Casalino et al., studied the weldability of dissimilar stainless steel joints. So far, some studies have been published about laser-TIG hybrid welding of dissimilar stainless steel with exhaustive characterization of microstructural transformation and mechanical properties.

1.6. Materials for automotive industry

Nowadays, car is a multi-material vehicle. The main reason is that the vehicle weight and the fuel consumption rely strongly on material car body weight. In the last years, the average vehicle weight was reduced by 18%. New materials production and development plays an important role in the automotive industry. Therefore, advanced high strength steels (AHSSs), stainless steel and aluminum alloys can be used in automotive body component with positive effects on the vehicle performance.

1.6.1. Stainless steel weldability

In the automotive industry, increasing the use of stainless steel to, improve aesthetics, increase safety and minimize life cycle cost has been increased [124]. The property of this steels are corrosion and fire resistance however they ensure security and reliability. Moreover, stainless steel exhibit good combinations of strength and ductility, which is of fundamental property in automotive applications. Consequently, maintenance cost is lower and this material at the end of its long life is easily recycled. The high resistance of corrosion is a crucial factor especially in crash situations. In fact, the absence of body car corrosion means lack of weak points. In automotive applications, stainless steel are most widely used for exhaust systems (Fig. 25). For example, ferritic stainless steel with stabilization elements like Titanium, Niobium are widely used in parts of automotive exhaust systems such as manifolds, exhaust pipes, mufflers, catalytic converters [125].

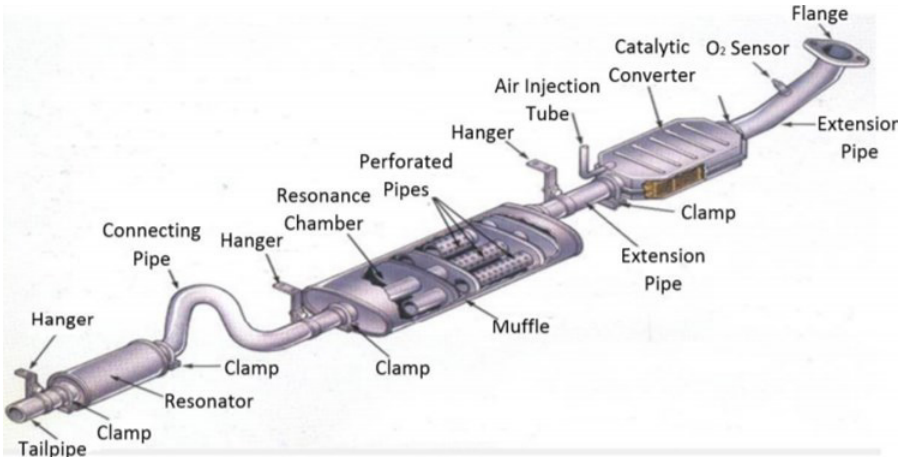

Fig. 25 *Automotive exhaust system [125].*

Moreover, heavy vehicles make wide use of austenitic stainless steel for outer panels. Steels used for these applications are AISI 301, AISI 304 and AISI 430. Cold worked Cr-Mn Stainless steel is now employed for full size building of urban bus (Ultralight Urban Bus) (Fig. 26). Due to the property of weight reduction, a higher percent of passengers can be carried on the same bus.

Fig. 26 *(a) Ultralight Urban Bus and (b) Body structure [126].*

Dissimilar stainless steel welds have important applications when it is necessary to combine both the excellent formability, and their excellent oxidation and corrosion resistance. However, welding of stainless steel joints is complex due to the chemical, physical and thermal differences between the two materials, such as different property such as: thermal expansion coefficients, melting points thermal or conductivities. Mainly the difference in thermal property can produce high stress around the weld interface due to uneven heating of the metals. Another problem of welding stainless steel joints interests the reduction of the mechanical properties due to metallurgical phenomena, such as micro segregation, porosity and grain growth in the HAZ [127, 128].

1.6.2. Advanced High Strength Steels Weldability

In the last year, use of AHSS steel in automotive body design has increased significantly over the past 20 years. The application of high strength steels is due to the need increase the lightweight design, car safety, fuel economy. This steel exhibit high strength and higher formability. The materials having yield strength less than 210 MPa are considered as conventional steel. While High-Strength Steels (HSS) has yield strengths from 210 to 550 MPa and tensile strengths from 270–700 MPa, while Ultra/Advanced High Strength Steels (UHSS or AHSS) steels have yield strengths greater than 550 MPa and tensile strengths greater than 700 MPa [129]. The first generation of these AHSS includes: Dual phase (DP), Transformation-induced plasticity (TRIP), Complex phase (CP), Martensitic (MS). The second generation AHSS include: Twinning-induced plasticity steel (TWIP).

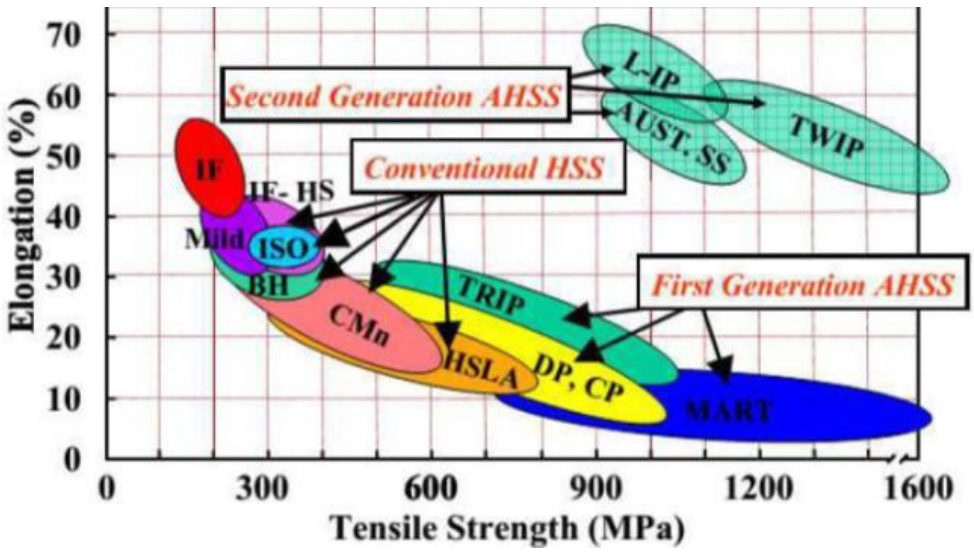

Fig. 27 *Total elongation vs tensile strength [130].*

Below are classified the primary types of AHSSs steels. Dual Phase steel microstructure consist of a ferrite matrix with hard isles of martensite. Increasing the volume of hard martensite generally increases the strength. DP600 is widely used in automobile applications, and 600 series means that the tensile

strength is over 600 MPa. Fig. 28 illustrates the application of various DP steels in automotive industry such as bumper beam, roof bow, rear side member, front floor cross member, floor side reinforcement, front side members, safety cage components (B-pillar, floor panel tunnel, engine cradle, front sub-frame package tray, and seat) [131].

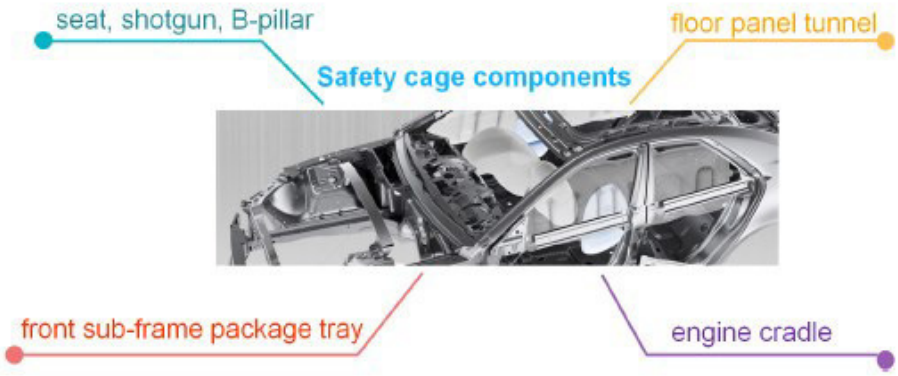

Fig. 28 *DP600 for automotive applications [131].*

Multiphase (MP) steels or Complex Phase (CP) affords higher level of yield strength at the same comparable tensile strength levels of dual phase steels [129]. CP steels mechanical characteristics are high energy absorption, high residual deformation capacity. They are used in automotive industry for frame rails, chassis components, transverse beams, B-pillar reinforcements, tunnel stiffener, rear suspension brackets, fender beam, rear frame rail reinforcements [132].

Moreover, TRIP (transformation induced plasticity) steel exhibit: high strength, good elongation and high energy absorption. Their application in automotive field are frame rails, rail reinforcements, side rail, crash box, dash panel, roof rails, B-pillar upper, roof rail, front and rear rails [129, 132]. The Martensitic Steel (MS) steels exhibit a martensitic matrix with small amounts of ferrite and/or bainite. Their exhibit high ultimate tensile strength level up to 1700 MPa [129].

TWIP (Twinning-induced plasticity steel) steels shows high strength (>1000 MPa) with high elasticity. However, adding high manganese content (17-24%) causes the steel to be fully austenitic at room temperatures. The presence of twins in the base material causes a large deformation [129]. Some studies have exposed the importance of hybrid laser welding of TWIP and DP steels with an austenitic filler, which avoids the formation of brittle martensite regions and manganese segregations in the fusion zone [123, 133].

1.6.3. Aluminum alloy weldability

Nowadays aluminum alloys used in automotive field has been constantly increasing. The main reasons for the interest of aluminum alloys is due to good corrosion resistance, good formability and light weighting properties. Consequently, lightweight materials reduce the weight and improve fuel economy [134].

Aluminum castings have been used to various automobile components for a long period. For example, the material for engine blocks, is being substituted from cast iron to aluminum resulting in important weight reduction. In automotive applications, aluminum castings have been used for almost 100% of pistons, about 75% of cylinder heads, 85% of intake manifolds and transmission [134]. However, wrought aluminum is becoming more active than applying aluminum castings. Nowadays the use of aluminum alloys is not limited to conventional castings, but includes, trunk lids, outer panels such as doors and protection covers including heat insulators [135]. For example, AA6181A alloy was used recently thanks to recycling features. For example, AA6181A alloy was used recently thanks to recycling characteristic. This alloy was employed for parts that require high strength with good formability. Moreover, AA6061 alloy used in car steering knuckles for instance, exhibit an average tensile strength of 383 MPa and elongation 10.7%. This alloy was improved by adding minor quantities of zirconium, zinc and copper. The alloy AA5182, is used for inner panels, present corrosion resistance and high formability, while its sister alloy AA5754 offers surface quality and is used in structural sheet applications [136, 137]. However, the welding of aluminum alloys has more problems compared to other industrial metals, such as steels. These difficulties are correlated with the physical properties of aluminum alloys, mainly their high reflectivity, high thermal conductivity, and low viscosity [138, 139]. Noticeably, aluminum alloys have high thermal conductivity that causes a rapid heat transfer when the aluminum alloys are exposed to a laser beam. To this purpose, high density energies are necessary for welding, and higher power distribution is needed to reach the melting temperature of the welding zones. Another important factor limiting the weldability of the aluminum alloys is their high reflectivity. The radiation absorption of this alloys depends on the input laser wavelength. Particularly dissimilar aluminum-steel joints have widely used in aeronautical and automotive industry. In those industries, the union of both low weight and high mechanical performances is a key factor in materials selection. The aluminum alloys are characterized by good recyclability, mechanical characteristics medium-high, and low cost, while steels by very high specific resistance and corrosion. The binary system Al-Fe [140] is characterized by limited solubility, consequently intermetallic phase formation occurs. Intermetallic phases include Fe-rich compounds (FeAl and Fe_3Al) and Al-rich compounds ($FeAl_2$, Fe_2Al_5, and $FeAl_3$), respectively. The mechanical properties of dissimilar joints are strongly correlated to the formation of IMC layer, and to its morphology. Consequently, the interface zone is often related with crack propagation or crack initiation during tensile test.

1.7. Laboratory of Innovative Techniques for Advanced Materials Welding (TISMA) DMMM Polytechnic of Bari

Similar and dissimilar welds were performed in the TISMA laboratory of Bari. The TISMA laboratory is focused to promote the development of new skills, technologies and processes for the regional economy and for the manufactories industry. In the TISMA laboratory three welding technologies, in detail the

laser beam, the electric arc and the friction stir welding, are coupled in order to test the welding capacities of classic and advanced and high-performance materials.

Fig. 29 *Equipment of the TISMA laboratory*

Combining simultaneously these heat sources a wide range of innovative materials, with low weldability and difficult to weld with technology traditional welding techniques, could be welded. For example, the combination of hybrid laser and arc welding offers many advantages, if compared to laser or arc welding, such as an increase of welding speed, stability of the process, and consequently, a high bead quality.
The equipment of the TISMA laboratory:

- Laser Fiber Ytterbium source (4kW);
- Laser/Arc Hybrid Welding Station (CNC - 5 axis);
- Hybrid Welding Station FSW/Laser & FSW/Arc (3 axis – 18kW);
- MIG/MAG Generator (500A);
- TIG Generator (500A).

1.8. Finite Element Model (FEM) for the welding process

Nowadays is possible simulate the welding technology in order to test the weld quality, the influence of welding parameters on the metallurgical aspect and the plates stresses and deformation during the welding process. This aspect is one of the principal factors affecting the lifetime of the welded [141-143].

A welding process is a complex process that includes numerous different non-linear physical phenomena, that influences the final properties of the joint. Therefore, the simulation of this process is very difficult for several reason. The first problem concerns the mathematical description of phenomena; consequently, simplifications and assumptions are required due to the excessive computational time. The welding simulation are interested with three main areas: 1) Process simulation, 2) Material simulation, 3) Structure simulation [144].

The welding simulation concerns the description of the molten pool formation and the fluid flow dynamics inside the fusion zone, considering the acting physical phenomena and the resulting local temperature field. The material simulation concerns the microstructural development during and after the welding process in the weld seam. Principally the hardness, the microstructural phase transformation, the hot and cold cracking are the principal themes of the welding simulation. The structure simulation defines the process effects on the adjacent structure, in terms of global temperature field and resulting residual stresses and distortions of the welded joint.

The method for calculation and simulation of welding process is Finite Element Analysis (FEA). This technique consist of subdivides a big problem into simpler discrete parts that are called finite elements, for each part partial differential equations are applied. The aerospace industry is the first field in which FEA was applied. Today the Finite Element Analysis can be used in different types of simulations: structural, thermal, electromagnetic etc.

Finite element method includes different steps. The first phase is to produce or import the model from a CAD program, the model must be as simple as possible. Further step is to mesh the geometry, so the volume is divided into small elements that approximates a geometry. Consequently, the size and the shape of the single element are significant factor for computation time and for accuracy of the solution. Next step is to apply boundary conditions and load, which are severely dependent from the process that must be simulated. Finally, the results are displayed with contour plots and can be examined.

A significant step in the welding simulation techniques is to determine the heat source model by examining experimental measurements, for example the size and shape of the fusion zone.

1.8.1. Heat source model for the laser beam

The first heat source model for a 2D numerical laser welding process, has been employed onto a thin plate. This heat flux model has been employed for sheet metal welding processes since temperature gradient was supposed constant in the direction of thickness. Later, other researchers [145] study the influence of heat flow through the weld thickness applying the conical Gaussian heat source model [146, 147]. This volumetric heat source model is frequently used for many 3D simulations in deep penetration laser welding. Fig. 30 shows a 3D heat source model.

In this model, the Gaussian distribution is maximum at top surface of the plates and minimum at the bottom surface.

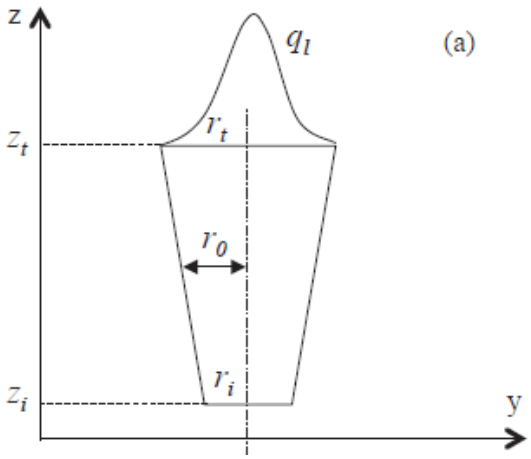

Fig. 30 *Gaussian heat source model [148].*

A moving laser heat source can be mathematically expressed as following Eq. 6 [148, 149]:

$$Q_r = Q_o \exp(\frac{-r^2}{r_o^2}) \quad \text{Eq. 6}$$

with

$$r = \sqrt{x^2 + y^2} \quad \text{Eq. 7}$$

Where Q_r represent heat source intensity, Q_0 is the maximum intensity, r_u and r_i describe upper and the lower radius in the upper plane at $z=z_u$ and in the lower plane at $z=z_l$ respectively.

1.8.2. Heat source model for the hybrid laser-arc welding

Goldak et al. [149-151] developed a double-ellipsoidal heat source model to describe the arc power on the molten pool. The heat source was described by two different half-ellipses: the at front (q_f) and rear (q_r) volumetric heat flux respectively.

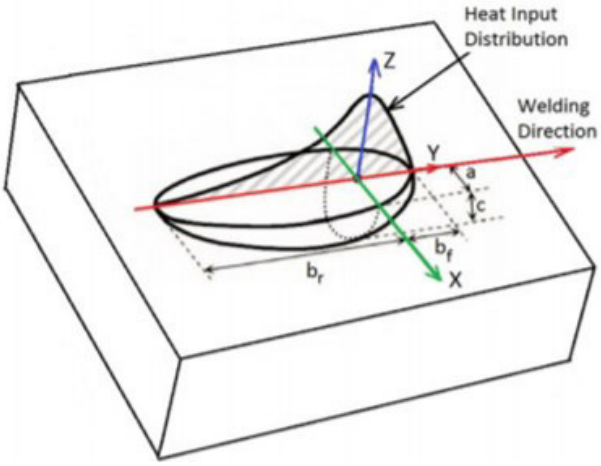

Fig. 31 *Goldak heat source model [152].*

A moving arc heat source in the plates can be mathematically defined as sum Q (x, y, z)= q_f (x, y, z)+ q_r (x, y, z) [149]. In particular, the mathematical definition of the double-ellipsoidal heat source was described as:

$$q_f = \frac{6\sqrt{3}f_f Q}{a_f bd\sqrt{\pi}} * \exp(-\frac{3(x-vt)^2}{a_f^2} - \frac{3y^2}{b^2} - \frac{3z^2}{d^2}) \quad \text{Eq. 8}$$

$$q_r = \frac{6\sqrt{3}f_r Q}{a_r bd\sqrt{\pi}} * exp(-\frac{3(x-vt)^2}{a_r^2} - \frac{3y^2}{b^2} - \frac{3z^2}{d^2}) \quad \text{Eq. 9}$$

Moreover, a_f represent front length, a_r is rear length, b and d are the width and the depth, respectively (see Fig. 31). While v is the welding speed, f_f and f_r are the proportion coefficients at front and rear ellipsoids and Q is arc power that is calculated of the following Eq. 10:

$$Q_{a=\eta_a} IU \quad \text{Eq. 10}$$

Where Q_a is the arc power; I is the arc current; U represents the arc voltage; and η_a is the arc heat efficiency.

2. CHAPTER: Laser/TIG weldability of AISI 304 and AISI 410 dissimilar weld

In this chapter, the Laser/TIG weldability of AISI 304 and AISI 410 have been analyzed. In order to define the best combination of process parameters that produces high performance in terms of ultimate tensile strength, the welding parameters (laser line energy and arc current), have been varied, each one in a range of values which were defined in former laser-TIG welding experiments of other ferrous materials. Nevertheless, no studies have been published concerning fiber laser-TIG hybrid welding of dissimilar stainless steel. The goal is the realization of the AISI 304 and AISI 410 stainless steel dissimilar weld by means of an innovative fiber laser-TIG hybrid welding. However, welding of dissimilar joints is difficult due to the physical, thermal and the chemical differences between the two materials.
The stainless steel used in the present study are widely used for industrial applications. Austenitic stainless steel exhibit excellent formability, good corrosion resistance, and high strength and are employed, especially, in automotive, industrial equipment and petrochemical industries. Future growth in the use of austenitic stainless steel is planned for automotive industries, due to their unique good fatigue resistance and formability. While martensitic steels are also suitable for applications where the material is subjected to both corrosion and wear [153, 154].

2.1. Experimental procedure

2.1.1. Welding configuration and method

An innovative fiber-laser TIG welding has been investigated. A fiber laser Ytterbium Laser System (IPG YLS-4000), with a maximum available power output of 4 kW was employed in continuous wave regime (see Tab. 1). An Ytterbium-doped fiber laser is better than traditional lasers, which uses solid or gas active medium. The laser beam was focused perpendicularly on the surface of the sheet. The experimental analysis of the AISI 304 and AISI 410 stainless steel dissimilar weld was reported. The heat laser source was coupled with a TIG generator (SELCO GENESIS 504 PSR). TIG torch tilting angle was 40°, and the laser beam was focused perpendicularly on the surface of the sheet.
The characteristics of the laser are indicated in term of fiber diameter, beam parameter product (BPP), wavelength, focal distance and spot diameter.

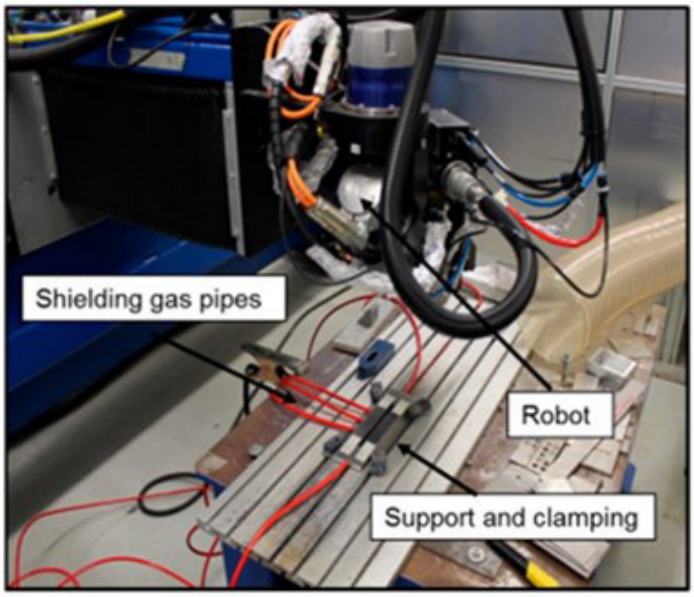

Fig. 32 *Experimental set-up [155].*

Diameter fiber (µm)	Beam parameter product (BPP) (mm*mrad)	Wavelength (nm)	Focal Distance (mm)	Spot diameter (mm)
200	6.3	1070.6	250	0.4

Tab. 1 *Laser parameters.*

A laser leading configuration was used. The laser beam was the primary heat source. The weld had a better shape and deeper penetration. Therefore, the laser beam offers high welding speed and stabilizes the electrical arc [93]. In this case, the distance between the two sources was equal to 3 mm (DLA).

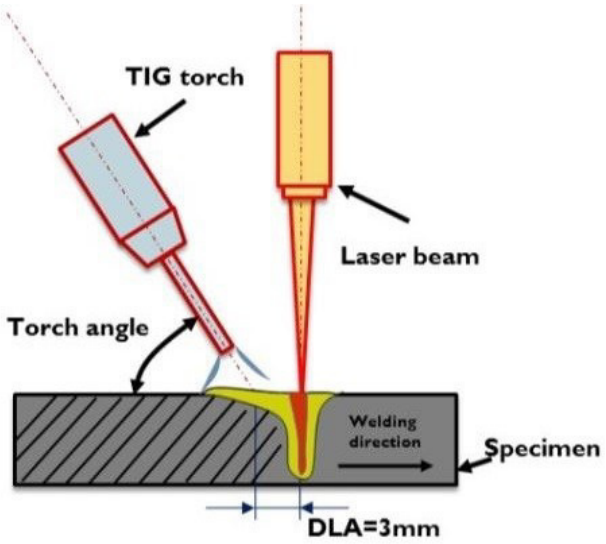

Fig. 33 *Fiber laser -TIG hybrid welding system [156].*

Sample	Laser power (W)	Welding speed (m/min)	TIG current (A)	TIG Voltage (V)	Laser Line Energy (J/mm)	Arc Line Energy (J/mm)
S1	3300	2.2	150	24.5	90	100
S2	3700	2.3	150	24.5	96	96
S3	3000	2.0	250	21.5	90	161
S4	4000	2.5	250	21.5	96	129

Tab. 2 *Experimental plane [156].*

Moreover, the dimensions of the plates (length x width x thickness) for the butt welding were 100 mm × 80 mm × 6 mm. In order to preserve the weld, the shielding gas adopted was Argon. The configuration of the experiment was shown in Fig. 33. Tab. 2 shows the experimental plan.

Laser line energy (Q_{laser}) and arc line energy (Q_{arc}) were given from by the following equations [157, 158] according to the experimental plan shown in Tab. 2:

$$Q_{laser} = 60 * \frac{P_l}{S} \left(\frac{J}{mm}\right) \quad \text{Eq. 11}$$

$$Q_{arc} = 60 * V * \frac{I}{S} \left(\frac{J}{mm}\right) \quad \text{Eq. 12}$$

Where P_l is the laser power (W), V is the TIG voltage (V), I is the TIG current (A) and S is the welding speed (mm/min). The joints microstructure was investigated using a Nikon Epiphot 200 optical microscope (OM). Transversal sections of welds were subjected to a standard metallographic preparative and etching for the characterization.

In order to observe the microstructures, the Vilella reagent (1 g of picric acid, 5 ml of HCl, 100 ml of ethanol) for martensitic stainless steel and Glyceregia reagent (15 ml HCl, 15 ml glycerol, 5 ml HNO_3) to for austenitic microstructure were used. The residual stresses were measured on two representative specimens (S1 and S3).

The residual stresses were calculated, using X_{stress} 3000 G3R Stresstech X-ray diffractometer (Stresstech Oy, Vaajakoski, Finland). For AISI 410 measurement, the Xray diffractometer was equipped with the Cr tube (λ=0.2291 nm) and 2mm collimator. The X-ray voltage was equal to 30 kV while the X-ray current was equal to 8 mA. Instead, to measure AISI 304 side, the Mn tube (λ=0.210314 nm) powered by 30 kV voltage and 8 mA arc current was used.

Finally, the mechanical properties were analyzed. Specimens were subjected to Vickers micro-hardness measurement (Affri Wiky 200JS2), with a load of 0.3 kg for 15s, and to tensile test. The fracture surfaces were studied by Zeiss EVO scanning electron microscope (SEM) using an accelerating voltage of 20 kV. The tensile tests were conducted with a 20 KN Ingstrom tensile test machine.

2.1.2. Base Material

The chemical compositions of AISI 304 and AISI 410 stainless steel was reported in Tab. 3. AISI 304 is an austenitic stainless steel and AISI 410 is a martensitic stainless steel. Both steels are cold rolled, in annealed condition, pickled and skin passed.

METAL	C	Cr	Mn	Ni	P	S	Si	Fe
AISI 304	0.08	18,0-20,0	2,0	8,0-10,5	0.045	0,03	1,00	balance
AISI 410	0,15	11,5-13,5	1,00	-	0,04	0,03	1,00	balance

Tab. 3 *Chemical composition of AISI 304 and AISI 410 (wt.%) [156].*

2.2. Base Material characterization

The optical microstructure of AISI 410, in annealed condition, comprised of a matrix of equiaxed ferrite grains (Fig. 34a). The structure present a micro-hardness value equal to 159 ± 5.5 HV0.3 Microstructure of the base material (BM) AISI 304, exhibited a typical fully austenitic structure with stringers of delta ferrite (Fig. 34b). This alloy presented a Vickers micro-hardness value equal to 191.6 ± 4.5 HV0.3.

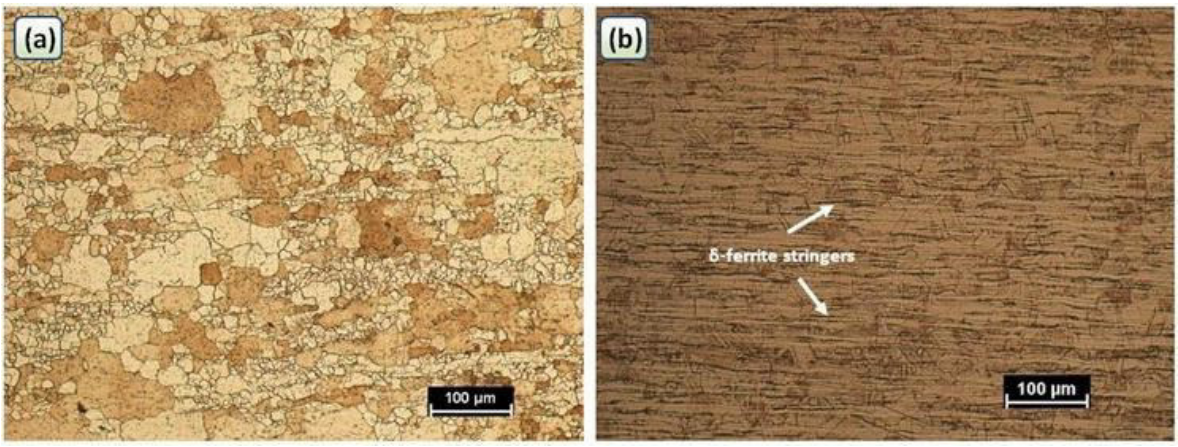

Fig. 34 *Optical micrographs shows* microstructure of the (a) martensitic stainless steel AISI 410 and the (b) austenitic AISI 304 as *received [156].*

2.3. Results and discussion

2.3.1. Weld shape and microstructure

The cross sections of the dissimilar joints S1, S2, S3 and S4, after standard preparative metallographic and chemical etching, is showed in Fig. 35. Moreover, all joints were exhibit incomplete penetration. All samples presented local porosity, which was severely associated to many conditions regarding the material and the welding technique.

The macro graphics of all the joints cross sections at Optical Microscopy (OM), exhibited the typical "wine-cup" shape constituted by two zones: laser zone (LZ) and crown zone (CZ) (Fig. 36) [112, 159]. In Fig. 36 is precisely described the classic shape of the joints, with indication of the different zones.

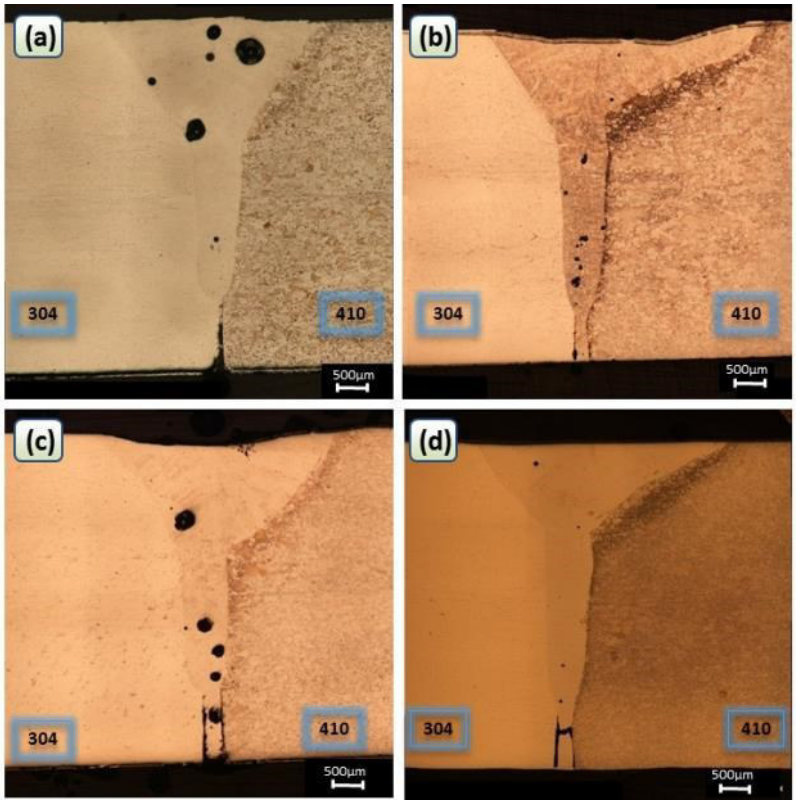

Fig. 35 *Optical macrographs of the joints cross-sections: a) S1; b) S2; c) S3; d) S4 [156].*

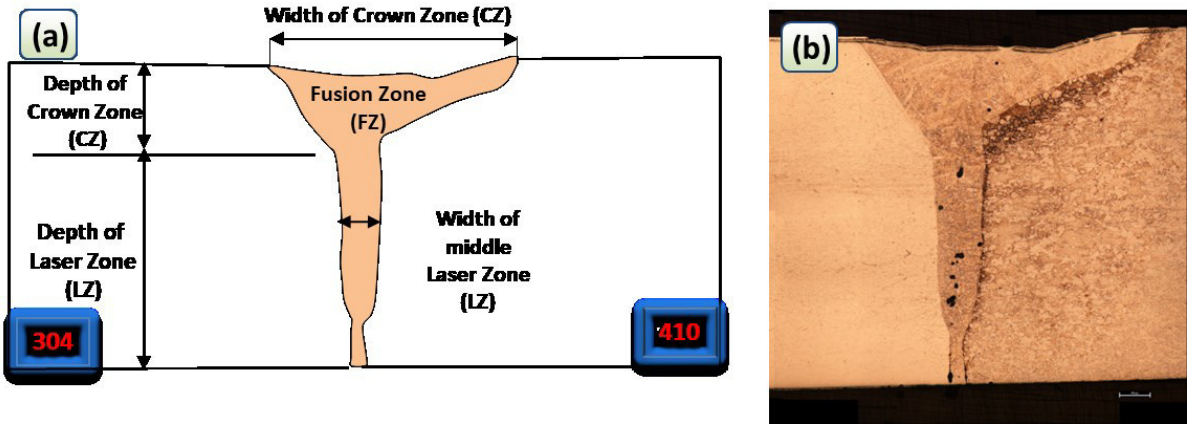

Fig. 36 *(a) Sketch of cross section; (b) Macro-graph of the joint shape [156].*

During hybrid welding the energy distribution from heat source, in the weld zone, is different. The extension of crown zone was affected from the arc energy. Consequently, the following relationship between the Depth of Crown Zone (DCZ) and arc line energy was detected: DCZ decreased with a lower arc line energy, due to higher welding speed. However, the laser energy favored the deep penetration in

the bottom, generating the typical keyhole shape and consequently the laser zone [87, 160]. Therefore, many researchers confer the deep penetration to the laser power and not to the arc current [87, 161-162]. Fig. 37 shows the relationship between the laser beam penetration, or depth of laser zone (DLZ), and laser line energy: the DLZ increased with laser line energy.

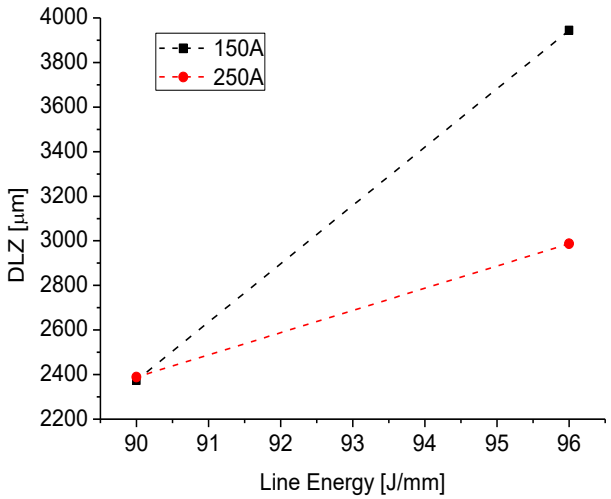

Fig. 37 *Relationship between laser beam penetration (DLZ) and laser line energy [156].*

Significant indications were achieved from the variation of laser line energy and TIG current. Therefore, that increasing the laser line energy only by 6.67%, the DLZ could grow up to about 66% with the same TIG current (see Fig. 37).

By optical microscope, a predominant martensitic microstructure in fusion zone (FZ) has been observed (Fig. 38).

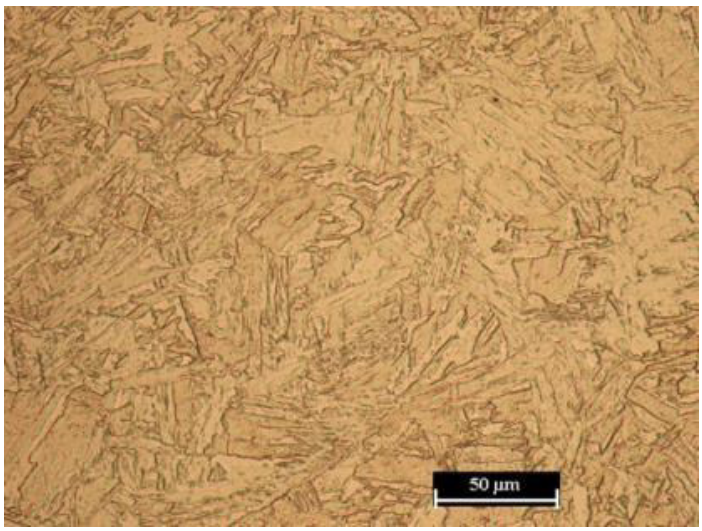

Fig. 38 *Optical micrograph of FZ showing a prevalent martensitic microstructure [156].*

Moreover, different heat-affected zone (HAZ) has been observed. In the HAZ of austenitic stainless steel, due to the high cooling speed, stringers of untreated ferrite delta (δ) has been observed (Fig. 39). However, the existence of untreated ferrite δ can modify the properties of AISI 304, as, high resistance to corrosion, due to the high percentage of chromium, low fatigue resistance [163, 164]. Moreover, the formation of ferrite δ can promote the reduce the growth of grains in the HAZ of the austenitic stainless steel [165].

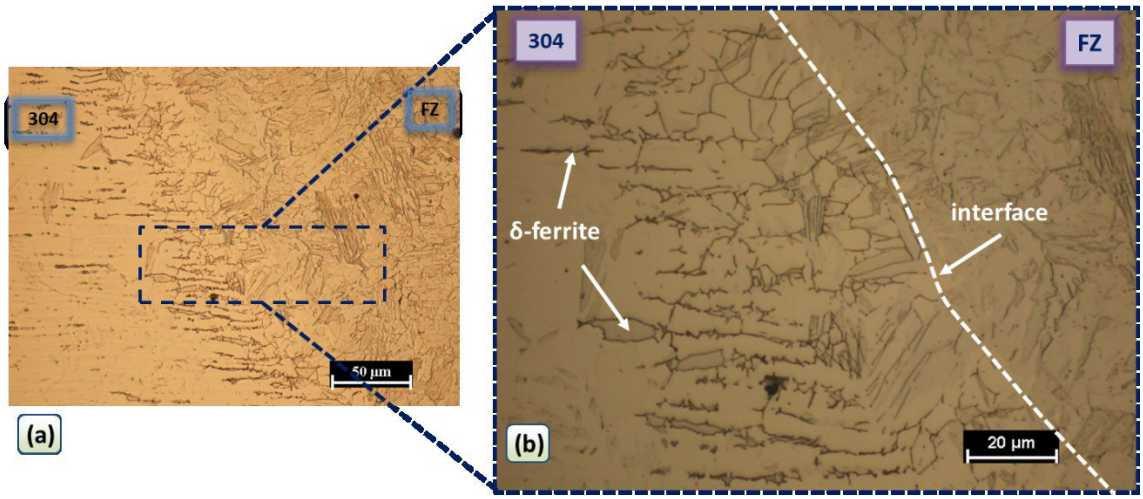

Fig. 39 *(a) Optical micrograph shows the interface of HAZ zone, between AISI 304 BM and FZ, at 500x; (b) Interface zoom-up of selected area at 1000×[156].*

While, at the interface between martensitic stainless steel and fusion zone, was observed a continuous layer of martensite at the ferrite grains boundaries, this layer is due to elevated temperature that are reached at the fusion boundary (see Fig. 40).

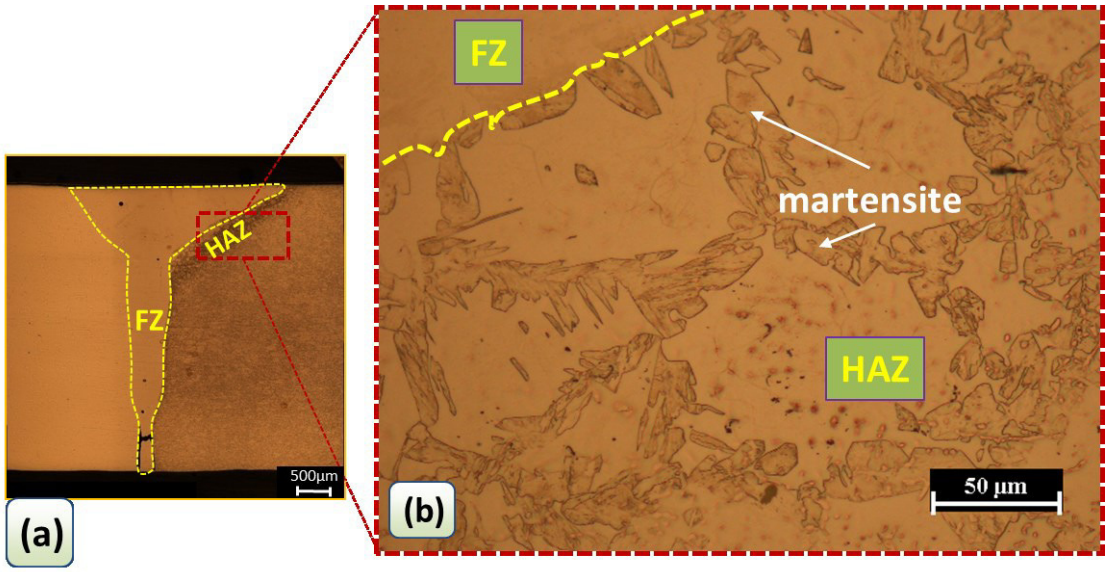

Fig. 40 *Optical macrograph of the joint S4 showing HAZ between FZ and AISI 410 BM; (b) high-magnification image of selected area at 500× [156].*

In particular, at the interface between martensitic stainless steel and fusion zone, the grain size progressively increased from the edge of HAZ to the fusion boundary (Fig. 41). Consequently, grain coarsening effect was a function of temperature as well.

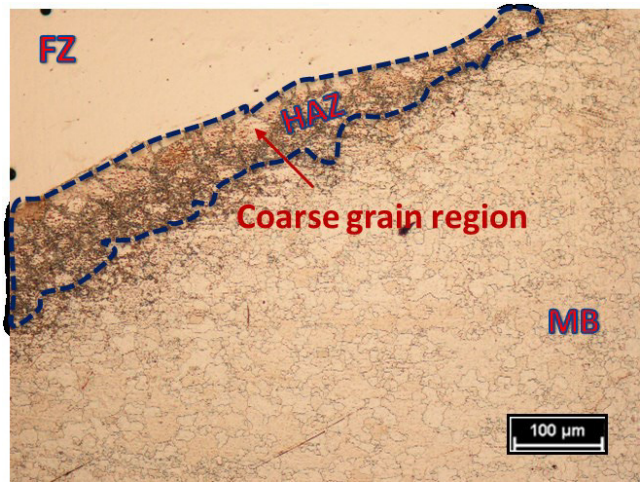

Fig. 41 *Grain coarsening effect in HAZ at the martensitic side [156].*

Therefore, by means Nikon's NIS-Elements imaging software the quantity of martensite has been evaluated. Consequently, it was analyzed that the percentage of martensite increased significantly when the laser line energy decreased (Fig. 40). In fact, this result is due to high temperature and therefore the martensite had not enough time for the growth [166].

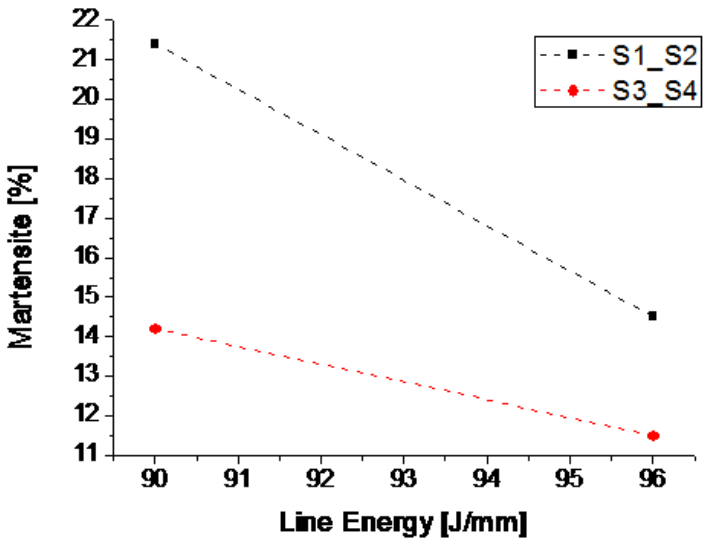

Fig. 42 *Martensite [%] versus laser line energy [156].*

2.3.2. Defects

All the observed joints presented porosity in the FZ that was probably due to the vapors and gases which remains entrapped in the molten movements. It is well known that porosity in hybrid laser arc welding can easily occur, due to the instability of keyhole [167-169]. The graph Fig. 43 displays the effect of arc current on porosity.

The percentage of porosity was estimated using an image processing software and evaluated as $\Sigma Area_{pores}/Area_{tot}$. The graph shows as the porosity decreased with the inverse of the arc current. In particular, Fig. 43 shows, as the quantity of porosity was very high in the welds that exhibit laser line energy of 90 J/mm and lower in the joints with laser line energy of 96 J/mm.

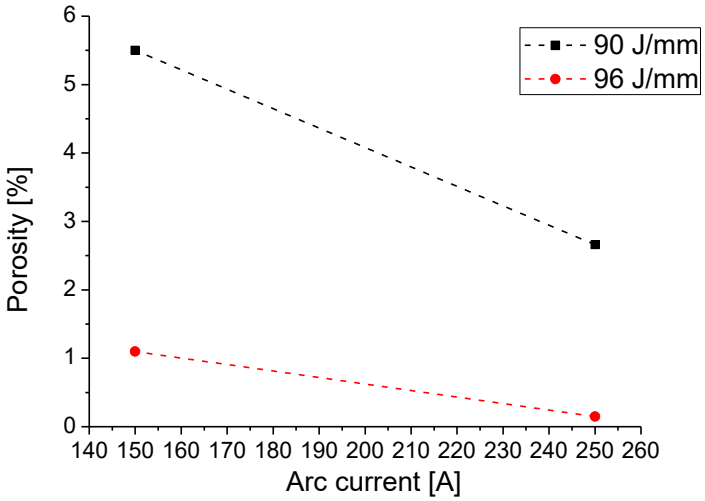

Fig. 43 *Porosity [%] versus arc current [A] [156].*

Moreover, the porosity reached the maximum value in correspondence with the minimum values of both the laser line energy and the arc current. Porosities did not have time to escape from the fusion zone before solidification.

2.3.3. Micro-hardness test

Micro-hardness profiles have been obtained at the middle-height of the cross section at fixed distance. All welds showed the same trend and maximum micro-hardness. In Fig. 44 the micro-hardness profile for joint S1 is reported. The micro-hardness was very high in the FZ where the microstructure was martensitic. In FZ microhardness increased up to an average value of about 350 HV.

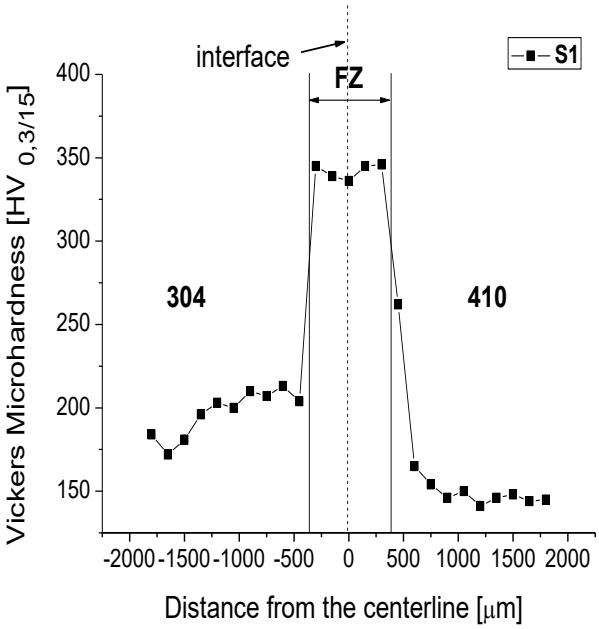

Fig. 44 *Cross weld section micro-hardness profile [156].*

No grain grown was observed in the zone between AISI 304 stainless steel fusion zone and HAZ, which can be explained by the fact that high cooling rate promoted by to steeper thermal gradient (Fig. 45). Some authors it was also reported that the formation of ferrite stringers along HAZ grain boundaries limit the grain growth [165]. In HAZ of AISI 410 martensitic stainless steel the rise of hardness, compared to the base material, was due to the growth of martensitic along the ferritic boundary grain.

Fig. 45 *Interface between fusion zone and austenitic stainless steel [156].*

2.3.4. Residual stresses

In this work, residual stresses were measured on two representative specimens (S1 and S3), to study in which manner they develop in the dissimilar stainless steel welded by laser-arc hybrid welding. The stress

was measured at different angles (0°, $\pm 22.5^{\circ}$, $\pm 45^{\circ}$) setting a tilt oscillation φ of$\pm 3^{\circ}$ and an exposition time of 40 s, to increase the deep penetration of the beam and to avoid the shear effects. The detection distance equaled 50 mm. The residual stress was measured along the center line (x=0) of the joints in two directions for each point (Fig. 46): normal ($\sigma_{\perp}$ in y-direction) and longitudinal ($\sigma_{/\!/}$ in x-direction) both on the top and the bottom surface.

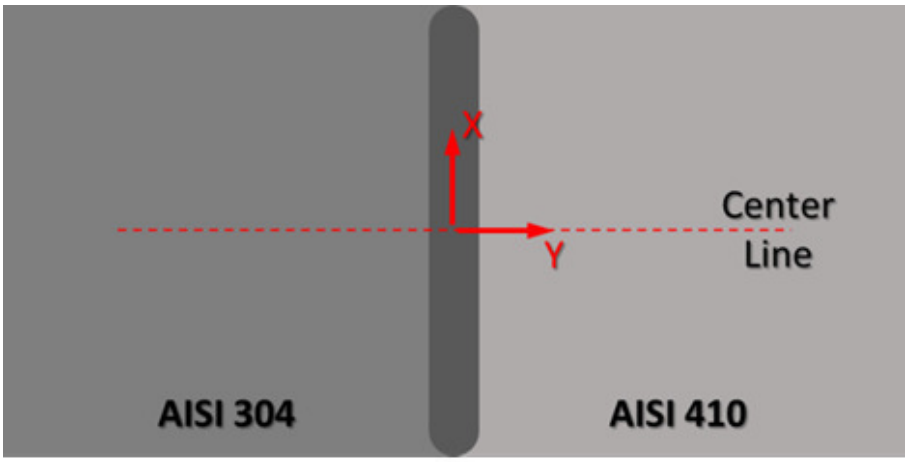

Fig. 46 *Sketch of the weld with the coordinate system and the measure lines [156].*

On top surface, the longitudinal stress increased from 1mm to 2.5 mm from the weld and after decreased to the values of the base metal for both materials (Fig. 47a). It was observed that the values of $\sigma_{/\!/}$ on AISI 304 side were higher than those measured on AISI 410 side. In fact, the highest value of $\sigma_{/\!/}$ (137 MPa) has been measured in AISI 304 at 2.5mm from the weld (case S1). On the top surface, the S3 set parameters appeared to guarantee the lowest values of $\sigma_{/\!/}$ in both materials Normal stresses, still on the top surface (Fig. 47b), showed a similar trend to longitudinal stresses but all measured values were in compression.

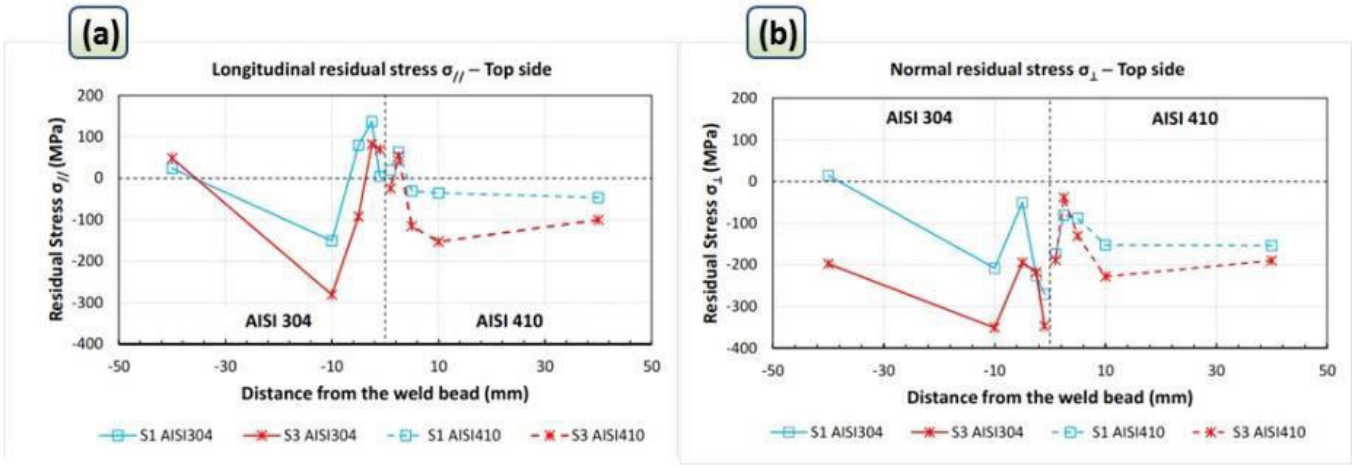

Fig. 47 *(a) Longitudinal residual stresses and (b) Normal residual stresses in transversal section (top side) [156].*

On the bottom side, the maximum longitudinal stress (130.4 MPa) was measured at 1mm to the weld line for specimen S1, on AISI 410 side (Fig. 48a), while the other values measured in both material and specimens were in compression. Finally, also on the bottom side, $\sigma_{\perp}$ (Fig. 48b) had quite the same trend of $\sigma_{//}$ but all the values were in compression.

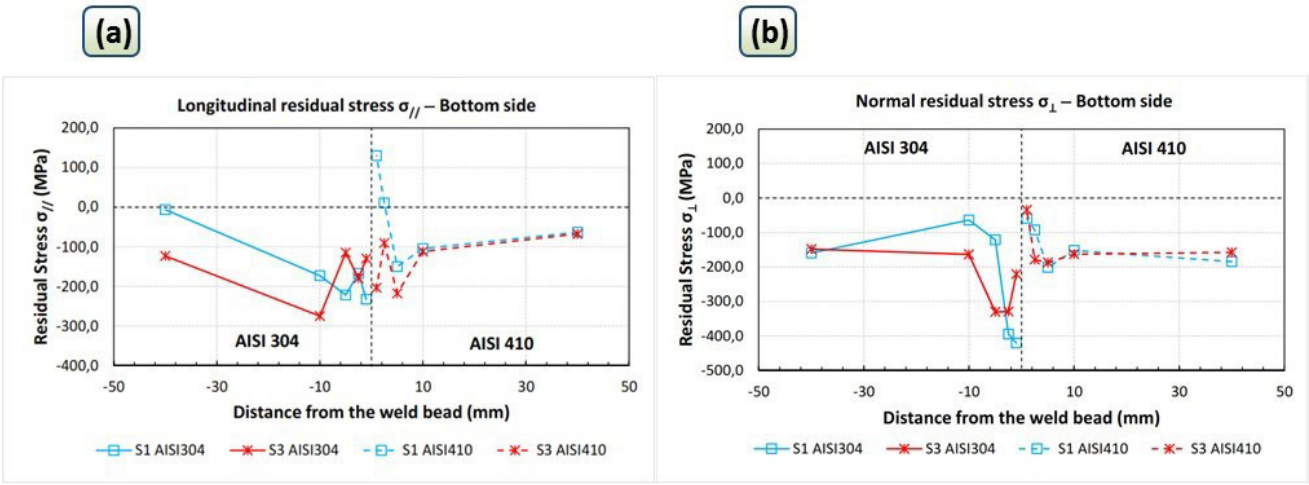

Fig. 48 *(a) Longitudinal residual stresses and (b) Normal residual stresses in transversal section (bottom side) [156].*

In conclusion, the compression state evaluated also near the weld bead can depend different factors: boundary conditions, on lack of complete penetration, original residual stress state of the plates, and the smallness of the HAZ. In fact, the final residual stress state is the consequence of the stress history of the component.

2.3.5. Tensile properties and fractography

In hybrid laser welding the mechanical properties are also influenced by high percentage of martensite existing in HAZ.

Consequently, the fracture occurs when high percentage martensite in HAZ, is incapable to deform at the same degree and at the same rate as the weld and base metal.

Therefore, the grain growth and martensite formation in HAZ, at AISI 410 side, are principal factors in tensile strength.

During tensile test all specimens cracked in the HAZ zone of the martensitic stainless steel (Fig. 49), and after the rupture the fracture surfaces have been observed to Zeiss EVO scanning electron microscope (SEM).

Particularly, fracture arose from the bottom side and propagated throughout the entire section mainly along the welding centerline. Particularly, fracture arose from the bottom side and propagated throughout along the whole thickness of the plates following the shape of HAZ.

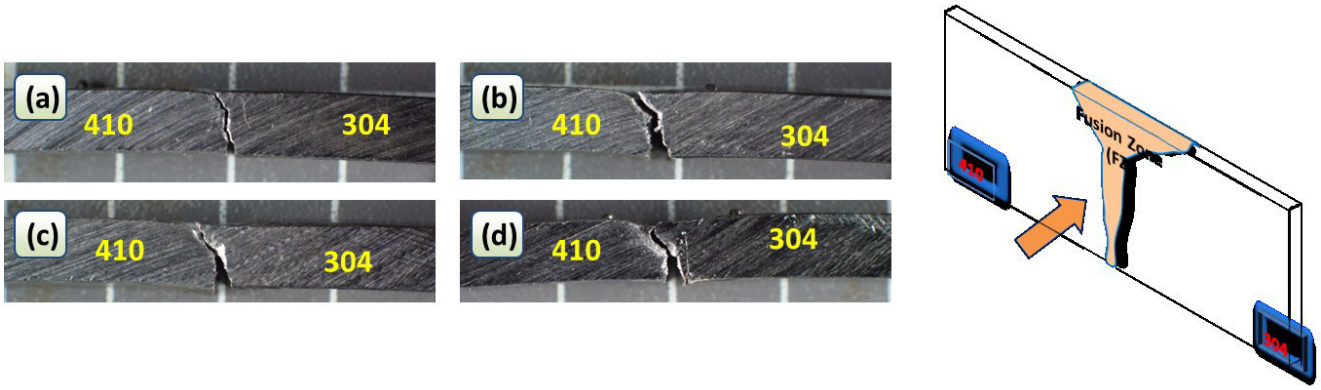

Fig. 49 *Photographs presenting the position of fracture in welds (a) S1, (b) S2, (c) S3 and (d) S4 after tensile tests (cross section) [156].*

In Fig. 50 the results of tensile test performed on the sample S4 are presented. SEM fractography showed small and large conical dimples characterized the rough fracture surfaces (Fig. 50c). Moreover, the presence of cleavage plane with voids indicates that the mode of failure was brittle (Fig. 50d).

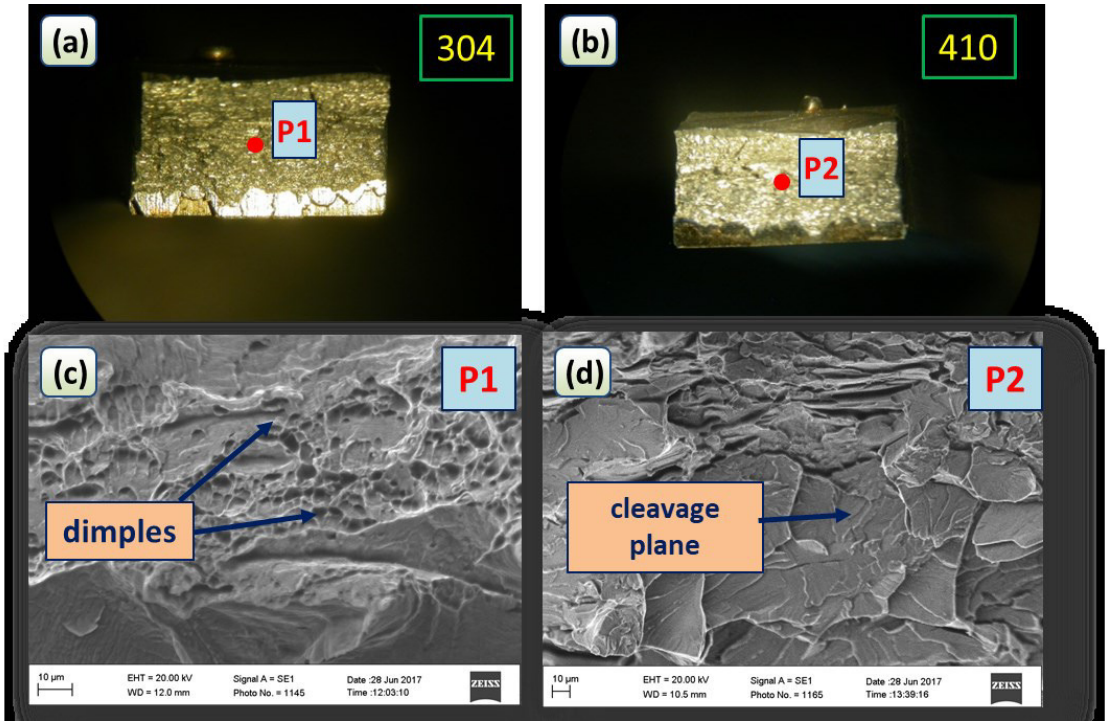

Fig. 50 *Photographs of the (a) austenitic steel side and (b) martensitic steel side of the tensile tested sample; SEM fractography of the highlighted points (c) P1 and (d) P2 [156].*

In the Tab. 4 values of the yield stress (σ_y), ultimate tensile strength (UTS) and strain at fracture (elongation ε_{max}) for the samples were definite.

Sample	UTS [MPa]	ε_{max} [%]	σ_y [MPa]
S1	360	3.29	268
S2	354	3.09	281
S3	301	4.06	272
S4	391	4.87	285

Tab. 4 *Tensile properties for joints S1, S2, S3 an S4 [156].*

The tensile stress-strain curves obtained were shown in Fig. 51.

As above mentioned, the fracture started from that gap at the weld root, being an area with a higher concentration of stress.

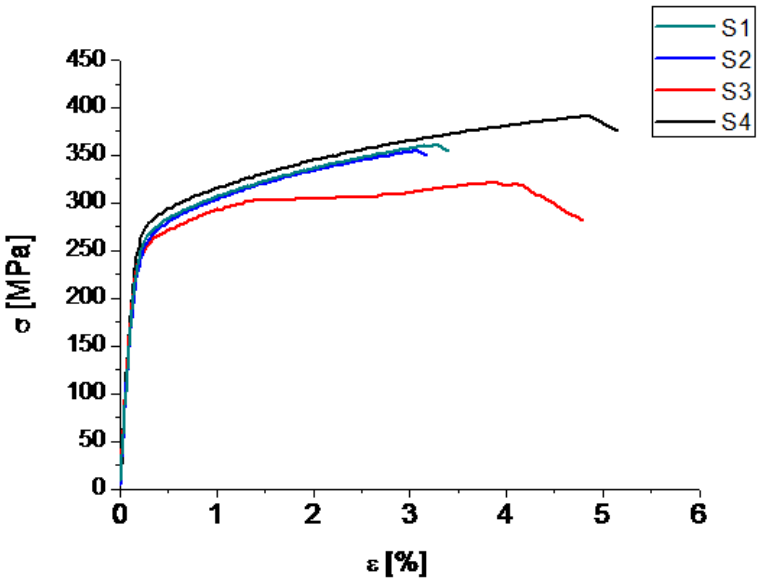

Fig. 51 *Tensile stress–strain curves [156].*

As all the specimens were afflicted by this problem, it has been executed a comparative evaluation of the behavior of the welds with the variation of the considered process parameters. The sample S4 exhibited the highest elongation and the best tensile strength, having the smallest percentage of martensite (see Fig. 42).

3. CHAPTER: Weldability of TWIP and DP steel dissimilar joint by laser arc hybrid welding with austenitic filler

In this study TWIP steel has been welded with DP steel, and the microstructural and mechanical characteristics of TWIP/DP dissimilar butt joints have been investigated.

The steels used in the present study are used automobile industries, and the laminates sheets, with thickness of 1.5 millimeters, have been used in butt joints configuration. The main mechanical properties of these steels are high fracture straight, high energy absorption, formability and good fatigue resistance [170, 171]. The material choice for the future will aim to reduce weight and make the car safer. However, the manufacturing issues will play a major role in the choice.

Ytterbium fiber laser has confirmed its capability at welding a variety of similar and dissimilar metal joints [172, 173]. However, that laser can be coupled to an arc torch so to provide some advantages like high welding speed, low heat input, good process stability, arc stability, and weld penetration [102]. Some studies have revealed the importance of hybrid laser welding of TWIP and DP steels with austenitic filler, in order to avoid the formation of brittle martensite regions and Mn segregations in the molten pool [123]. Micro-hardness and tensile properties of the welds were analyzed, in order to understand the weldability of the TWIP-DP dissimilar joints.

3.1. Fiber laser MAG hybrid welding of DP/TWIP steel

DP and TWIP plates 1.6 mm thick have been welded in butt joints configuration as it is shown in the sketch in Fig. 52. An Ytterbium Laser System (IPG YLS-4000) has been used. The laser beam has been focused on the workpiece surface.

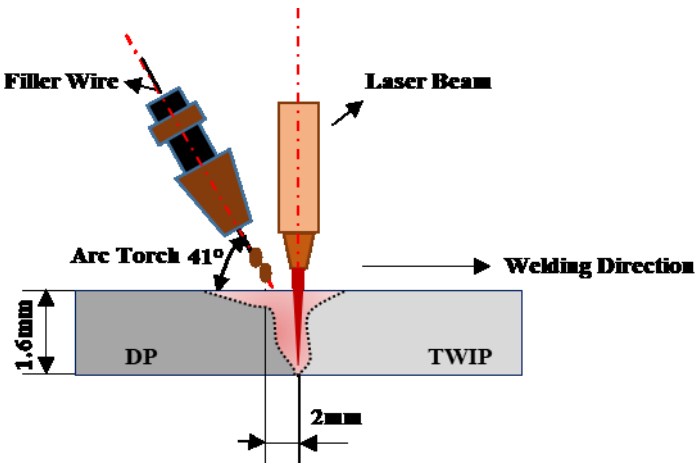

Fig. 52 *Sketch of the welding configuration.*

In the Tab. 5 is reported the chemical composition.

Sample	C	Si	Mn	Cr	Mo	Al	Ti
TWIP	0.66	0.2	23.4	0.13	0.12	0.04	-
DP	0.09	0.2	1.65	0.43	-	0.03	0.003

Tab. 5 *Chemical composition of TWIP and DP steel (wt.%) [174].*

Argon (87%) and carbon dioxide (13%) were employed as shielding gas. In order to reach acceptable results in term of bead appearance and mechanical strength, that mix was used. The laser source was orientated at the weld centerline. The torch angle was equal to 40°, while the laser beam was focused perpendicularly on the sheets surface. The distance between the two sources was equal to 2.5 mm. The filler material was 316L-Si/SKR-Si and its chemical composition is reported in Tab. 6.

	C	Si	Mn	Cr	Mo	Ni	Cu	P
Filler	0.016	0.82	1.65	18.1	2.57	12.33	0.03	0.023

Tab. 6 *Chemical composition of the 16L-Si/SKR-Si (wt.%)[174].*

In the experimental plan, three dissimilar joints have been obtained varying laser powers: 1250 W, 1500 and 1800 W, and with the welding speed equal a 2.7 m/min. The arc parameters have been imposed: a wire feed rate of 8.6 m/min with 20 V voltage and 94 A current. After etching with Glyceregia (15 cc HCl, 5cc HNO_3, 10 cc Glycerol) and Villella's (5 cc HCl, 2gr picric acid, 100 cc ethylic alcohol), the weld cross sections were observed using the optical microscope (OM). The dissimilar welds have undergone to micro-hardness and tensile tests. Particularly the Vickers micro-hardness test was performed with al load of 300gf and with a time of indentation of 15 sec.

3.2. Weld appearance and microstructure

The macro graphics of the joints cross sections at OM, presented two separated fused zones can be delineated (FZ-Upper and FZ-Below) (Fig. 53a). This phenomenon can be due to the displacement the laser source to the TWIP side, so can be one of the reasons why the filler wire did not melt appropriately. While, in Fig. 53b the filler wire and the base material mixed in a better way, thanks a high level of power. The high-power laser promoted a large fused zone. Moreover, there aren't defects in both samples.

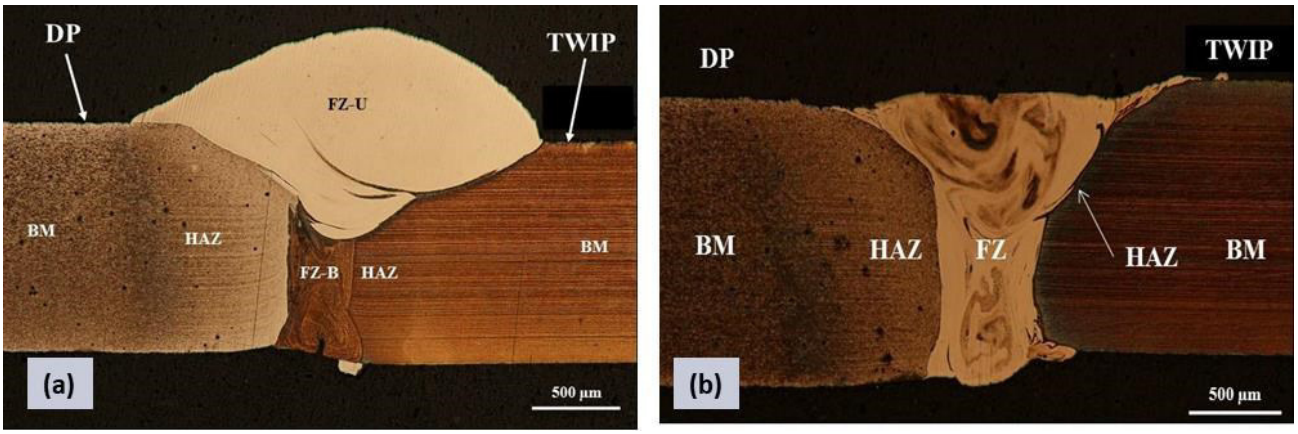

Fig. 53 *Cross section with partial mix between filler wire and base metal: (a) 1250W and (b) 1800W [174].*

In the Fig. 54 the microstructure inside the joints is reported. In the HAZ of DP side, the thermal cycle induced by the process promotes a martensitic transformation (Fig. 54a). The fusion zone exhibits a dendritic microstructure and the dendrite are straight (Fig. 54b). The dendritic growth from the edge of the molten pool and proceeds toward the weld centerline. Grain coarsening effect can also be seen on the TWIP side of both weldments (Fig. 54c). The grain coarsening effect was due to by low thermal conductivity of the TWIP steel. This causes heat accumulation, slower cooling, and coarsening in the TWIP side [175].

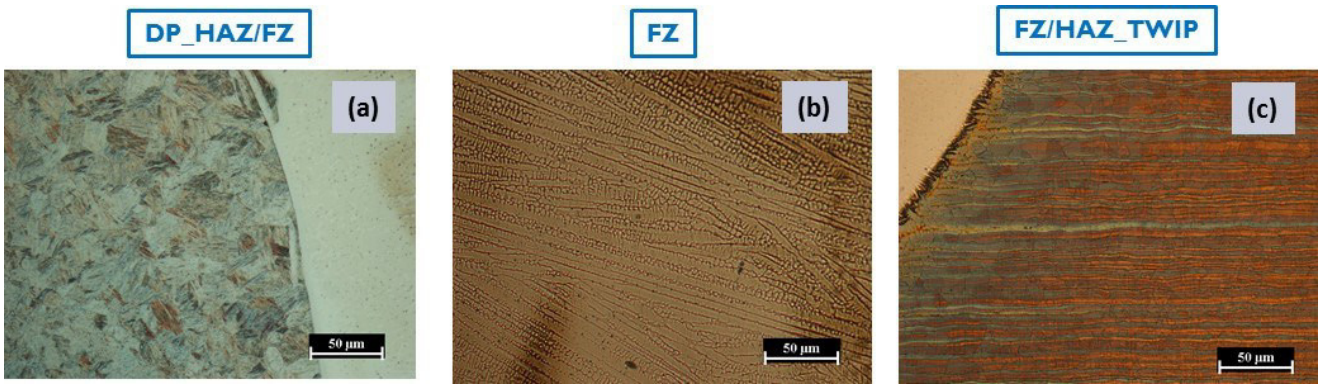

Fig. 54 *Microstructure of the different zones: (a) interface DP/FZ; (b) FZ and (c) interface FZ/TWIP [174].*

3.3. Mechanical testing

3.3.1. Micro hardness test

The micro-hardness in the transverse section of the welds was evaluated for both welds. In Fig. 55 are showed the micro-hardness profiles of the weld. The micro-hardness was very high in the DP HAZ where the microstructure was martensitic. The hardness of HAZ decreases with the decrease of content of martensite, and therefore increasing the distance from the interface FZ/DP_HAZ. The lower microhardness in the HAZ of TWIP was due to the grain coarsening effect. Moreover, both dissimilar

welds exhibit in FZ low microhardness values, which was caused by dendritic microstructures. In particular, in HAZ of DP steel, the hardness decreased under that of the base material due to a process named HAZ softening. This phenomenon is due to the formation of tempering martensite [176, 177]. Xia et al., [176] report HAZ softening can have a significant effect on weldment strength. As can be seen by tensile test.

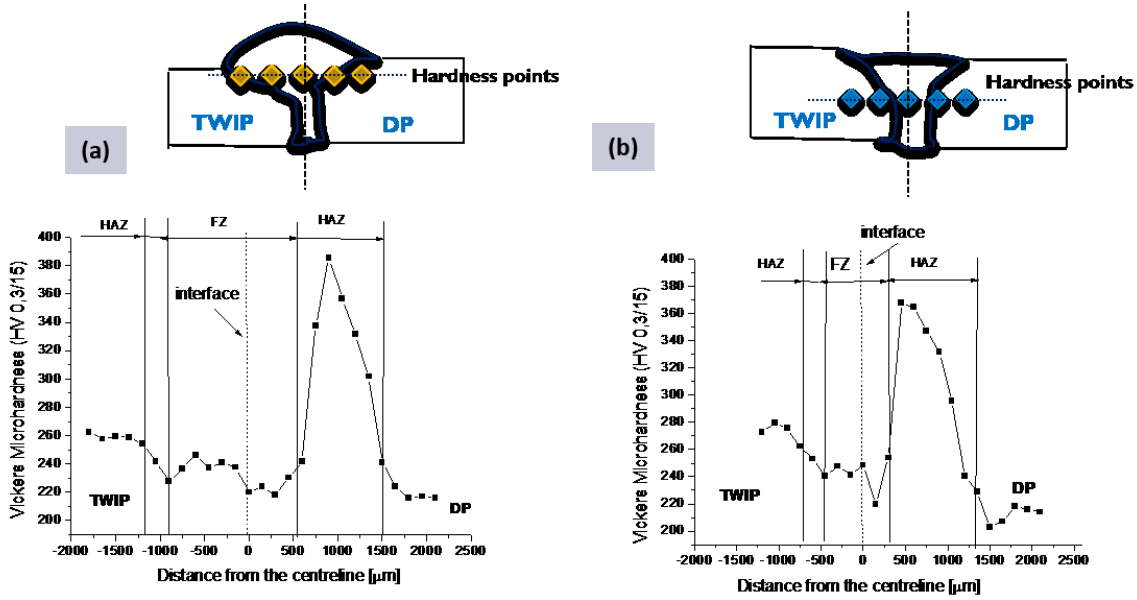

Fig. 55 *Vickers Micro-hardness profiles of the welds: (a) 1250W; (b) 1800W [174].*

3.3.2. Tensile test

For tensile test rectangular specimens 100 mm long and 10 mm width were cut transversal to the weld direction. A standard tensile test machine whose maximum load was 20 kN was used. Fig. 56 shows the stress strain curves. The welds showed a good strength and an appreciably elongation, see sample with 1800W laser power. During tensile test, both the specimens cracked in the BM of DP steel. Necking and failure occurred in the DP steel of base material (Fig. 56). The fracture in DP base material can be due to the presence of tempering martensite. This phenomenon can have detrimental effects on the weld strength.

Sample	UTS [MPa]	ε_{max} [mm]	σ_y [MPa]
DP_TWIP_1250W	586	4.7	387
DP_TWIP_1800W	618	5.1	434
DP	880	15	490
TWIP	1050	40	420

Tab. 7 *Tensile properties for weld DP_TWIP_1250W and DP_TWIP_1800W: UTS: ultimate tensile strength, ε_{max}: elongation at fracture; σ_y: yield strength.*

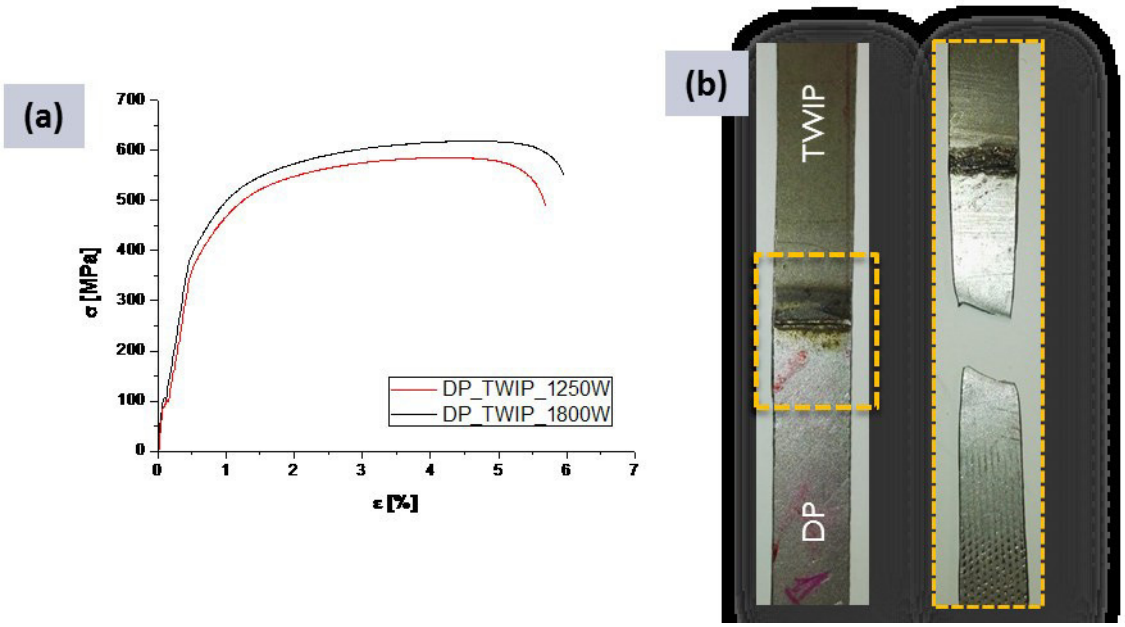

Fig. 56 *(a) Tensile test and (b) Photographs presenting the position of fracture in weld [174].*

Particularly, Tab. 7 reports the values of the yield stress (σ_y), ultimate tensile strength (UTS) and elongation ε_{max} for both samples.

4. CHAPTER: Fiber laser-MAG hybrid welding of DP/AISI 316 and TWIP/AISI 316 dissimilar weld

The aim of this chapter is to characterize DP/TWIP steels with austenitic stainless steel AISI 316, which will be used in laser-MAG hybrid welding. The steels employed in the present work are used in automobile industries, due to their excellent mechanical properties. However, the automotive industry is still reducing vehicle weight and, consequently, fuel consumption. Therefore, advanced high strength and stainless steel sheet can do the trick.

4.1. Experimental set-up

An innovative heat source has been used for fiber laser MAG welding to weld in butt configurations Dual Phase (DP) /AISI 316 and Twinning Induced Plasticity steels (TWIP)/AISI 316 plates 1.5 mm thick (Fig. 57). The heat source was an Ytterbium Laser (IPG YLS-4000) combined with a MAG generator. The MAG torch was tilted at an angle of 40°. The heat sources were distant 2 mm each other.

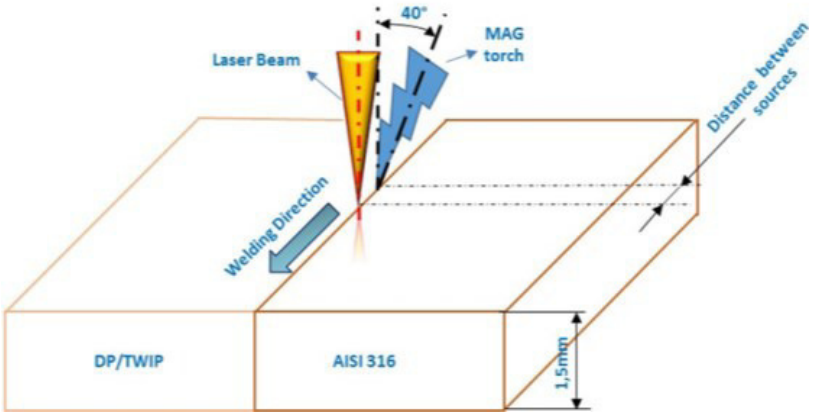

Fig. 57 *Schematic configuration of hybrid laser welding [178].*

Metal	C	Si	Mn	Cr	Mo	Al	Ti
TWIP	0.66	0.2	23.4	0.13	0.12	0.04	-
DP	0.09	0.21	1.65	0.43	-	0.03	0.003

Tab. 8 *Chemical composition of TWIP and DP steel (wt.%) [178].*

Metal	C	Cr	Mn	Mo	Ni	P	S	Si	Fe
AISI 316	0.08	18	2	3	14	0.045	0.03	1	balance

Tab. 9 *Chemical composition of AISI 316 (wt.%) [178].*

A laser leading configuration was used, so the laser beam is the main heat source. The filler material 316L-Si/SKR-Si (diameter 0.8mm) has been employed. For the composition of the filler wire see Tab. 6. In order to promote process stability, the shielding gas was a mixture of 87 % Argon and 13 % carbon dioxide. Tab. 8 and Tab. 9 show the chemical composition of TWIP, DP, and AISI 316 stainless steel. Particularly, the same levels of laser power, laser speed, current and voltage for the two welds were used, according to the experimental plan shown in Tab. 10.

Laser power (W)	Laser speed (m/min)	Wire feed speed (m/min)	Current (A)	Voltage (V)
1500	2.4	8.6	94	20.2

Tab. 10 *Experimental plane [178].*

The cross section was prepared with standard metallographic techniques and etching to show the microstructures of the weld. Optical microscopy (OM; Nikon Epiphot 200, Nikon, Tokyo, Japan) was executed on the cross section of the dissimilar welded. The cross section were prepared with standard metallographic grinding and polishing techniques and etching to reveal the microstructures with the following reagents: Glyceregia solution: 15 ml HCl, 15 ml glycerol, 5 ml HNO_3 for austenitic stainless steel and TWIP steel and LePera solution: 1% metabisulfite in distilled water and 4% picric acid in ethyl alcohol for DP steel. Joints were subjected to Vickers micro-hardness measurement (Affri Wiky 200JS2) with a load of 0.3 kg for 15s. Tensile and bending test of the joints were analyzed, in order to understand the weld strength and formability.

4.2. Weld appearance and microstructure

The macro graphics of the joints cross-sections after chemical etching are shows in Fig. 58. The observation with OM reveals the full penetration and the absence of porosity and crack.

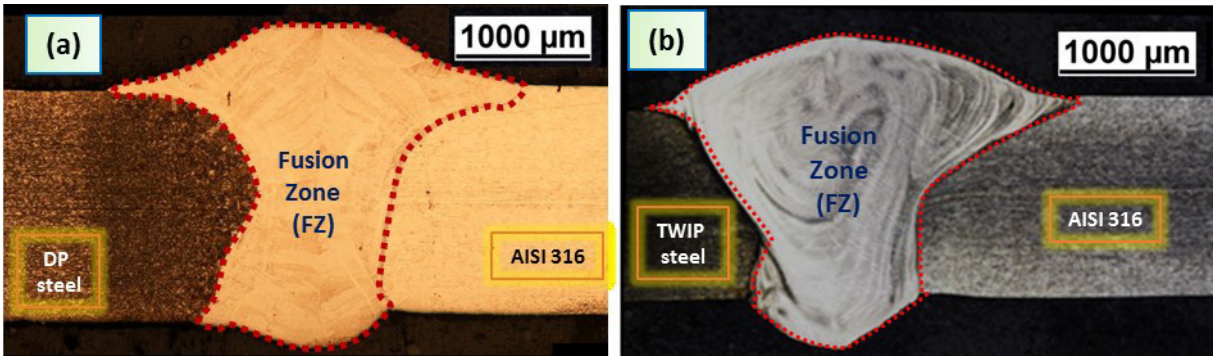

Fig. 58 *Macrographs showing joint cross-section of (a) DP/AISI 316 and (b) TWIP/AISI 316 [178].*

In the FZ of the DP/AISI (Fig. 59) a fine microstructure has been observed, due to the rapid cooling rate, mainly consists of martensite.

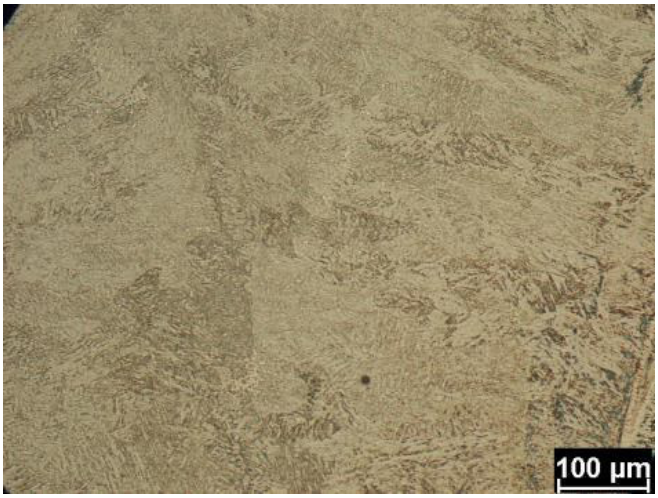

Fig. 59 *Optical micrograph shows microstructure FZ of DP/AIS [178].*

In the TWIP/AISI, the FZ exhibits a dendritic structure (Fig. 60). The dendritic grew toward the weld centerline in the direction opposite to the heat transfer direction [1, 179]. A small amount of shrinkage porosities was observed in the interdendritic regions, which means that the shrinkage cavities formed during the solidification process (Fig. 60).

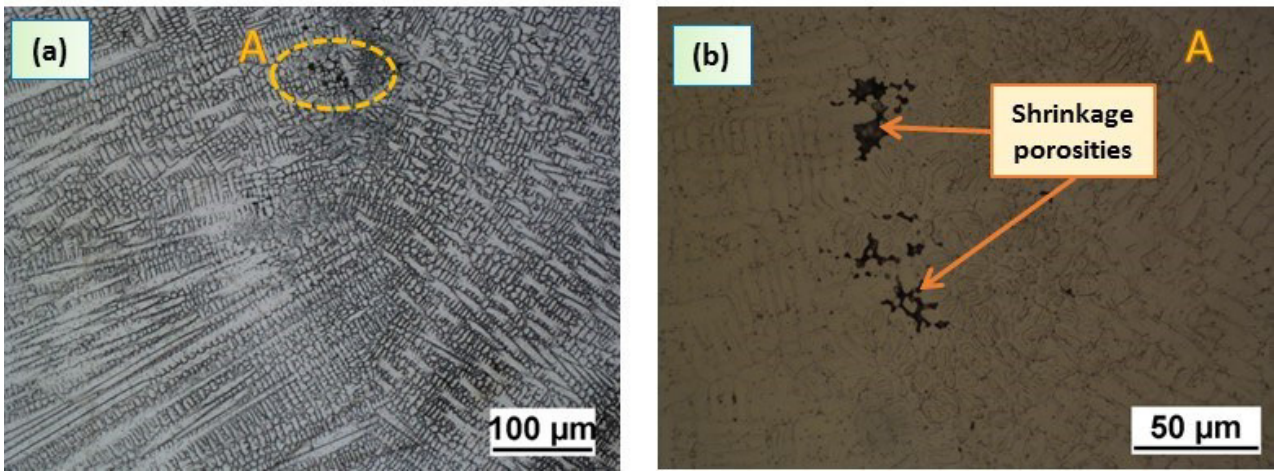

Fig. 60 *(a)Shrinkage cavities in the fusion zone of dissimilar joint TWIP/AISI 316; (b) Zoom-up of selected area at 500× [178].*

DP/AISI 316 showed a significant microstructural change in the heat affected zone (HAZ). That zone was created under the effect of thermal weld cycle. Different regions in HAZ can be observed after welding process as a function of the distance from the fusion zone (Fig. 61). In the Fig. 61 the microstructure inside the DP joint compared to BM microstructure is reported.

Consequently, HAZ can be divided into three sections, as follows: HAZ_1, adjacent to the FZ, where martensite is the main constituent due to at the rapid cooling (Fig. 61b). HAZ_2 is a region where the martensitic transformation is partial (Fig. 61c). HAZ_3 where the material was partially quenched to martensite and the original ferrite remained (Fig. 61d). The amount of martensite in the HAZ decreases with increased distance away from the fusion zone [180]. While as received material was characterized by martensite islands in the ferrite matrix.

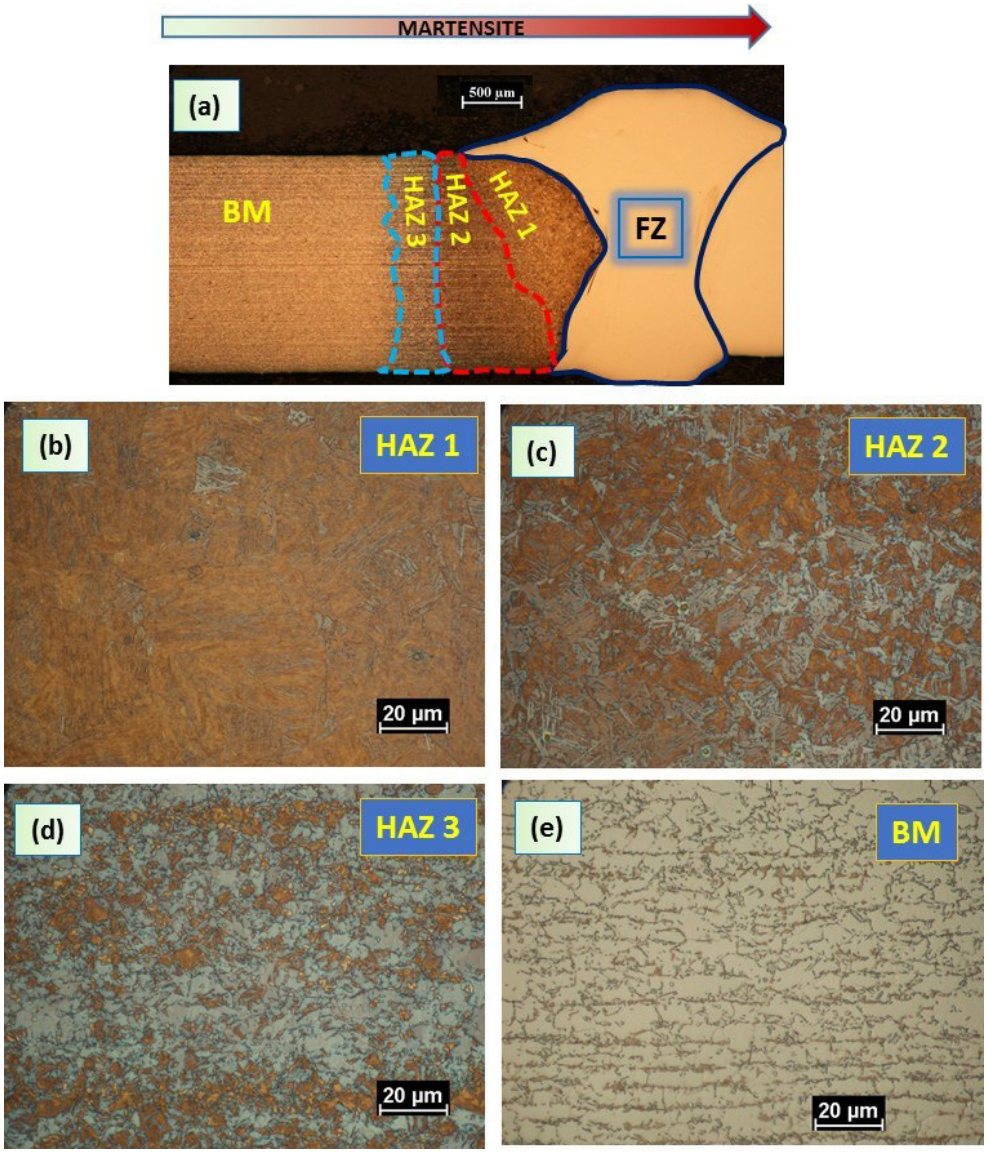

Fig. 61 *(a) Microstructure of the different zones in DP side: (b) HAZ 1, (c) HAZ 2, (d) HAZ 3 and (e) base material [178].*

In the BM of the TWIP steel (Fig. 62) a fine a fine austenitic microstructure has been observed. In the HAZ of TWIP side was observed the grain coarsening effect (Fig. 62). The grain coarsening effect was due to by low thermal conductivity of the TWIP steel. This causes heat accumulation, slower cooling, and coarsening in the TWIP side [175].

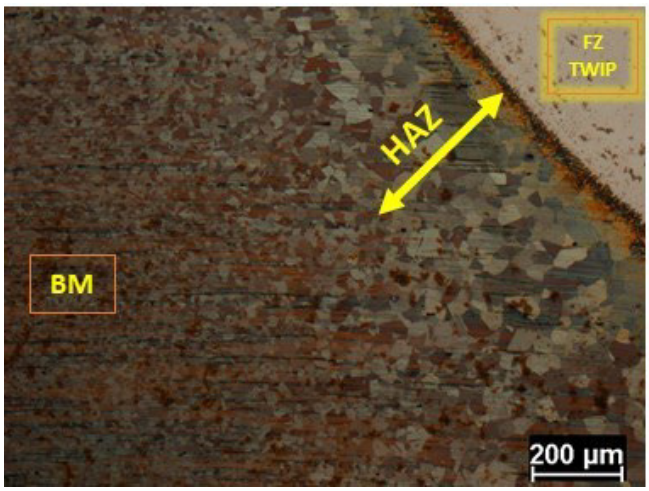

Fig. 62 *Optical micrography showing grain coarsening effect at HAZ of TWIP side and fine austenitic microstructure in the base material [178].*

The microstructure of the of the sample is shown in Fig. 63. In the AISI 316 HAZ side, delta ferrite stringers was detected as seen in the picture at high magnification (Fig. 63b). The migration of the ferrite stabilizers, such as Cr and Mn, from the filler metal to HAZ can promote the formation of delta ferrite, consequently, grain coarsening and refine the grain can be limited [165]. Moreover, the microstructure of BM was show in Fig. 63c. Austenitic grain has a polygonal shape with stringers of delta ferrite elongated in the rolling direction.

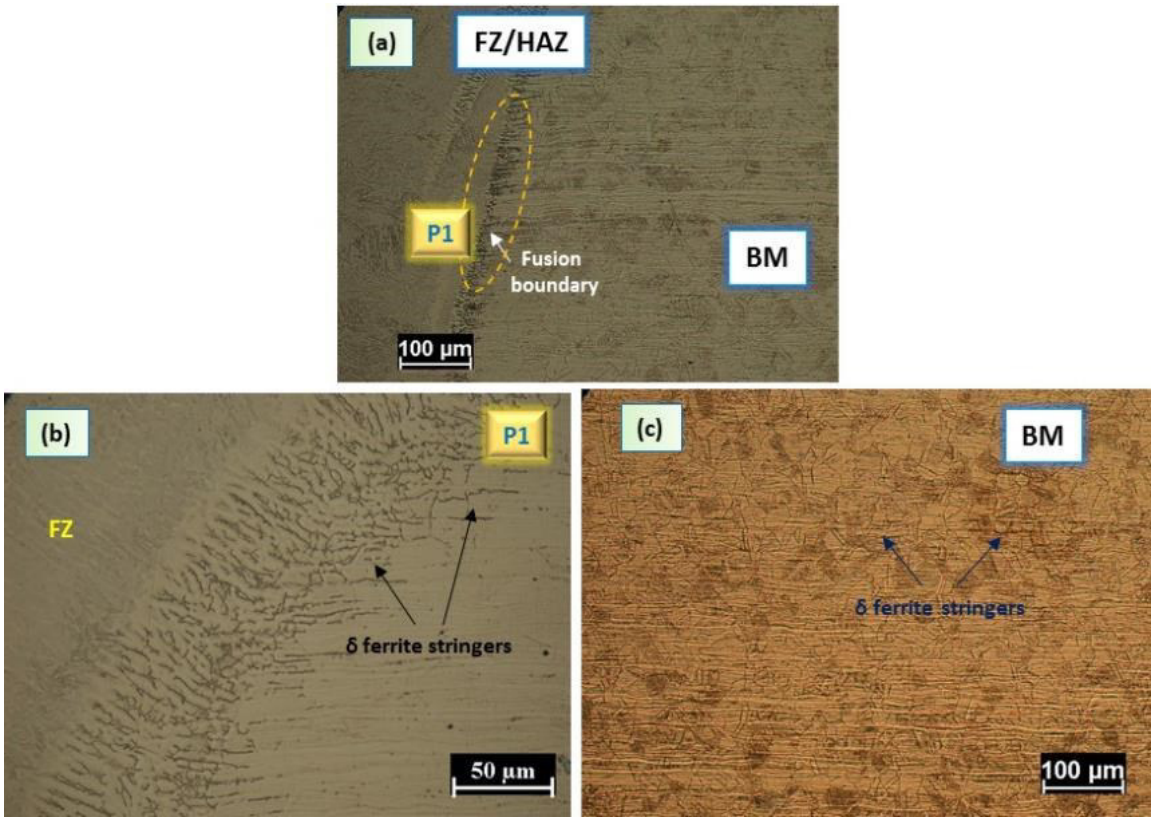

Fig. 63 *(a) OM of the interface FZ/HAZ; (b) Zoom-up of selected area at 500×; (c) Base material microstructure.*

4.3. Mechanical tests

4.3.1. Micro-hardness test

The micro-hardness in the transverse section of the welds were evaluated. Vickers micro-hardness profiles have been obtained in the cross section in the middle line. In Fig. 64 are reported the micro-hardness profiles of the weld. Significant variation in the FZ, HAZ, and BM micro hardness have been detected.

In HAZ close to DP side, the microhardness was significantly higher, which was over 300 HV. This is due to the formation of martensitic microstructure as a result of a fast cooling rate. In the fusion zone of DP/AISI 316 weld the hardness is lower than the HAZ of DP, this is probably due to the austenitic wire. In HAZ of DP steel, the hardness decreased under that of the base material due to a process named HAZ softening [176, 177]. In fact, martensite volume fraction of the base material regulates the degree of the HAZ softening. As showed in tensile and bending test, the degree of HAZ softening in the weld had a negligible effect on the overall mechanical behavior. Moreover, the hardness of DP base metal was as high as 216.6 ± 2.3 HV 0.3.

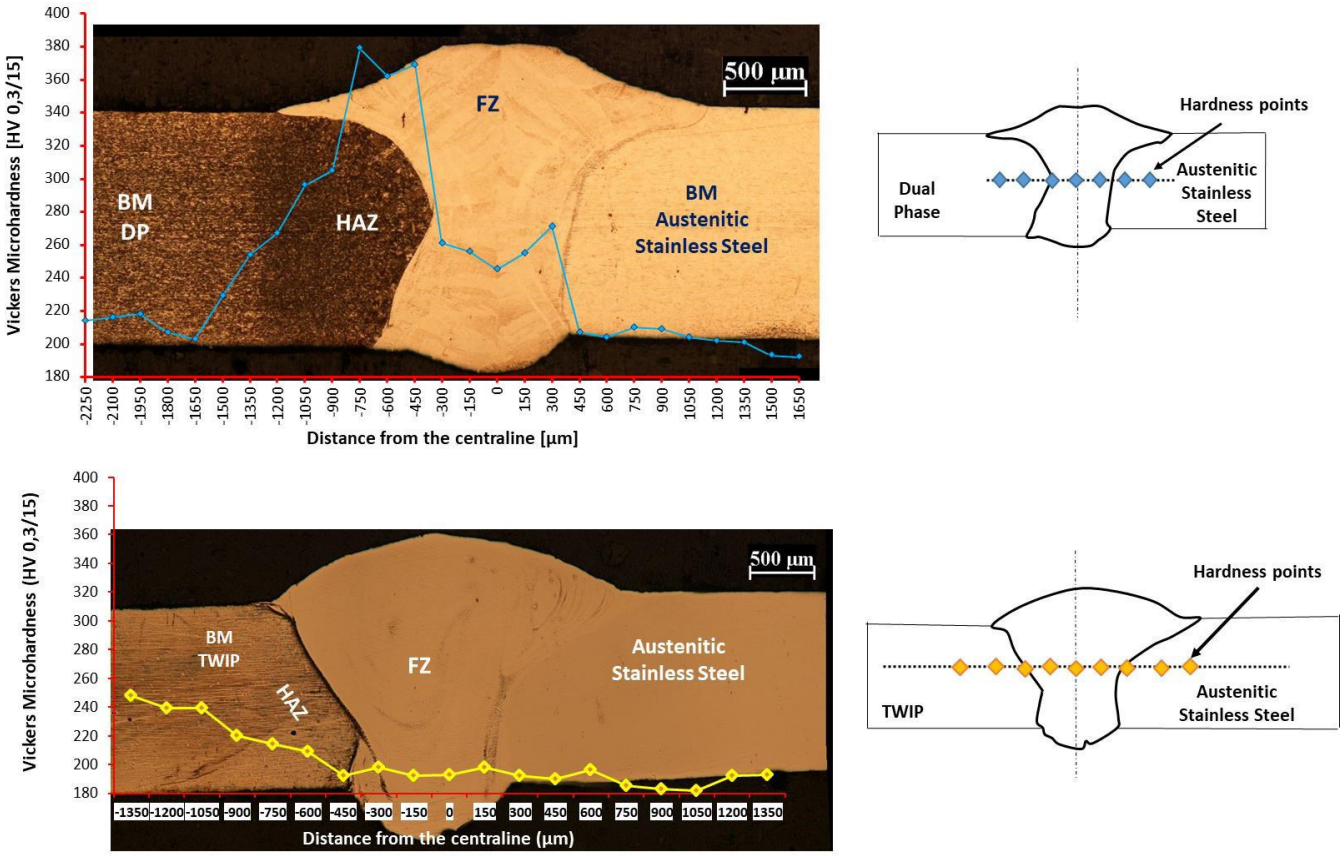

Fig. 64 *(a) Vickers Microhardness of the joint DP/AISI and (b) TWIP-AISI 316 Vickers Microhardness TWIP/AISI [178].*

In HAZ of TWIP steel, the microhardness was lower than that of the base material due to coarse austenitic grain. The fusion zone of dissimilar joint TWIP/AISI 316 shows low microhardness values, which was caused by the mixing of the austenitic wire and base material. The hardness of TWIP base metal was 246.5±4.3 HV0.3. However, both dissimilar joint exhibit the same trend in the microhardness in the austenitic stainless steel side. The hardness of the base material was as high as 179.5±4.3HV 0.3.

4.3.2. Tensile test

Tensile test has been performed and the specimens were taken perpendicular to the weld seam. The width was 10 mm. Tensile test was carried out to evaluate the weld strength. Fig. 65a reports the resulting tensile curve. The rupture occurred in the stainless steel form both type of weld, as it can see in Fig. 65b. The experimental error is the responsible for that difference

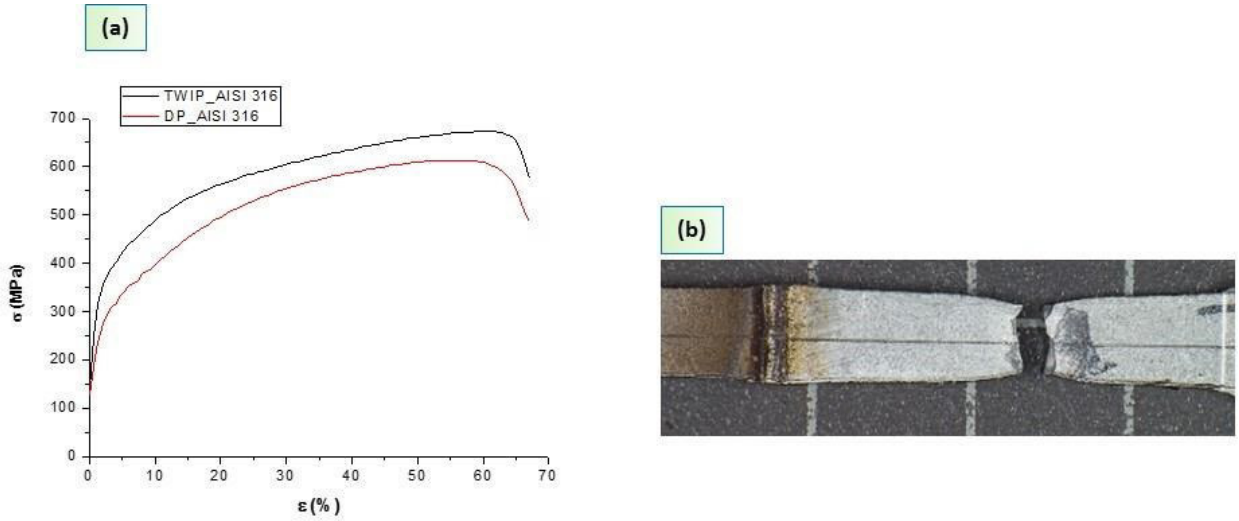

Fig. 65 *(a) Tensile curves of dissimilar welds and (b) Cracked specimen [178].*

In Tab. 11 are reported the properties of the samples, in terms of mechanical response. Difference in the welds strength and elongation was due to slight difference in the sample size and geometry, which can be considered as experimental error.

Sample	UTS [MPa]	ε_{max} [%]	σ_y [MPa]
DP/AISI 316	614	61	325
TWIP/AISI 316	672	51	350
DP	880	15	490
TWIP	1050	40	420
AISI 316	640	50	320

Tab. 11 *Tensile properties for dissimilar joints DP/AISI 316-TWIP/AISI 316. UTS: ultimate tensile strength, ε_{max}: elongation at fracture; σ_y: yield strength [178].*

4.3.3. Bending test

Three points bending test was performed to evaluate the weld quality. Both samples showed good behavior. The weld surface was defect-free after bending. Moreover, Fig. 66 shows the good bend behavior of samples after observation naked eye and optical microscopy (Fig. 67).

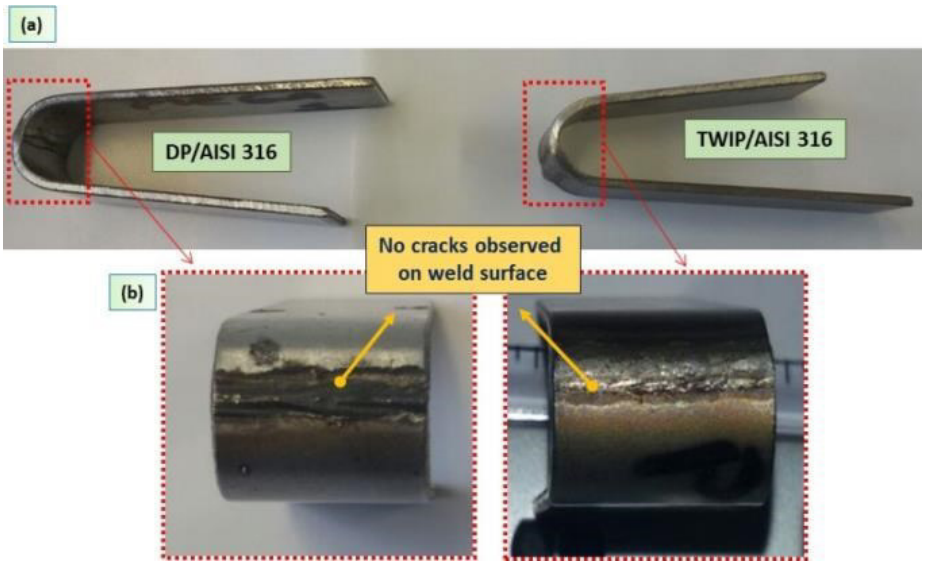

Fig. 66 *(a) Joint appearance after the bend test (b) Frontal views shows then absence of cracks on weld surface [178].*

The samples did not show defects on the weld surface after bending, even if they were subject to very high local deformations.

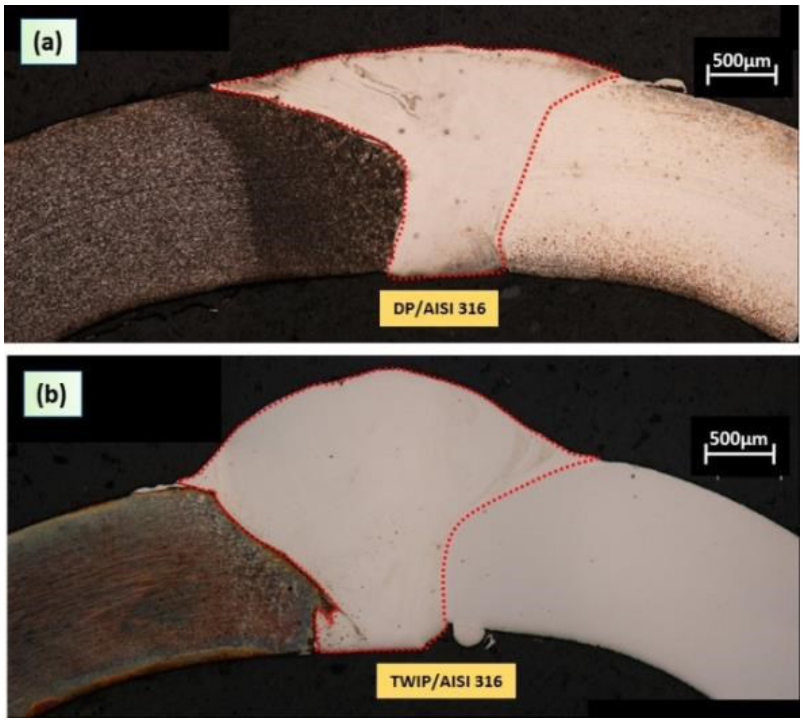

Fig. 67 *Cross section after bending: (a) DP/AISI and (b) TWIP/AISI [178].*

5. CHAPTER: Effects of Laser Offset and Hybrid Welding on Microstructure and IMC in Fe–Al Dissimilar Welding

In this chapter a comparative study between laser offset and hybrid laser welding of AA5754 and 316 stainless steel have been investigated. Realizing a fusion welded joint between Al and Fe alloys is challenging, due to the difference in thermal properties. Moreover, the nearly-zero solid state solubility of Al in Fe, and the zero solubility of Fe in Al result in the formation of brittle intermetallic compounds (IMCs), which deteriorate the mechanical properties [5, 66]. Consequently, the microstructure and interlayer were characterized by optical and electron microscopy to understand in detail the morphology of the weld. The phases and their distribution were determined by micro-hardness, which was associated with data available in the literature. The EDS/XRD analysis revealed the composition of the intermetallic compounds.

5.1. Material properties and weld configuration

The butt weld configuration was used for examination the weldability of a dissimilar Al–Fe weld. The dimensions of the plates (length x width x thickness) were 100x50x3 mm^3 for the aluminum sheet and 100x50x2 mm^3 for the steel one. The difference in sheets thickness was chosen to enhance the wettability of aluminum on the steel. Austenitic filler wire (AISI 316) with a diameter of 0.8 mm has been used. The chemical compositions of as-received alloys are displayed in Tab. 12.

METAL	C	Cr	Mn	Mo	Mg	Ni	Ti	P	S	Si	Fe	Al
AISI 316	0.08	18	2	3	-	14	-	0.045	0.03	1	balance	-
AA5754	-	0.30	0.50	-	3.6	-	0.15	-	-	0.40	0.40	balance

Tab. 12 *Chemical composition of as-received alloys (weight %) [155].*

The

Tab. ***13*** shows the property of the base materials AISI 316 and AA5754:

METAL	UTS (MPa)	YS (MPa)	E (GPa)	A (%)	HV	K (W/mK)	T_L (°C)	ρ (g/cm^3)	C ($J/g^{\circ}C$)
AISI 316	580	290	193	50	178	163	1400	8	0.5
AA5754	230	80	68	17	62	147	600	266	0.9

Tab. 13 *Properties of the as-received materials: ultimate tensile strength (UTS), yield stress (YS), Young module (E), elongation to fracture % (A%), Vickers micro-hardness (HV), thermal conductivity (K), Liquidus Temperature (T_L), density (ρ), specific heat capacity (c).*

5.2. Welding systems

Two different systems were used to execute the welds:

- A standard laser system was used for laser offset welding. It included a 6-axis robot, a stationary shielding box system and a workbench, equipped with clamps and supporting table. A YLS-4000 Yb-doped fiber laser with a wavelength of 1070 nm and a maximum power of 4 kW (IPG Laser GmbH, Barbuch, Germany) was used in continuous wave regime.
- For hybrid laser welding, a CO_2 laser (Rofin, Hamburg, Germany) whose maximal power was 3 kW was used operating in continuous wave mode. In order to obtain the arc stability, a laser beam coaxial argon shielding gas has been employed.

5.3. Process parameters

Preliminary tests were executed to find out the process parameters that permitted the weld configuration. Tab. 14 shows the process parameters used for the analysis. In order to obtain a comparison between the results reached by the two technologies, the total power assumed for the hybrid process was larger (3420W vs 2500W), since part of the energy was used to melt the wire.

TECHNOLOGIES	Laser Power (kW)	Welding Speed (m/min)	Wire Feed Speed (m/min)	Current (A)	Voltage (V)
Laser Offset Welding	2.5	2	-	-	-
Hybrid Laser-MIG Welding	3.42	2	1.2	80	24

Tab. 14 *Experimental plane [155].*

5.4. Metallographic Analysis and Mechanical Testing

Weld cross sections of samples were cold mounted and subsequently they were grinded and mechanically polished. The microstructure was analyzed by Epiphot 200 Optical Microscope (OM, Nikon, Tokyo, Japan) and EVO scanning electron microscope (SEM, Zeiss, Oberkochen, Germany), equipped with an energy-di energy-dispersive X-ray spectrometer (EDS, Bruker AXS Inc, Madison, Germany). The specimens were obtained by a standard metallographic technique, and etching with the following reagents to reveal the microstructures: Keller's solution (1 ml HF, 1.5 ml HCl, 2.5 ml HNO_3, and 95 ml H_2O) for aluminum microstructure and Vilella's solution (1 g picric acid, 5 ml HCl, 100 ml ethanol) for steel microstructure. However, Vickers micro-hardness tests with a load of 0.1 Kg (AffriWiky 200JS2) on the interface aluminum/steel has been performed. An X-ray diffraction (XRD) equipment was employed (Rigaku diffractometer with CuKα radiation (λ = 0.154 nm)). The X-ray diffraction data were collected at a scanning rate of 0.02°/s in 2θ ranging from 20° to 100° with count time 1.0 s in the fusion zone of both

the aluminum and steel sheet. In the thin intermetallic layer, the X-ray diffraction data were collected at a scanning rate of 0.02°/s in 2θ ranging from 20° to 55° with count time 6.0 s.

5.5. Base Material characterization

The examined alloy belongs to aluminum alloys 5xxx group, and it is based on Al–Mg system. However, this alloy is a "non-heat-treatable" alloys, in which the strength can be due to alloying elements or through various degrees of cold working or strain hardening. The name H111 designates that the alloy has strain-hardened to obtain the desired strength without additional thermal treatments [181]. For this study, it was supplied in annealed and recrystallized state.

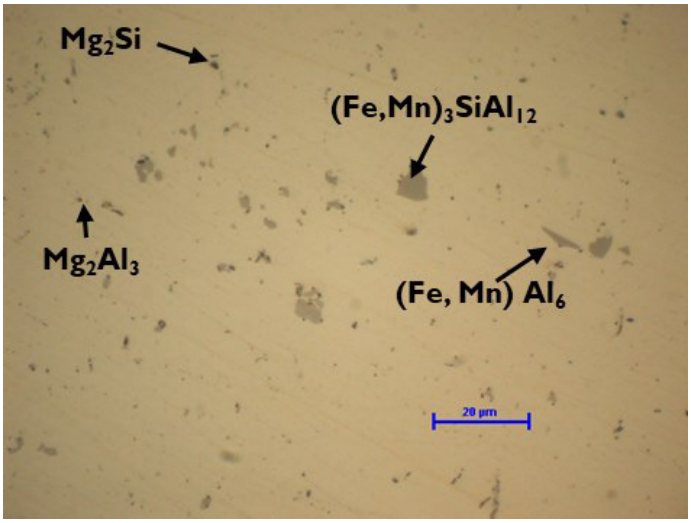

Fig. 68 *Optical micrograph of AA5754 base material [155].*

The annealing state is employed to give the material its plasticity bringing them back to the state before the plastic deformation, successfully make re-workable a material hardened by a previous cold working. The observation at the OM micrograph (Fig. 68) displays the aluminum matrix (solid solution phase) together with a series of intermetallic precipitates. It's know from the literature [181-183], that the acicular shape, light grey particles are $(Fe,Mn)Al_6$ (Fig. 68), while the rounded shape dark grey particles are fragile and this particles are identified as $(Fe,Mn)_3SiAl_{12}$ (Fig. 68). The larger black particles are identified as Mg_2Si (Fig. 68), while the smaller ones are Mg_2Al_3 [182,183].

Polarized light micrograph shows the microstructure of austenitic stainless steel 316L (Fig. 69). The samples exhibit an equiaxed, twinned microstructure. Austenitic stainless steel are characterized by annealing twins (induced by heat treatment) and deformation twins. Twins are typical of austenitic stainless steel and are characterized by low stacking fault energy (SFE). The low SFE austenitic steel promotes a planar arrangement of dislocations during the deformation inducing deformation twinning.

Consequently, the twin boundaries are obstacles to the dislocation slipping, which rises the strain-hardening rate [183].

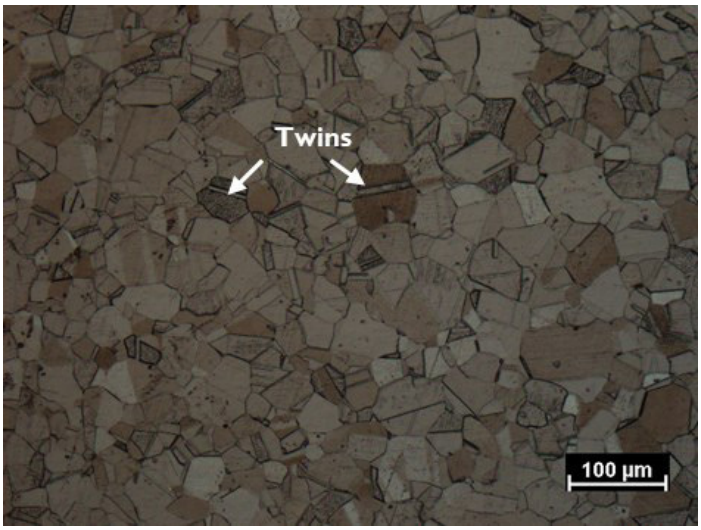

Fig. 69 *Polarized light micrograph of 316L base material [155].*

5.6. Laser off-set welding results

The cross section of the weld obtained by laser offset welding (LOW) is shown in Fig. 70. The joint exhibits full penetration and the undercut at the top surface was prevented. The bottom part of the weld showed a slight sagging. This geometric defect generally derived from the contraction of liquid walls during the solidification.

At the interface between aluminum and steel, a layer of intermetallic compounds (IMC) assuming curvilinear morphology (Fig. 71a). In the aluminum side, Fe-based isles are visible. These isles are not-uniformly distributed within the thickness. Consequently, a layer of intermetallic compounds is due to the low thermal input that promoted a slight interaction between liquid-state materials. Fig. 71b shows a magnification of zone A.

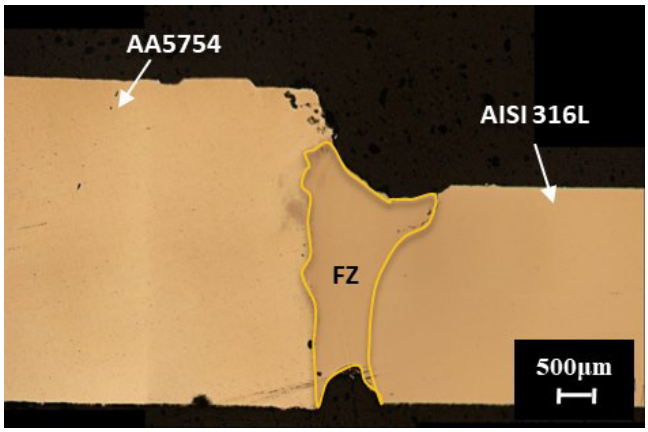

Fig. 70 *Optical macrograph of cross section obtained by LOW technique [155].*

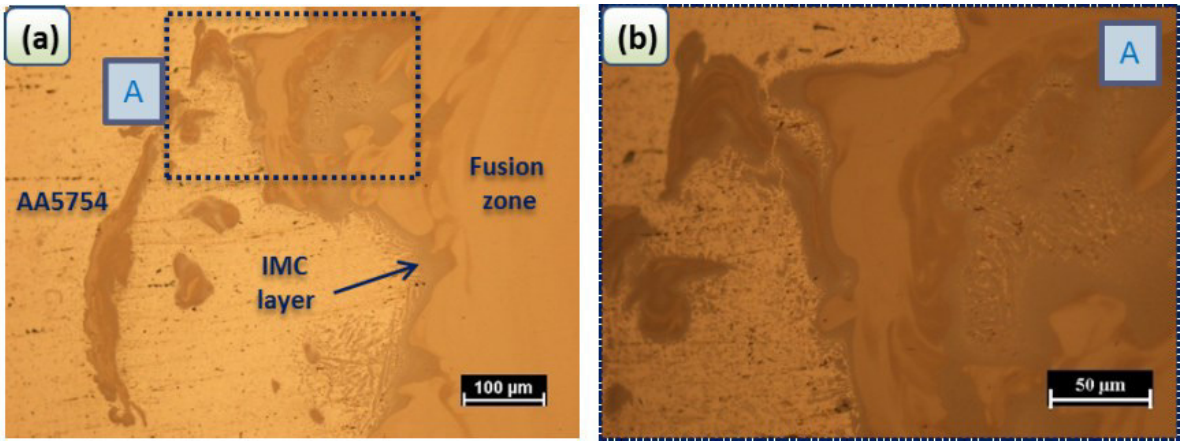

Fig. 71 *IMC layer of the joint at: (a) 200x; (b) high-magnification image of area A in (a) at 500x [155].*

Moreover, focusing the beam on the steel side limited the interaction between liquid phases into a narrow area. Thus, the growth of IMCs was limited and consequently laser offset welding considerably reduced the content of cracks and promoted a narrower intermetallic layer, which was limited to roughly 6 µm. (Fig. 72). While the aluminum side was not exposed to laser emission. So, neither vaporization of alloying elements and nor liquid viscous flows towards the interface was detected. Moreover, the rapid process speed lead to high cooling rate, promoting a narrower fusion zone [181]. Consequently, the shorter interaction time and narrower fusion area promoted a thinner IMCs layer. Such a result is extremely favorable for a larger sample strength [184].

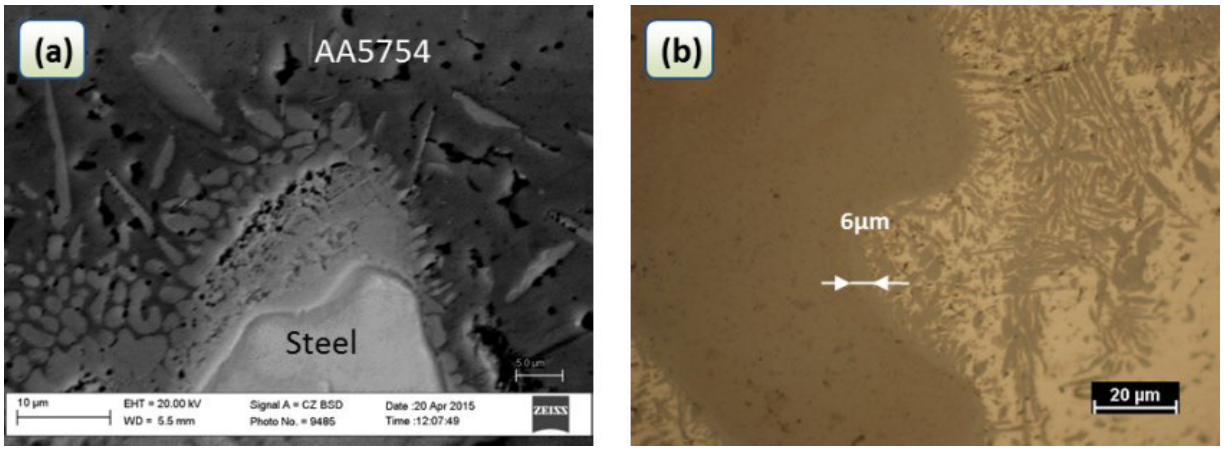

Fig. 72 *a) Optical and b) SEM micrographs showing IMC layer [155].*

The intermetallic layer was studied by means of back scattered (BS) electron, which unveiled different zones for chemical composition (Fig. 73 and Fig. 74). The maps of elements at the interface was showed in Fig. 73 b, c. The element distribution identified the presence both iron and aluminum mainly in the light gray areas while the fused zones contains respectively iron and aluminum together with their alloy elements. Principally diffusion of Al alloy elements towards the steel molten pool and vice versa can be detected too.

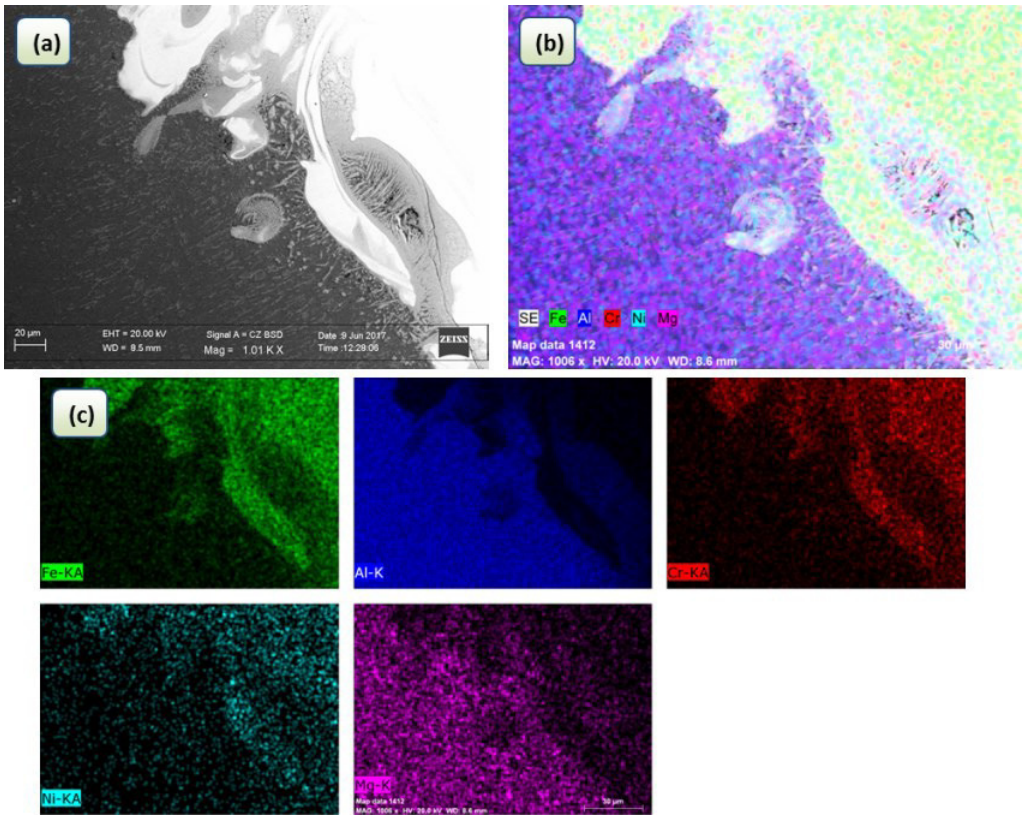

Fig. 73*(a) Back scattered electrons showing the IMC layer (b) alloy elements mapping and (c) maps of single elements at the joint interface [155].*

EDS analysis (Tab. 15) has allowed to identify the composition of IMCs in different zones. in the points (Fig. 72). In Fig. 74, those zones were marked with P1 (layer_1) and P2 (layer_2) respectively. The chemical analysis evidenced that in the zone P1 and P2, could be Fe_2Al_5 or $FeAl_2$ type according to Fe-Al phase diagram [140].

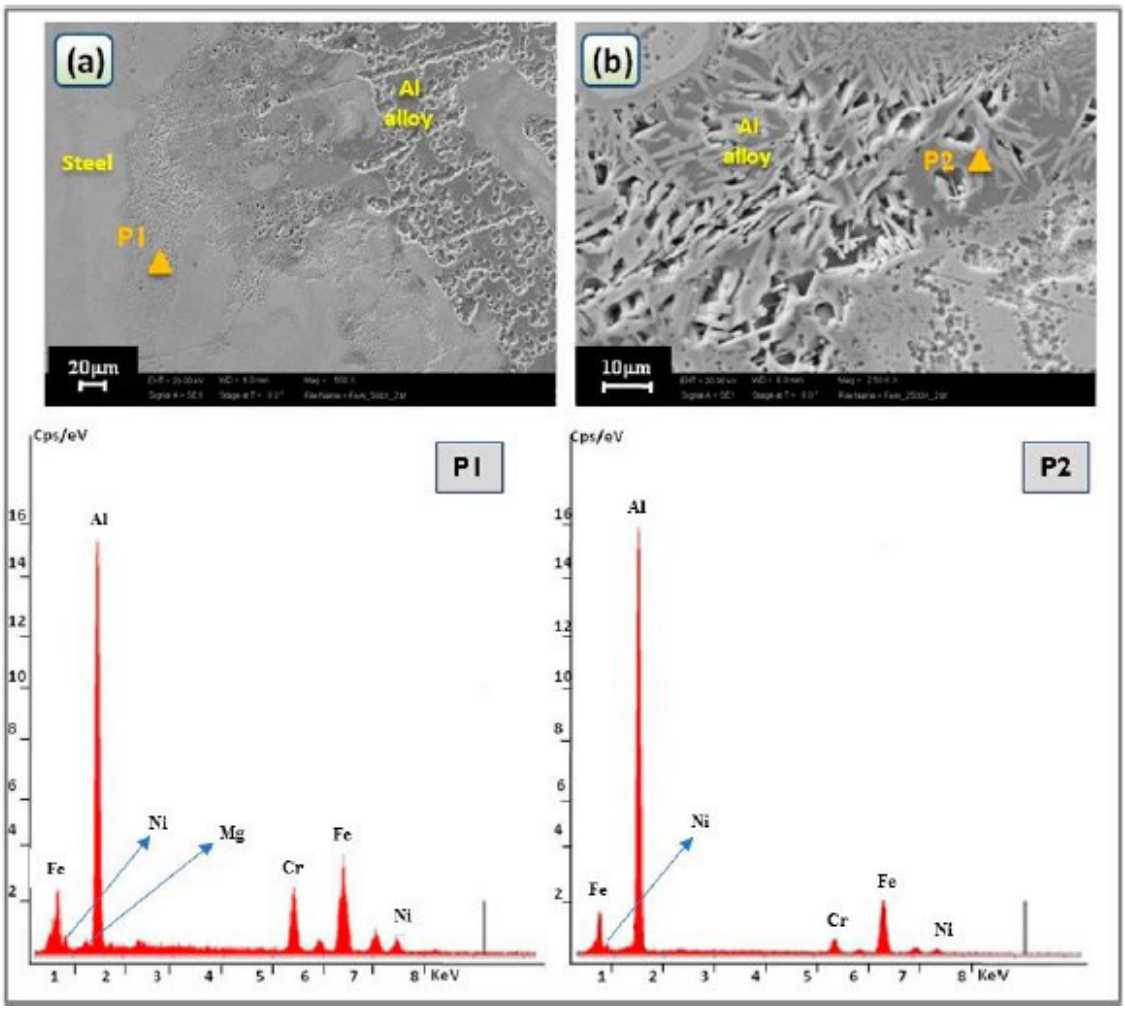

Fig. 74 *SEM micrographs of the IMC zone of the cross section with EDS analysis results in the highlighted points P1, P2 at (a) 5000_ and (b) 10,000_ magnifications [155].*

Point N°	Al	Fe	Cr	Ni	Mg
P1	63.9	26,2	5,8	3,3	0,8
P2	71.37	23,43	3,6	1,6	-

Tab. 15 *EDS analysis in IMC layer at different points near aluminum/fusion zone interface (at%) [155].*

As shown in the Fe–Al binary phase diagram [140], primarily five types of Fe–Al intermetallic compounds (i.e. Fe_3Al, FeAl, $FeAl_2$, Fe_2Al_5 and $FeAl_3$ phases) are obtained during the Fe/Al reaction process [185]. The sequence of the development of Fe–Al IMCs based on the thermodynamic data of the free energy designates that $\Delta G^0(Fe_2Al_5) < \Delta G^0 (FeAl_3) < \Delta G^0 (FeAl_2) < \Delta G^0 (FeAl) < 0 < \Delta G^0 (Fe_3Al)$

[185-188] suggesting that the first phase to be obtained is Fe_2Al_5. Moreover, to identify the different compounds in the interlayers, an X-ray diffraction (XRD) equipment was employed. Moreover, both the fusion zone of aluminum and steel were examined by XRD (Fig. 75b, c). In the steel fusion zone were identified the diffraction peaks of Aluminum and iron, meanwhile in the Al zone only aluminum peaks were identified.

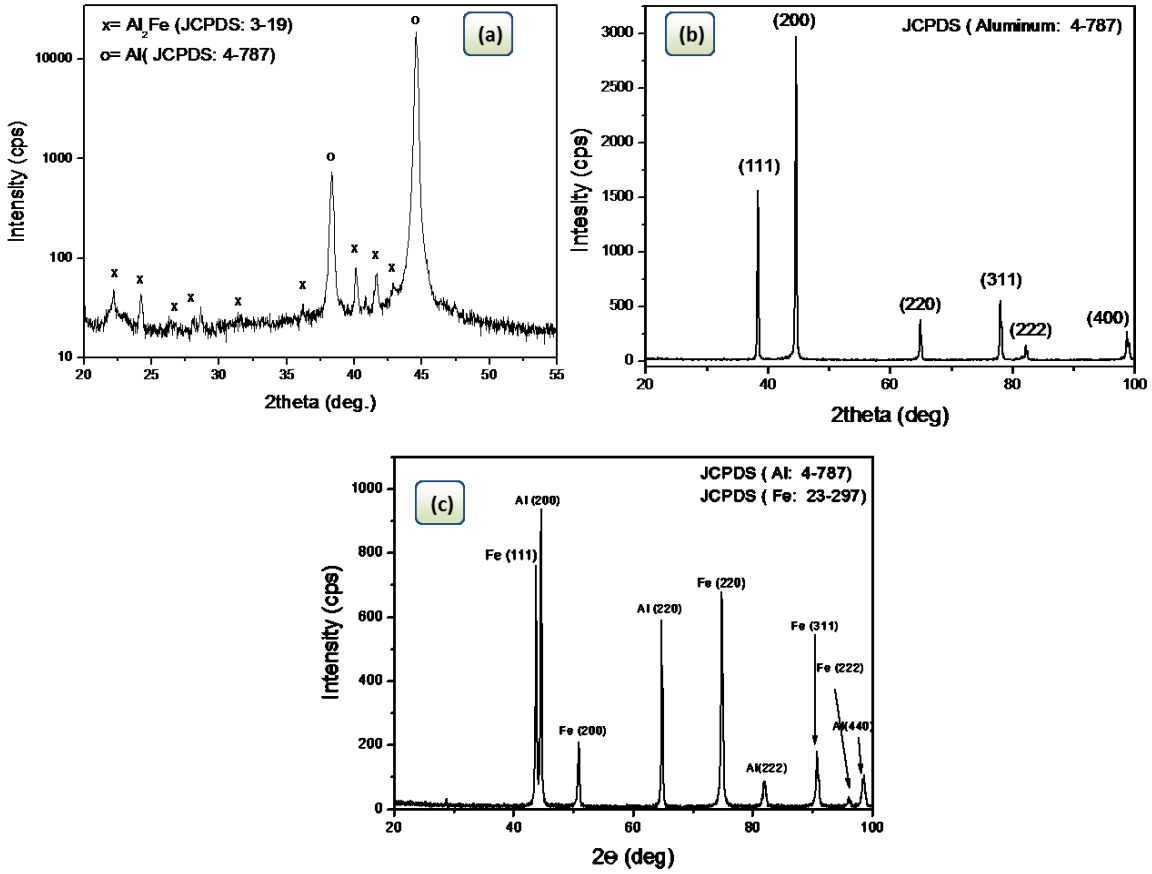

Fig. 75 *(a) precision X-ray diffraction analysis in the thinner intermetallic layer. X-ray diffraction analysis in the (b) aluminum and (c) steel fusion zone [155].*

The XRD analysis in the intermetallic zone identified only the $FeAl_2$ compound together with the Al matrix while no trace of some other more stable compounds was found. The reason could be the low amount of the more stable compounds (i.e Fe_2Al_5). In fact, during the welding technology the solidification is a non-equilibrium process being characterized by high welding speed (2m/min) and cooling rate. Consequently, the compounds formation could be not in agreement with thermodynamic condition. Therefore, if thermodynamically more stable compounds (such as Fe_2Al_5), being diffusion controlled, do not have sufficient time to growth during the cooling of the joint some other less stable compounds (such as $FeAl_2$) could nucleate and growth preferentially [1]. The micro-hardness test in accordance with typical values reported in the literatures, shows the presence of FeAl or Fe_2Al_5

intermetallic compounds (Fig. 76a) [189]. In such a case, the values of hardness could be underestimated due to the effect of Al matrix (Fig. 76b).

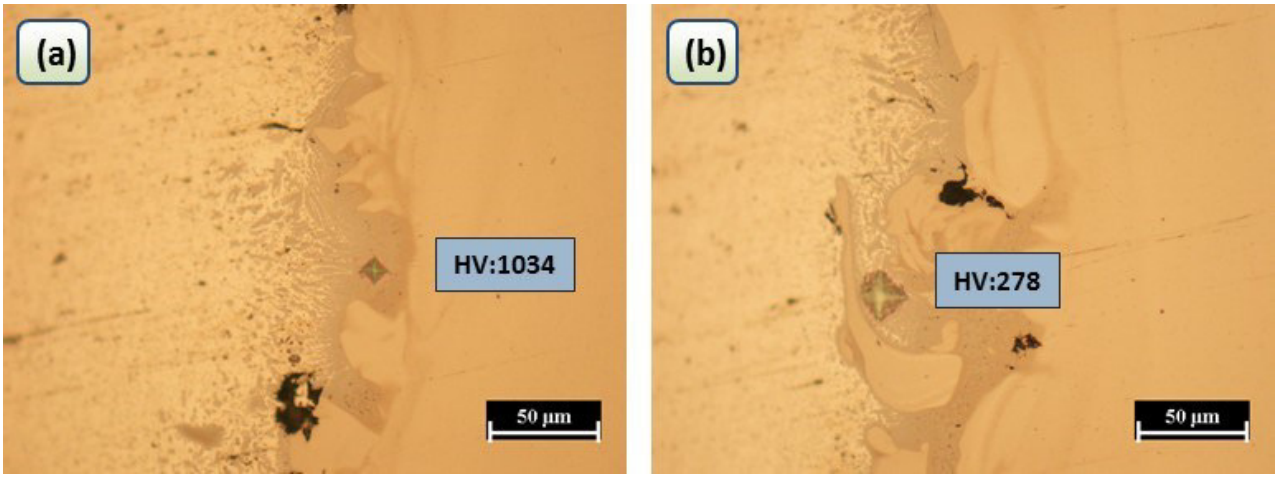

Fig. 76 *Optical micrographs of sample shows the result of Vickers micro-hardness measurements on the interface aluminum/steel: (a) hardness value due to IMC (b) hardness value due to both effect of IMC and Al matrix [155].*

The micro-hardness in the transverse section of the weld was evaluated (Fig. 77). The hardness of the Al FZ was higher than that in the heat affected zone (HAZ) and the base material (BM). Moreover, rapid solidification and consequently both grain refining and low grain boundaries precipitation increased the hardness in the FZ. It is observed in Fig. 77 that the hardness of the Al HAZ is slightly larger than that in the base material. This result can be probably induced by the dissolution of soluble compounds and the consequent strengthening by solid solution.

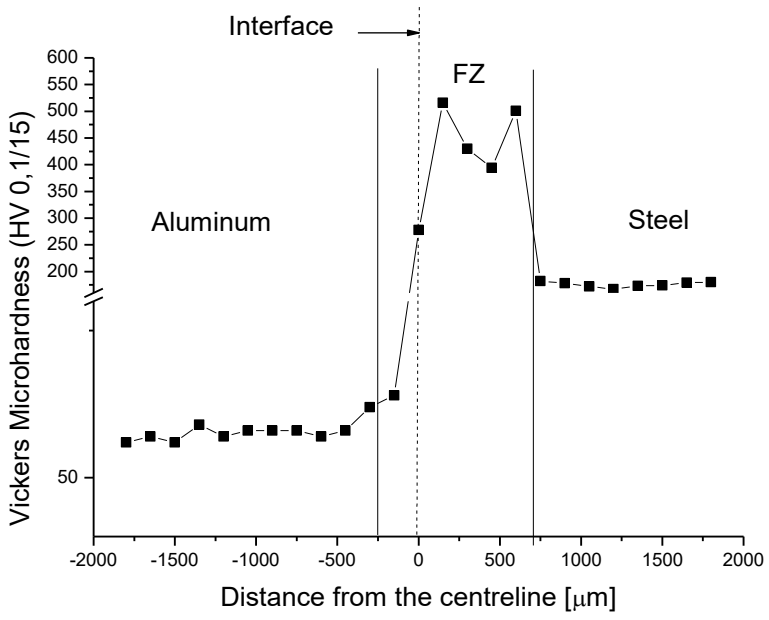

Fig. 77 *Vickers micro-hardness profile for the laser offset welding [155].*

The increase of hardness in the steel is due to grain refinement promoted by laser welding process [190, 191]. Grain boundary precipitation on the aluminum side did not occur during the joint solidification because the rapid cooling. If grain boundary solidification occurred, the hardness of AA5754 would strongly decrease. The precipitation of Al–Mg particles inside the grains leads to softening [1, 192].

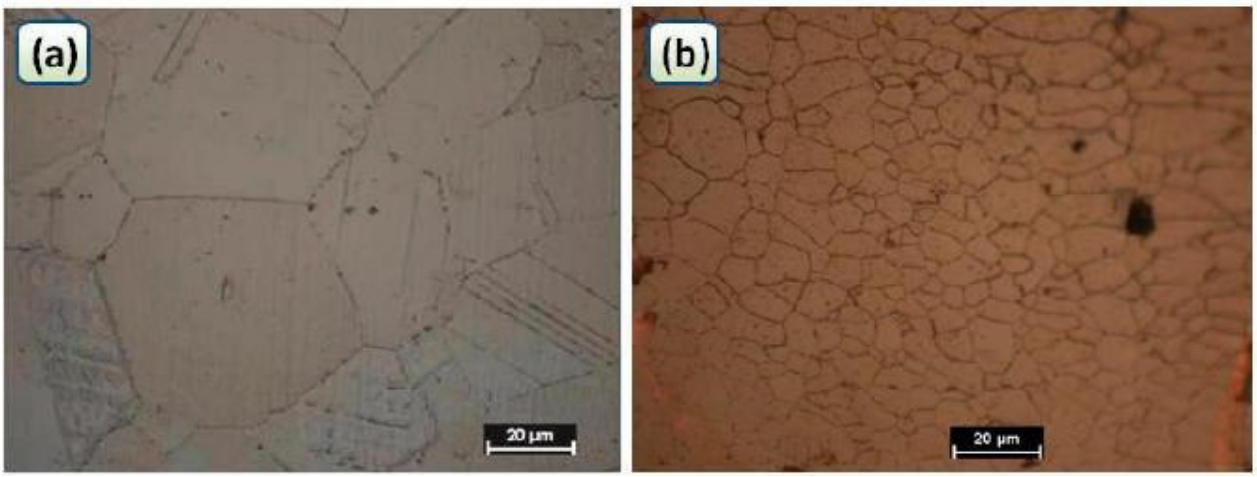

Fig. 78 *Optical micrographs showing (a) base material of 316L stainless steel and (b) fine structure in the fusion zone due to the fast solidification [155].*

5.7. Laser hybrid welding results

Cross section of the joint obtained by hybrid laser-MIG welding has been observed (Fig. 79). The top surface presented excessive weld metal, while the bottom part exhibited a slight lack of penetration.

These geometric defects can be explained by assessing the process dynamics. Consequently, lower wire feeding speeds were assumed to improve the geometric outcome and reduce the defectiveness. Nevertheless, reducing the deposition rate of filler wire must correspond to a reduction of the heat input to keep the process energy balance and avoid wire overheating. However, the laser power was maintained constant, because it is mainly responsible for penetration. Nevertheless, even if the laser power was maintained constant, the low MIG power had a negative effect on the geometry of the sample.

The negative effect on the geometry of the joint is due to the amount of total energy was not adequate to fully penetrate the sheets' thickness and produce a consistent bond. Thus, the most satisfactory outcome was evaluated for the present analysis (see Tab. 14). Fig. 79 shows, a good compromise between penetration and excessive weld metal. A slight lack of weld penetration was detected at the bottom part (less than 0.3 mm depth), while the excessive weld metal was limited to 0.6 mm.

The interface between the two metals was highly irregular and non-homogeneous (Fig. 80). Because of the difference in thermal expansion coefficient between the two metals and the brittleness of IMCs structures, cracks formed at the interface. Consequently, a huge amount of thermal energy was directly adduced at the interface between the sheets.

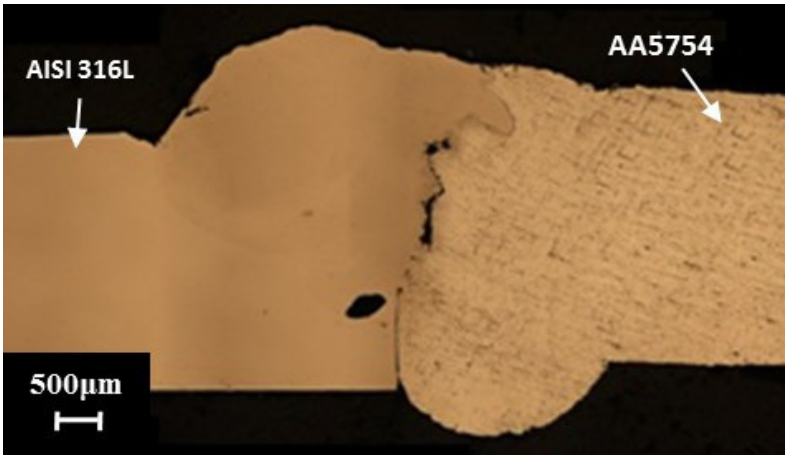

Fig. 79 *Cross section by hybrid laser-MIG welding [155].*

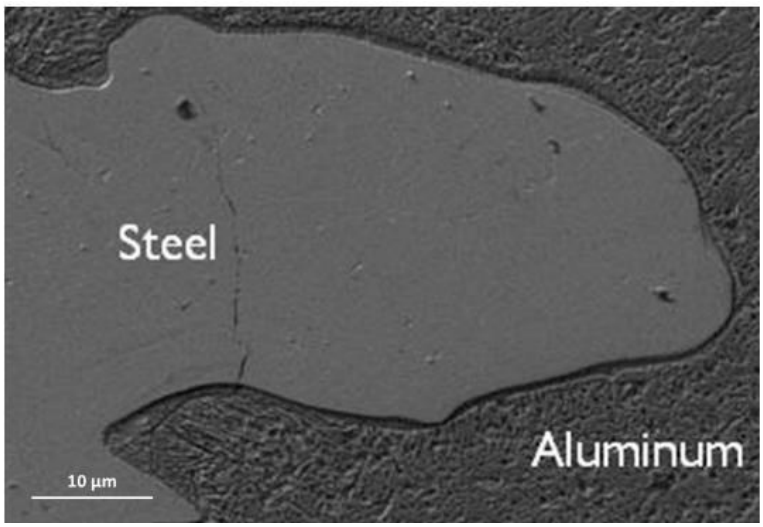

Fig. 80 *SEM micrograph showing irregular interface between the two metals [155].*

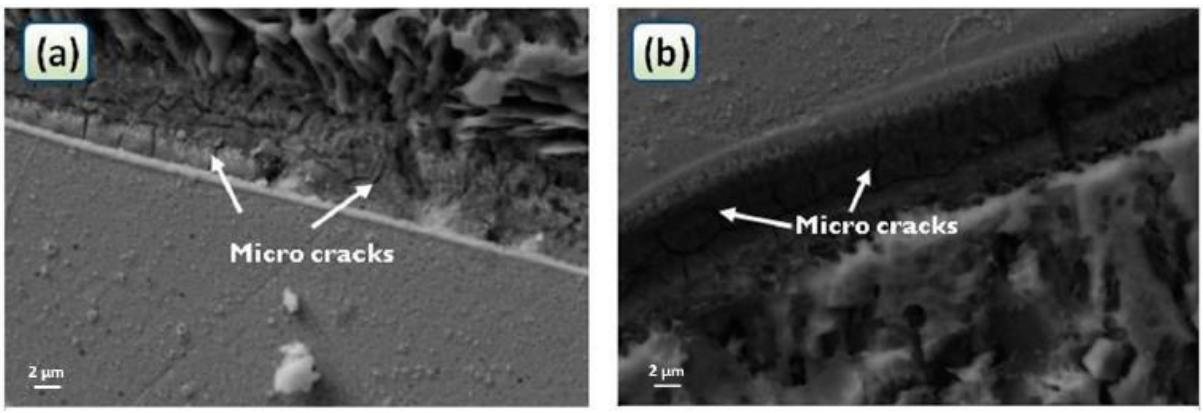

Fig. 81 *SEM pictures show: (a) Close-up of the upper side of the interface of the sample; (b) Close-up of the lower side of the interface of the sample [155].*

The geometry of the IMCs layer was analyzed by scanning electron microscope. The width of the IMCs layer exceeded the value of 14μm (Fig. 81).

The arc favored lower cooling rate and non-uniform energy distribution within the thickness and consequently a longer reaction time for IMCs growth occurred. Micro cracks were identified at both the upper and lower side of the interface (Fig. 81). IMCs compounds at the interface are extremely brittle. During welding process, local stresses exceed the elastic limit, leading to small fractures both perpendicular and parallel to the layer width.

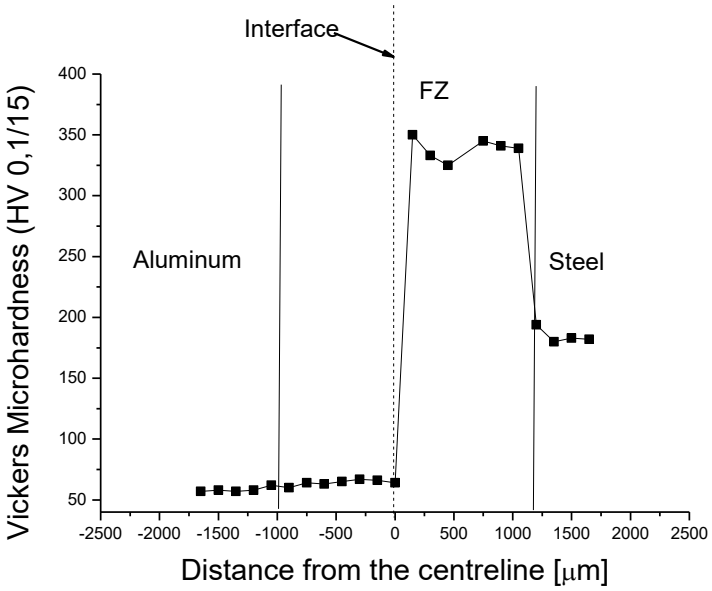

Fig. 82 *Cross weld section microhardness profile for the hybrid laser-MIG [155].*

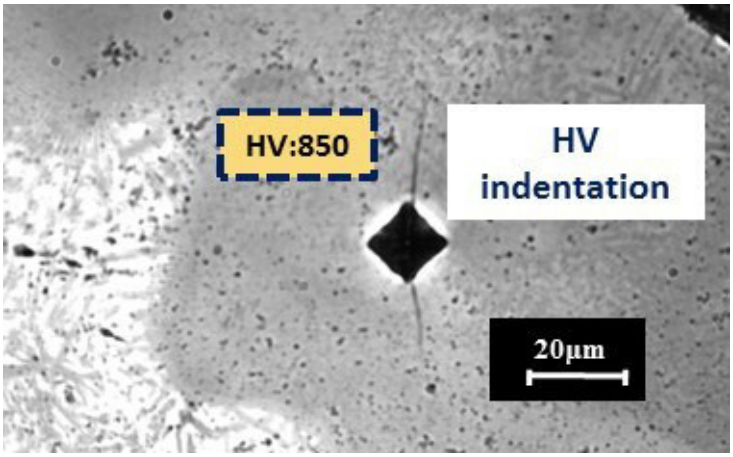

Fig. 83 *Micro-hardness indentation of the intermetallic layer [155].*

In Fig. 82 are reported the micro-hardness profiles of the weld. Adding arc increased the thermal energy and volume of molten metal compared to single laser welding. Therefore, even if the welding speed was the same as for the autogenous laser process, the thermal inertia of the fusion zone was higher and the cooling rate was lower, leading to grain coarsening effect and lower hardness values in the fusion zone.

Fig. 83 shows the indentation was performed at the aluminum/steel interface with a value of 850 Vickers. The IMC layer presented much harder than single-alloy fusion zones. Consequently, the intermetallic layer is locally subjected to compressive and tensile stresses during the non-uniform solidification, which probably permits crack propagation.

6. CHAPTER: Thermo-mechanical simulation of fiber laser-arc welding of DP/AISI 316 and TWIP/AISI 316 dissimilar joints

The most important aspect to simulate laser welding is the heat source model. For a dissimilar laser weld, the model of the heat source is a paramount boundary condition for the prediction of the thermal phenomena, which occurs during the welding cycle. In this chapter, three-dimensional (3D) Gaussian heat sources for simulating the keyhole in laser welding and Goldak's double-ellipsoid heat source model was assumed to describe the arc power. These thermal sources were studied for the thermal and mechanical analysis of the fiber laser welding of DP/TWIP with AISI 316 dissimilar butt joints. Analysis is performed with numeric code, Simufact welding. The models were calibrated comparing the fusion zones of experimental and numeric results and were validated by the continuous cooling transformation (CCT) diagram.

6.1. Experimental set-up

A laser arc hybrid welding butt joint has been produced from plates of DP/TWIP with AISI 316, according to the scheme of Fig. 84. The welding parameters included 1500 W power at 2.4 m/min welding speed. Austenitic filler wire with a diameter of 0.8 mm was used (316L-Si/SKR-Si). The heat sources were 2 mm spaced. The laser focus was put at the sheets surface.

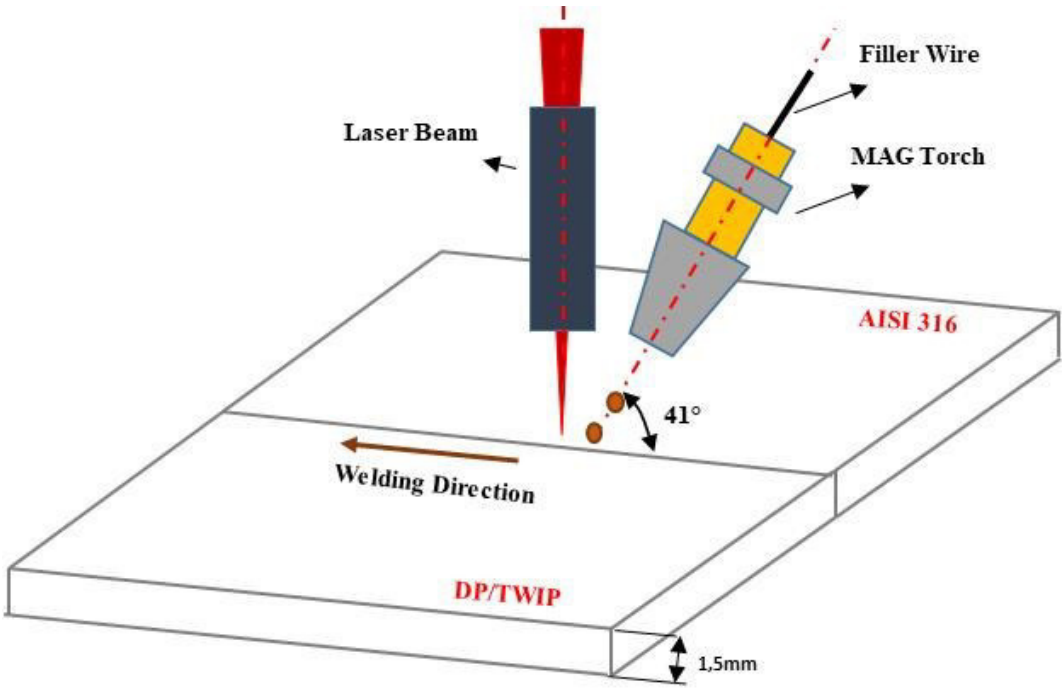

Fig. 84 *Scheme of hybrid laser welding on DP/TWIP with AISI 316.*

6.2. Numerical model

The finite element analysis was built using the Simufact Welding 8.0 software. Thermo-mechanical finite element calculation was executed for the prediction of the fusion zone and prediction of the temperature fields, thermal cycles and distortions of the plates. The flow chart in Fig. 85 defines the numerical procedure used in the finite element model: the coupling thermal analysis was used as input for mechanical analysis step by step.

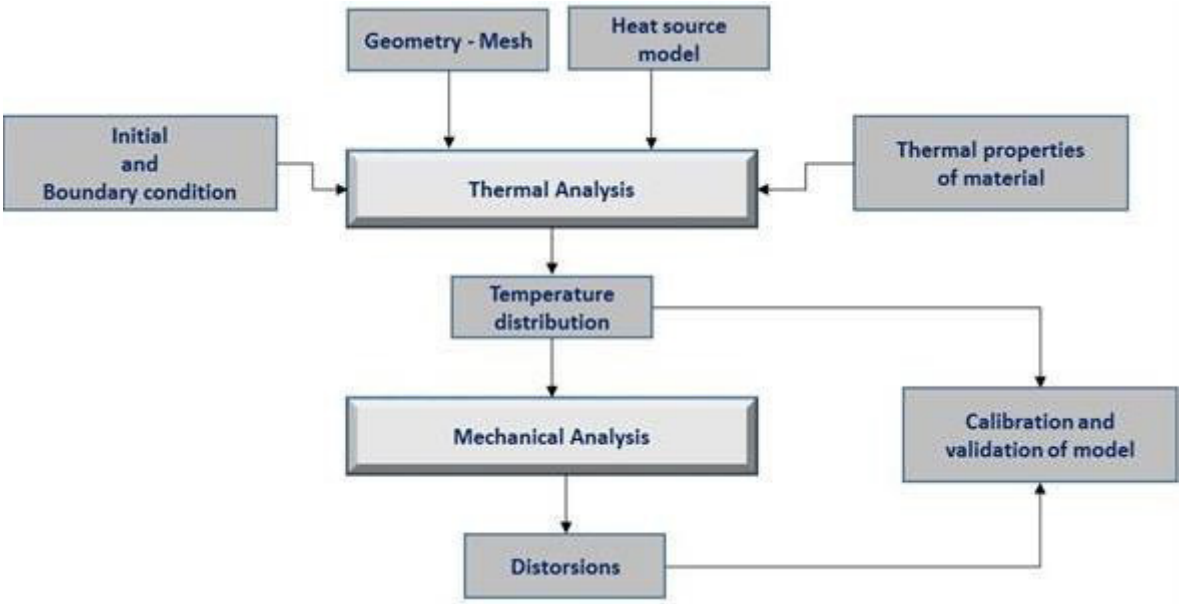

Fig. 85 *Flowchart of the simulation process.*

6.2.1. Geometry and mesh

For simulate the models, the real setup has been considered. Particularly, two plates of DP/TWIP with AISI 316 (150x50x1.5mm) were welded along the long side. The accuracy of the temperature distribution in the zones with high thermal gradient is directly related to the finite element mesh that is used. Fig. 86a displays the mesh used in the model.

Mesh sizes is equal to 3.2×0.5×0.1 mm^3 at the contact surfaces of the plates in order to reproduce the high thermal gradient. The ratio in size between the last element and first element in the distribution is 0.1 (Fig. 86b). A coarse mesh was employed far from the molten pool to reduce the computational cost. The mapped mesh had 33000 elements.

The top and bottom reinforcements produced during the welding processes require a finer mesh. The tetrahedron mesh in the top and bottom material had 45000 elements (see Fig. 86b).

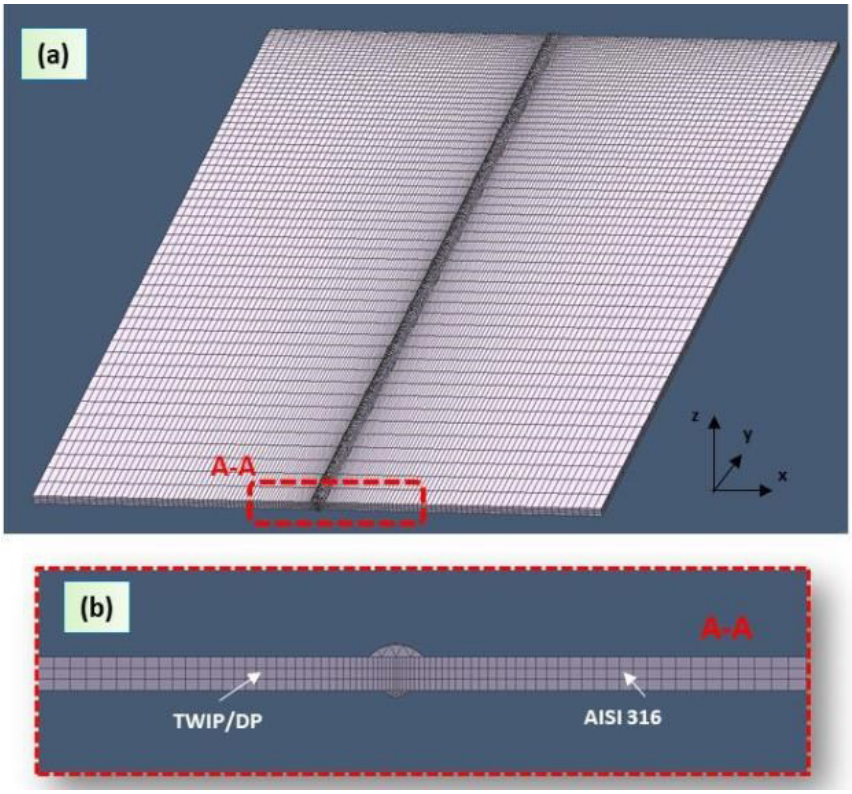

Fig. 86*(a) FEM model used in the hybrid laser-arc welding; (b) Detail view of mesh.*

6.3. The welding procedures

The welds were obtained using two different technologies: the laser offset welding (LOW) and the hybrid laser-MIG welding. In the LOW, the laser source was focused on the steel side at a distance from the aluminum edge (off-set) (Fig. 87). In this study, the off-set value was about 1 mm from the laser beam axis. The heat moved to the aluminum side through the steel heat affected zone, as describe in Fig. 88. So, the thermal energy spreading from the keyhole produced the fusion of the aluminum. In this way, the steel fusion zone (FZ) divided the steel molten pool from the aluminum-fused zone, which avoided the excessive growth of the IMC layer.

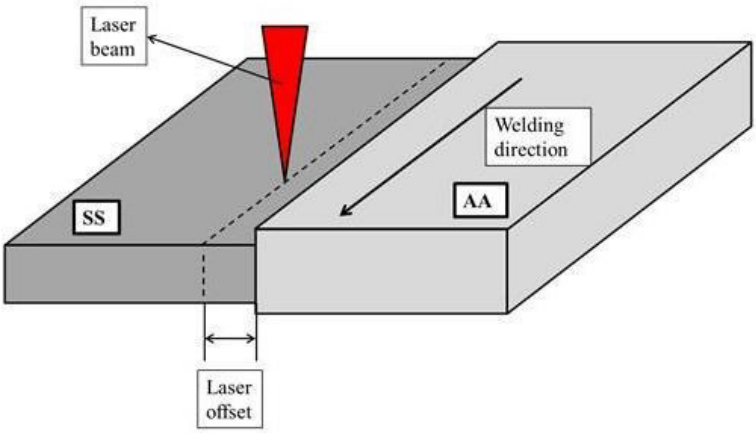

Fig. 87 *Laser offset welding configuration (LOW) [155].*

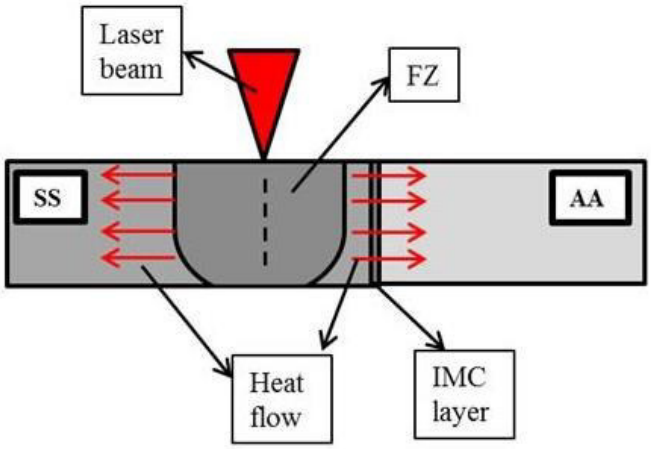

Fig. 88 *Schematic drawing for describing the joining mechanism by LOW technique [155].*

On the other hand, during laser-MIG hybrid welding the laser-arc coupled source was focused perpendicularly to the weld surface. However, the wire was located at a 1 mm distance from the laser focus (see Fig. 89).

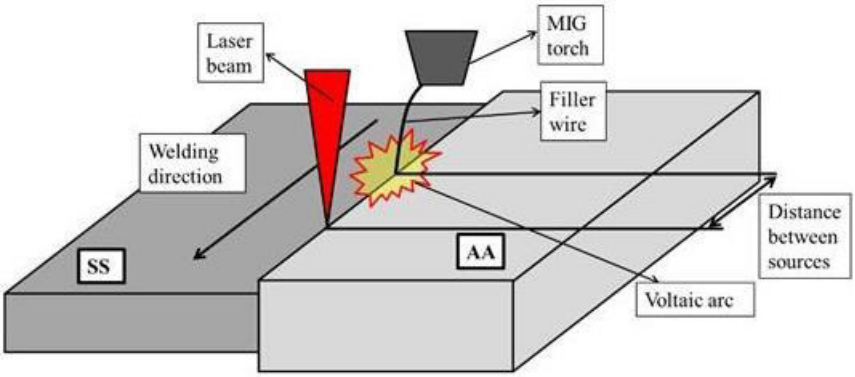

Fig. 89 *Sketch of laser MIG welding [155].*

6.3.1. Material property

Tab. 16 displays the mechanical and thermo-physical properties at room temperature of DP, TWIP and AISI 316 stainless steel. Temperature dependent material properties were considered in the finite element analysis. The simulation strategy was to execute first the thermal analysis. The thermal load data was used for the mechanical analysis to evaluate the induced strain fields.

Property	DP Steel	TWIP Steel	AISI 316
Young modulus [GPa]	137.5	171.5	205
Density [Kg/cm^3]	7326	7500	7800
Thermal Conductivity [W/mK]	35.3	40	16.3
Liquidus Temperature [K]	1788	1696	1673
Solidus Temperature [K]	1650	1562	1648

Tab. 16 *Mechanical and thermo-physical properties at room temperature of DP, TWIP and AISI 316 steels.*

6.3.2. Initial and boundary conditions

The heat transfer in the plates can be obtained by solving the following heat equation [193]:

$$\frac{\partial}{\partial x}\left(K_x \frac{\partial T}{\partial x}\right)+\frac{\partial}{\partial y}\left(K_y \frac{\partial T}{\partial y}\right)+\frac{\partial}{\partial z}\left(K_z \frac{\partial T}{\partial z}\right)+Q(x,y,z)=\rho c \frac{\partial T}{\partial t} \quad \text{Eq. 13}$$

In this equation, Q (Wm^{-3}) represents the heat transfer in the work piece and ρ (kgm^{-3}) the density of the metal. K_x, k_y and k_z define the thermal conductivity in the x, y and z directions ($Wm^{-1}K^{-1}$), C represents the specific heat capacity ($J\ kg^{-1}\ ^{\circ}C^{-1}$), while t is the time (s),

Moreover, the surfaces include heat losses due to the convection and radiation. The heat losses following the equation [193]:

$$-q = \varepsilon\sigma(T_r^4 - T^4) + h(T_r - T) \quad \text{Eq. 14}$$

where ε is the emissivity of the surface, σ is the Stefan–Boltzmann constant, T_r is the room temperature (293 K), h is the heat transfer coefficient and can be assumed to 20 $W/(m^2K)$ for air and 200 $W/(m^2K)$ for the lower surface in contact with the workspace. The workpiece room temperature of 293K has been considered.

6.3.3. 3D heat source model for laser

In order to define arc and laser heat source in hybrid laser-arc simulation welding, two different heat source models were defined and coupled. 3D heat source was considered for both sources.

In particular, a conical heat source with a Gaussian distribution was defined for the laser welding simulation (Fig. 90). In this model, the heat intensity decreased from the top to the bottom of the heat source.

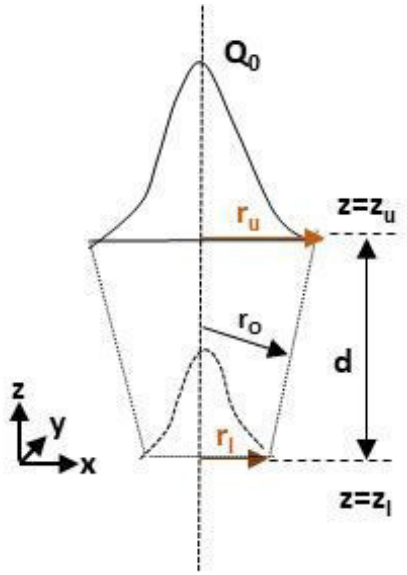

Fig. 90 *Conical heat source.*

The power distribution in welding direction can be expressed as it follows [194]:

$$Q_r = Q_o \exp(\frac{-r^2}{r_o^2}) \quad \text{Eq. 15}$$

$$r = \sqrt{x^2 + y^2} \quad \text{Eq. 16}$$

In particularly, Q_r symbolizes the heat source intensity, Q_0 is the maximum intensity, r_u and r_i define upper and the lower radius in the upper plane at $z=z_u$ and in the lower plane at $z=z_l$ respectively.
The parameter r_0 was decreased linearly from the top to the bottom surfaces and it can be expressed as:

$$r_o = r_u - \frac{(r_u - r_l)(z_u - z)}{(z_u - z_l)} \quad \text{Eq. 17}$$

6.3.4. 3D heat source model for the electric arc

The double-ellipsoidal heat source proposed by Goldak et al. [194] was employed to describe the arc power (Fig. 91). The heat source model, as displayed in Fig. 91, combines two different ellipses, i.e. one in the front quadrant of the power distribution (q_f) and the other in the rear quadrant (q_r).

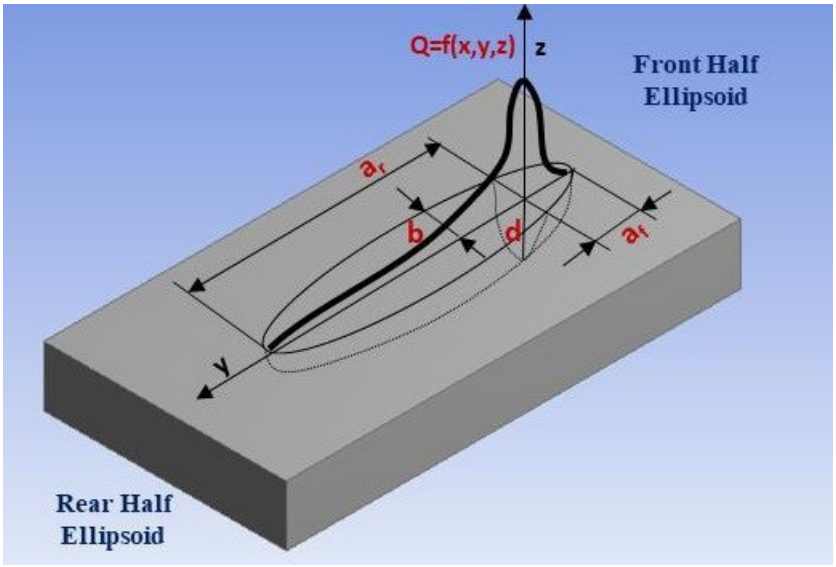

Fig. 91 *Goldak heat source distribution.*

Moving arc heat power distribution can be mathematically expressed as [194, 196]:

$Q(x, y, z) = q_f(x, y, z) + q_r(x, y, z)$

The mathematical definition of the heat source of the two different ellipses is defined by power distribution inside the front quadrant (Eq. 18) and for the rear quadrant (Eq. 19), respectively:

$$q_f = \frac{6\sqrt{3}f_f Q}{a_f bd\sqrt{\pi}} * exp(-\frac{3(x-vt)^2}{a_f^2} - \frac{3y^2}{b^2} - \frac{3z^2}{d^2}) \quad \text{Eq. 18}$$

$$q_r = \frac{6\sqrt{3}f_r Q}{a_r bd\sqrt{\pi}} * exp(-\frac{3(x-vt)^2}{a_r^2} - \frac{3y^2}{b^2} - \frac{3z^2}{d^2}) \quad \text{Eq. 19}$$

Principally, a_f symbolize the front length, a_r is the rear length, b and d are the width and depth, respectively (see Fig. 91). The welding speed is v and f_f and f_r are the proportion coefficients at front and rear ellipsoids. Q is arc power that was calculated by the following equation:

$$Q_{=\eta_a} IU \quad \text{Eq. 20}$$

I represents to the arc current. U symbolizes the arc voltage and η_a is the arc heat efficiency.
The heat source parameters will be engaged for the calibration of the model according to the welding parameters.

The temperature during the FEM analysis has reached 1923K by ensuring the material fusion (Fig. 92).

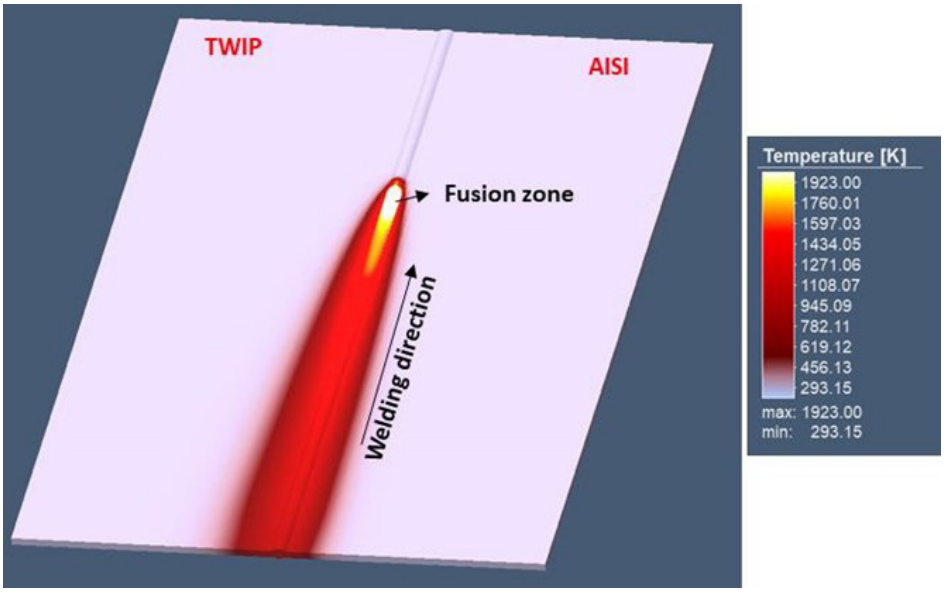

Fig. 92 *Temperature field of the welded plates.*

6.3.5. Mechanical analysis

Thermal analysis results were employed for mechanical analysis. During mechanical analysis, the same meshing sizes as those in thermal analysis was used. Temperature dependent mechanical properties of the material such as, Poisson's Ratio, Young's Modulus, and Yield Strength were taken into account in the FEM analysis simulation.

The distortions are defined as the buckling of the plates due to the contraction and expansion of the plate material during the welding processes. The total strain is defined by the following general equation [197, 198]:

$$\Delta\varepsilon = \Delta\varepsilon^{E} + \Delta\varepsilon^{p} + \Delta\varepsilon^{T} \qquad \text{Eq. 21}$$

Where $(\Delta\varepsilon^{E})$ define the elastic strain,$(\Delta\varepsilon^{p})$ represent the plastic component and $(\Delta\varepsilon^{T})$ represent the thermal loading.

Another boundary condition supposed that the plates were clamped to the worktable to avoid rotation and translation.

6.4. Results and discussion

6.4.1. Calibration of the model

After the simulation, the fusion zone in transversal plane was compared with the experimental one for calibration purposes.

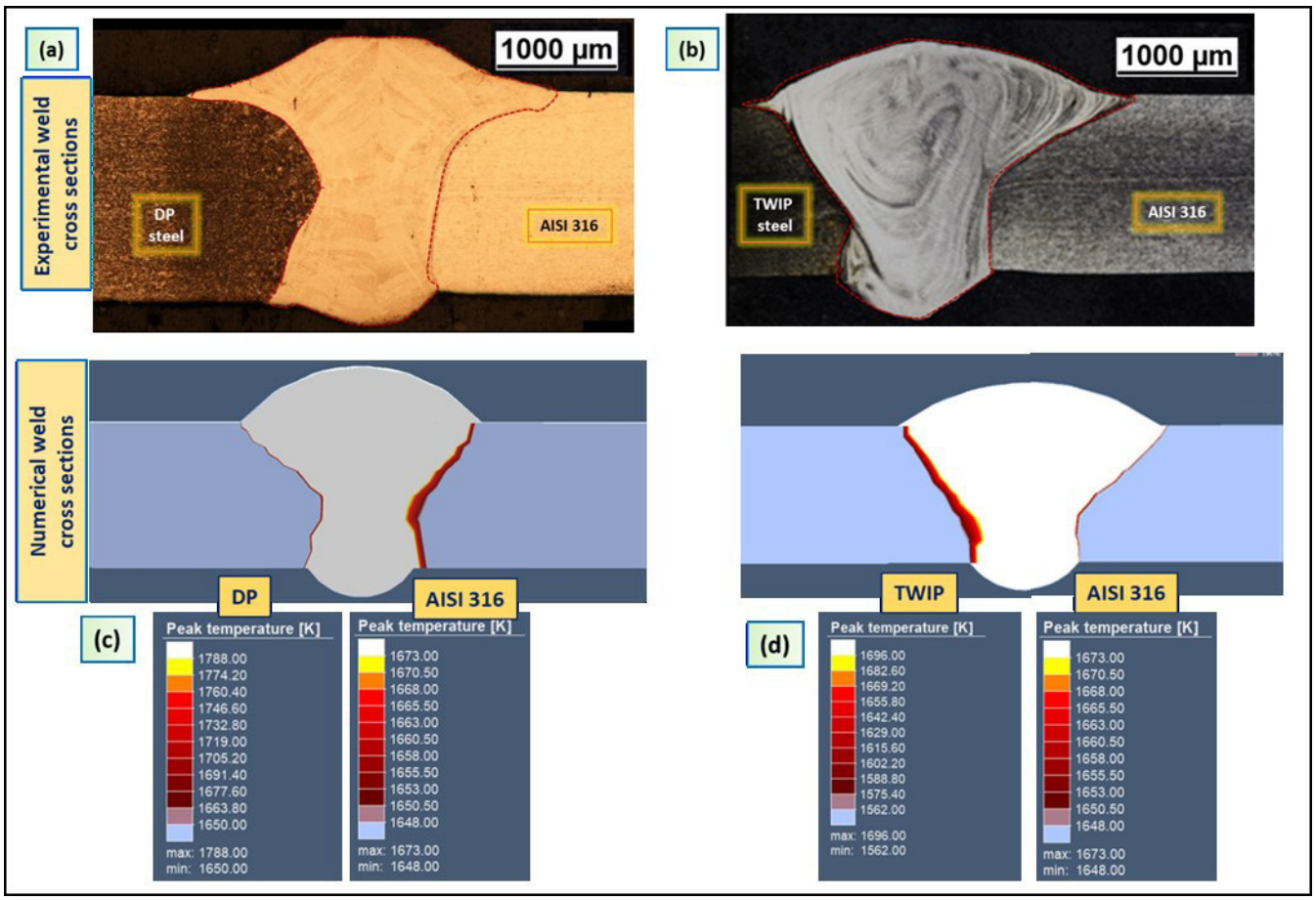

Fig. 93 *(a), (b) Macrographs after etching; and (c), (d) numerical weld cross sections.*

The fusion zones, after etching, were compared with the cross section obtained during welding simulations. Fig. 93 displays the comparison between the simulated and experimental fusion zone profile for the two joints: DP-AISI, TWIP-AISI. The geometry of molten pool was like that obtained in the welding process.

The above results can be quantified by measuring the dimensions of the fusion zone profile in the top, middle and bottom (see Fig. 94).

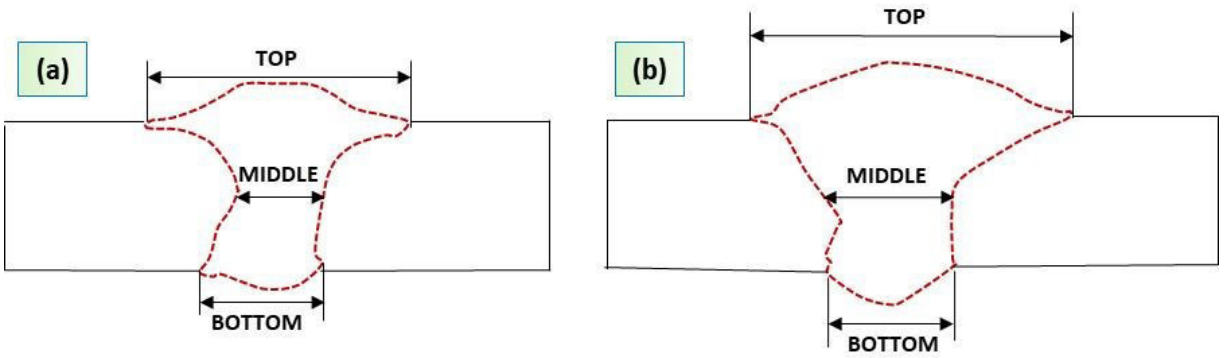

Fig. 94 *Drawing of weld cross sections: (a) DP-AISI 316 and (b) TWIP-AISI 316.*

In Tab. 17 and Tab. 18 the results simulation and the experimental measurements are reported. The numerical simulations display good agreement between the predicted and the measured values.

DP-AISI	Experimental Data (mm)	Numerical Data (mm)	Errors (%)
Top	2.5	2.4	4.0
Middle	0.8	0.75	6.3
Bottom	1.1	0.8	27.3

Tab. 17 *Comparison of experimental and numerical dimensions (mm) of the DP-AISI fusion zone.*

TWIP-AISI	Experimental Data (mm)	Numerical Data (mm)	Errors (%)
Top	3.2	2.9	9.4
Middle	1.1	1.2	9.0
Bottom	1.1	1.2	9.0

Tab. 18 *Comparison of experimental and numerical dimensions (mm) of the TWIP-AISI fusion zone.*

The 3D heat source used in the hybrid laser welding simulation was capable of modeling with adequate accuracy the shape of the fusion zone dimension and shape (see Fig. 93 c, d).

In the finite element analysis, the heat source parameters must be manipulated to calibrate the weld pool shape. The calibrate parameters were used during the thermal-mechanical analysis. Particularly, conical heat source for laser was define by three parameters, while a double ellipsoidal heat source for electric arc was describe through four parameters. Tab. 19 and Tab. 20 shows the parameters used to calibrate the two simulated models.

Symbol	Reference	DP-steel [mm]	TWIP-steel [mm]
r_u	Conical heat source upper radius	0,3	0,6
r_l	Conical heat source lower radius	0,6	0,12
d	Conical heat source depth	2,4	2,3

Tab. 19 *Parameters calibration of conical heat source for laser (*see Fig. 90).

Symbol	Reference	DP-steel [mm]	TWIP-steel [mm]
a_f	Front length	0,36	0,55
a_r	Rear length	1,5	1,9
b	Width	1,4	1,6
d	Depth	1,5	1

Tab. 20 *Parameters calibration of double-ellipsoidal heat source for electric* arc (see Fig. 91).

6.5. Models' validation

6.5.1. Thermal cycles results

To validate the model, was comparison the microstructure in the HAZ of DP steel forecasted using the thermal cycles with that coming from the CCT curve and the cooling speed. The thermal cycle was measured in different points of DP steels along the x direction. These points are located at -1,25 mm, -2 mm, -5 mm, respectively (see Fig. 95).

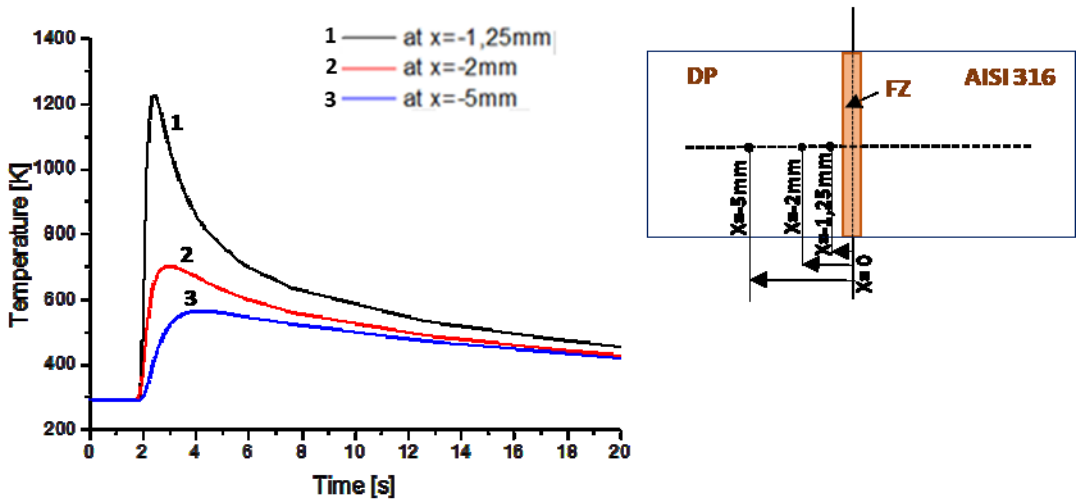

Fig. 95 *Thermal cycle in different points of DP steels along the x direction: x=-1,25mm, x=-2mm, x=-5mm, respectively.*

During the finite element analysis, high temperature gradient occurred at the weld zone due to the interaction the arc heating and laser energy. At the end of welding process, the welded plates cooled to

room temperature and the peak value of the temperature decreased. The metallurgical behavior followed the thermal cycles as showed in Fig. 95. Simufact allows describing the thermal cycles in order to verify the microstructure transformations.

The phase transformation in the HAZ DP steel were validated from the CCT curves. DP steel showed a substantial microstructural change in the heat affected zone due to the thermal cycle during the welding (Fig. 96 b, c). Based on the CCT diagram, at high cooling rates (v=81°C/s) martensite and bainite microstructures were detected. While at slow cooling rates (26°C/s and 21°C/s) a mixed microstructure was observed (Fig. 96 b, c).

CCT are displayed in Fig. 96a. [199 modified]. Optical micrographs of weld DP-AISI displayed the effect of cooling rate on the microstructure. As function of the distance from the fusion zone, HAZ can be divided into three sections, as follows:

- HAZ-1 where the rapid cooling favorites the formation of martensite.
- HAZ-2 where the martensitic transformation is partial.
- HAZ-3 this zone due to greater distance from fusion zone a martensitic and ferritic microstructure has been observed.

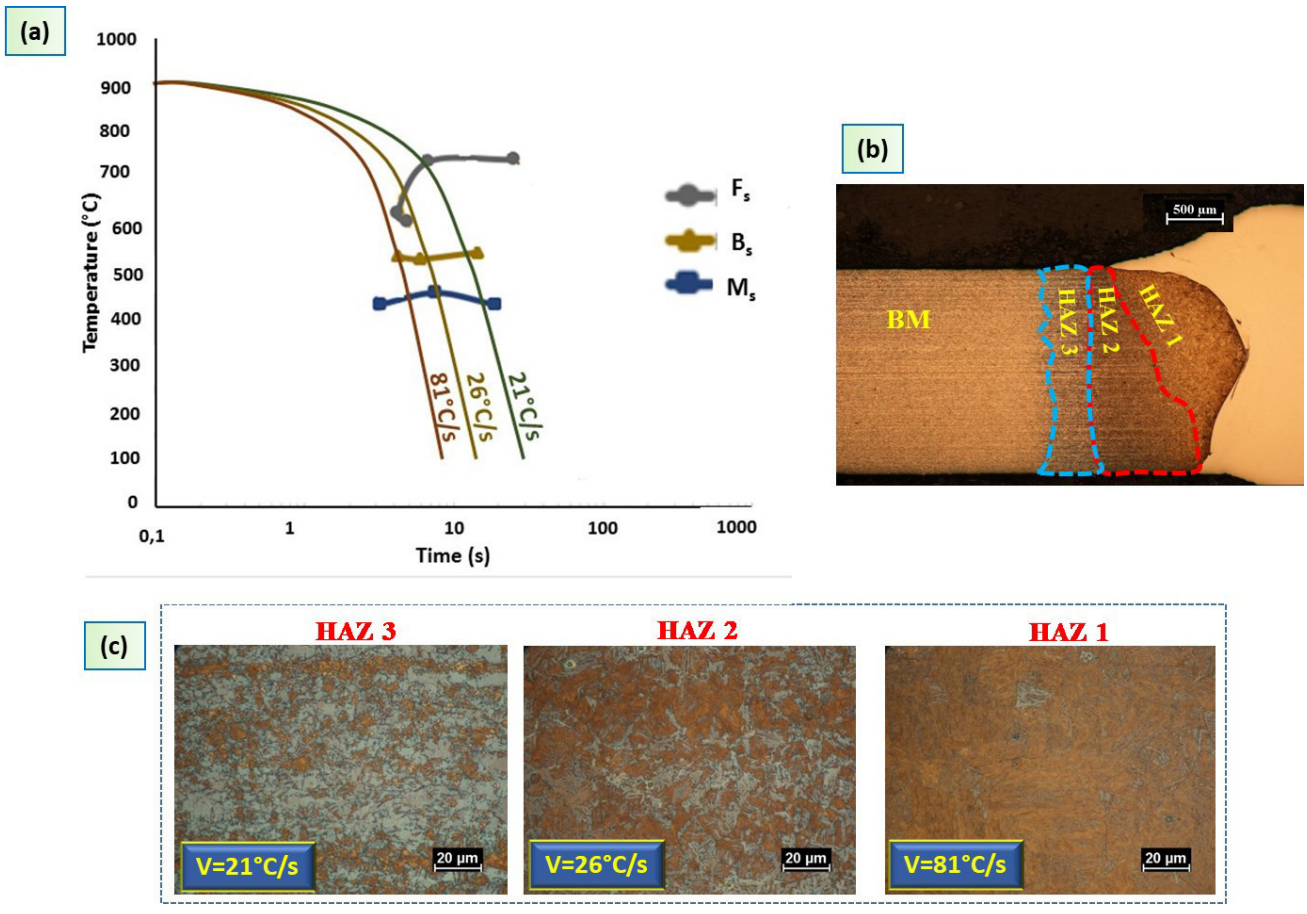

Fig. 96 *(a) Schematic representation CCT curves for DP steel; (b) Macrograph after etching show three section of the HAZ; (c) Details view of HAZ and their respective cooling rate.*

While, in the HAZ of TWIP steel a grain coarsening effect was detected. For TWIP steel, Fig. 97a displays the thermal cycle measured in four different points along the x direction.

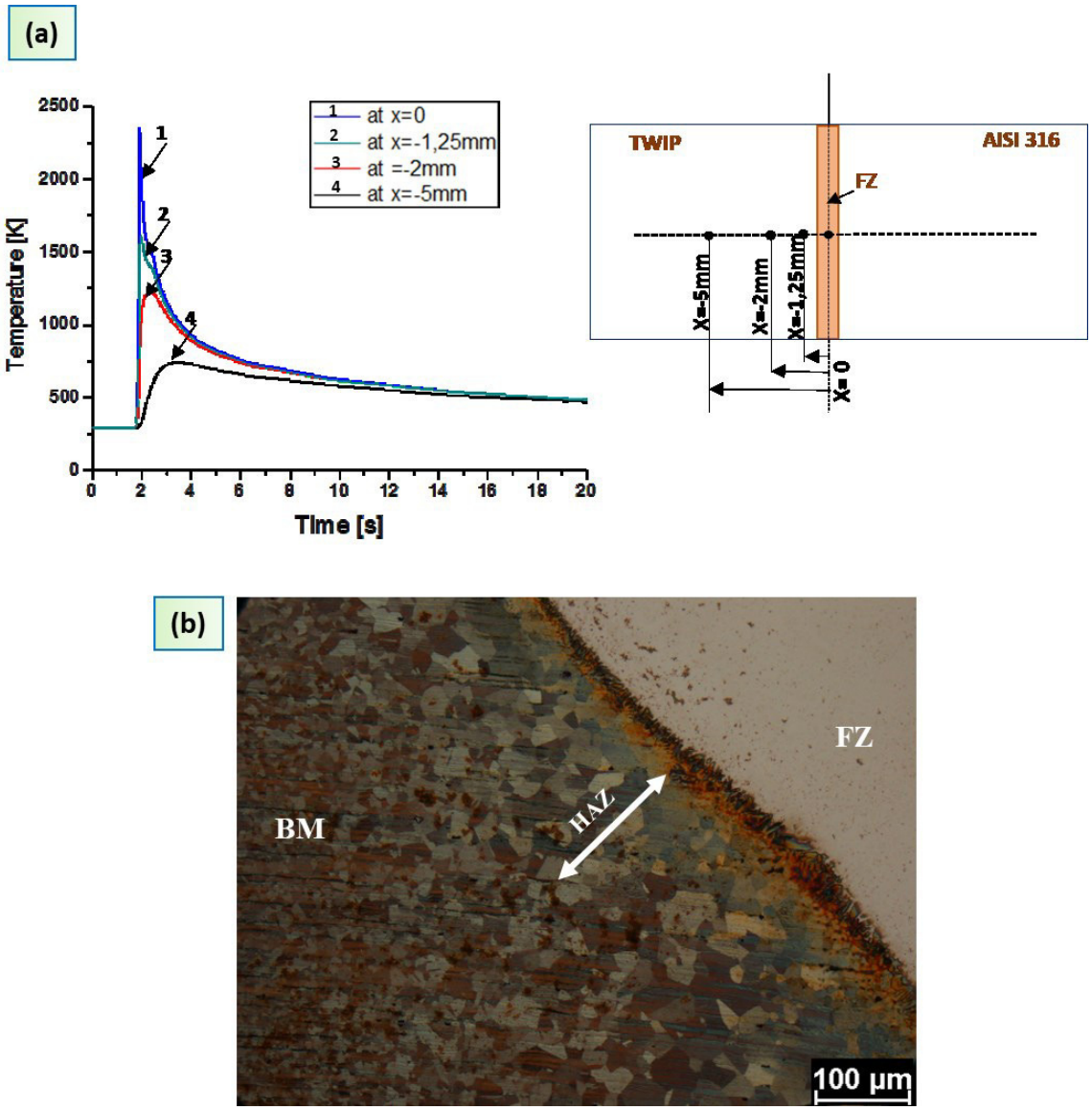

Fig. 97 *(a) Thermal cycles was measured in different points of TWIP steel along the x direction; (b) Micrograph, after etching, show a grain coarsening in HAZ and a fine austenitic microstructure in the base material.*

6.6. Distortion results

During welding process, several types of deformation (bending distortion, longitudinal shrinkage, buckling or angular distortion) occurred due on the welding parameters and mechanical clamping conditions. Moreover, during the hybrid welding process, big strain develops in the molten pool and near weld region. The plates displayed a distortion of about 2 mm (Fig. 98a). This value was evaluated using a software for the image analysis. Fig. 98b displays the simulated distortion values distribution in z direction after cooling and compared with the measured values. It was verified that the higher distortion

existed at the fusion zone and around HAZ (Fig. 98b). Consequently, the conical and double-ellipsoidal heat source model assumed predicted distortion profile comparable with that of the measured distortion.

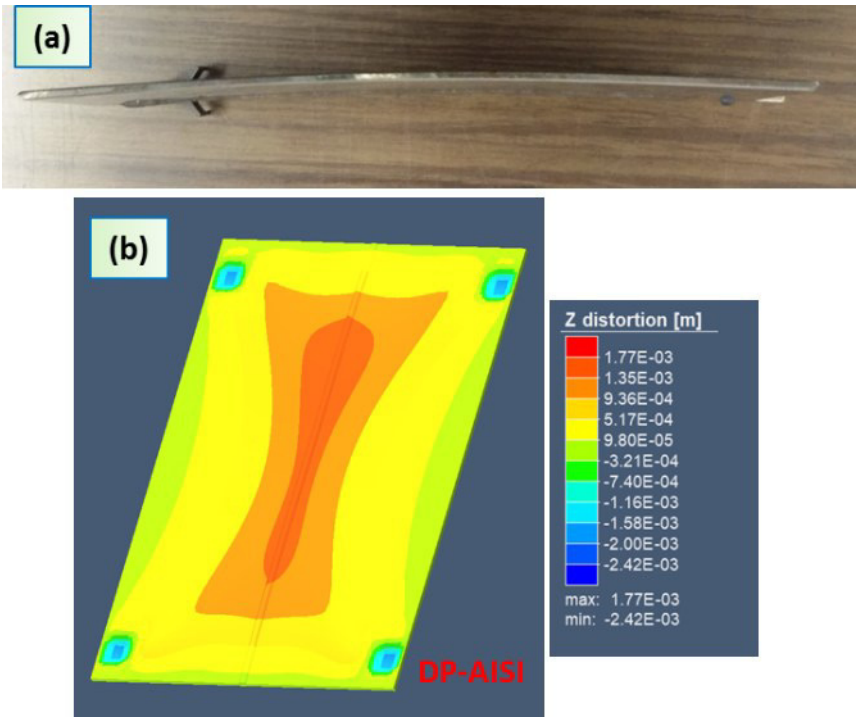

Fig. 98 *(a) Photo show distortion of the plate after welding; (b) Simulation of welding residual distortion of the plate DP-AISI.*

7. CHAPTER: FEM model for TIG hybrid laser butt welding of 6 mm thick austenitic to martensitic stainless steel

In this chapter, was analyzed a thermal simulation of plate butt joints austenitic stainless steel (AISI 304) and martensitic stainless steel (AISI 410) welded by fiber laser-TIG hybrid welding system. Three-dimensional (3D) Gaussian heat source to represent the laser power and Goldak's double ellipsoid to describe the arc power have been proposed. The models were calibrated comparing the fusion zones of experimental and numeric results and were validated by acquiring the effective temperature by the continuous cooling transformation (CCT) diagram.

7.1. Experimental set-up

A fiber laser-TIG welding butt joints have been produced from two plates of AISI 304 and AISI 410 stainless steel of 100mm x 80mm x 6mm (length x width x thickness), according to the scheme of Fig. 99.

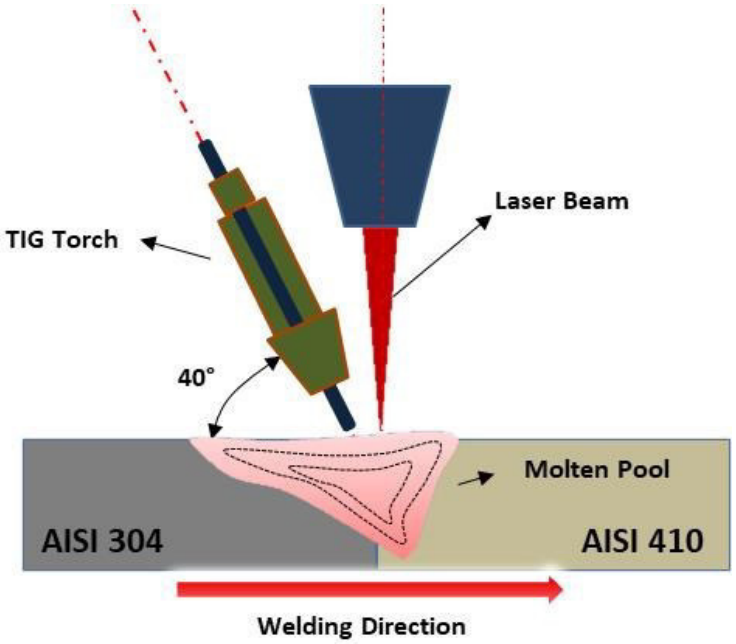

Fig. 99 *Scheme of laser TIG welding.*

Thermo-physical and mechanical properties of the stainless steel (AISI 304/AISI 410), such as thermal conductivity, density, Young modulus, have significant influences on the results of welding simulations [200]. In particular, mechanical and thermo-physical properties of stainless steel were given in Tab. 21. Particularly the thermal conductivity and density have been considered variable as a function of temperature (Fig. 100).

Property	AISI 304	AISI 410
Young modulus [GPa]	193	200
Poisson	0,29	0,27
Liquidus Temperature [K]	1728	1755
Solidus Temperature [K]	1673	1805

Tab. 21 *Mechanical and thermo-physical properties of stainless steel [201].*

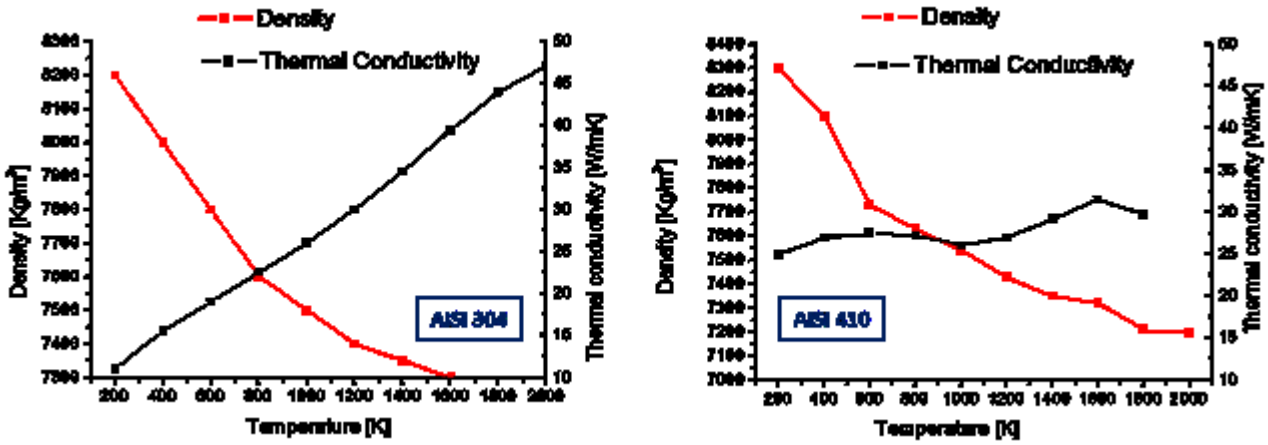

Fig. 100 *Thermal conductivity (W/mK) and density (Kg/m^3) as a function of temperature [201].*

7.2. Finite element analysis

In order to simulate, with satisfactory accuracy, the fiber laser-TIG hybrid welding, finite element software has been used. For this purpose, butt joints of 6 mm plates were modeled using the commercial code Simufact.

7.2.1. Geometry and mesh

A finite element analysis was developed to simulate fiber laser-TIG hybrid welding process. Fig. 101 displays the mesh employed during the FEM simulation. In order to obtain more accurate results, a fine mesh (element size 3.2 × 0.5 × 0.1 mm^3) was adopted at interface of the two plates (in the fusion zone and in HAZ). So, achieve accuracy of solution with reasonable calculation time. A coarse mesh was employed moving away from the weld centerline in order to reduce the calculation time (Fig. 101). The mapped mesh in the plats has 43000 elements.

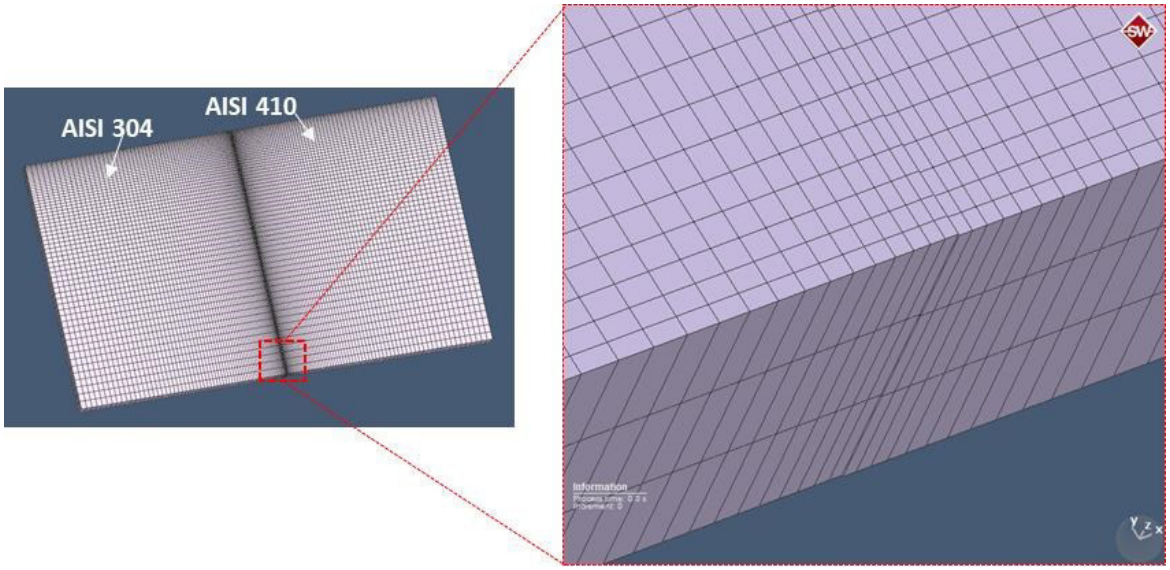

Fig. 101 *FEM model [201].*

7.2.2. Initial and boundary conditions

Fourier law describes the temperature in welding process (Eq. 22) [202, 203]:

$$\frac{\partial}{\partial x}\left(K_x \frac{\partial T}{\partial x}\right) + \frac{\partial}{\partial y}\left(K_y \frac{\partial T}{\partial y}\right) + \frac{\partial}{\partial z}\left(K_z \frac{\partial T}{\partial z}\right) + Q(x,y,z) = \rho c \frac{\partial T}{\partial t} \qquad \text{Eq. 22}$$

where, k_x, k_y and k_z represents the thermal conductivity in the x, y and z directions ($Wm^{-1}K^{-1}$), C is the specific heat capacity ($J\ kg^{-1}{}^{\circ}C^{-1}$), ρ is the density ($kg/m^3$), t is the time (s), and Q(x,y,z) represents internal heat generation rate per unit volume (W/m^3). In the welding process, the work piece, exchanges heat with the surrounding due to convection and radiation. According to Newton's law and Stefan-Boltzmann's law the heat losses is given by Eq. 23 [202, 204]:

$$-q = \varepsilon\sigma(T_r^4 - T^4) + h(T_r - T) \qquad \text{Eq. 23}$$

Where, σ represents Stefan Boltzmann constant ($5{,}67*10^{-8}$ W/m^2K), and ε is the emissivity, h is the convection heat transfer coefficient.

This coefficient can be assumed equal to 20 $W/(m^2K)$ for air and 200 $W/(m^2K)$ for the lower surface in contact with the work piece. While Tr represents the room temperature equal to 25°C. However, in order to avoid translation and rotation, the plates were clamped to the worktable. While at time t = 0 T (x, y, z, 0) = 25°C.

7.3. Moving distributed heat source

In order to simulate the distribution of temperatures in fiber laser-TIG hybrid welding process two different heat source models have been modelled. In this chapter, as illustrated in Fig. 102, the best heat source model for simulating laser welding process was a cylindrical Gaussian heat source.

While the Goldak's double-ellipsoid heat source model was assumed to define the arc power. However, the choice of heat source models to define the power distribution is essential to precisely model the welding heat source in order to find a relationship with the weld profile.

Consequently, as described below, in order to simulate hybrid welding process is crucial calibrate the heat source parameters, that will be examined in this work. Fig. 102 displays parameters that describe the size and shape of the molten pool.

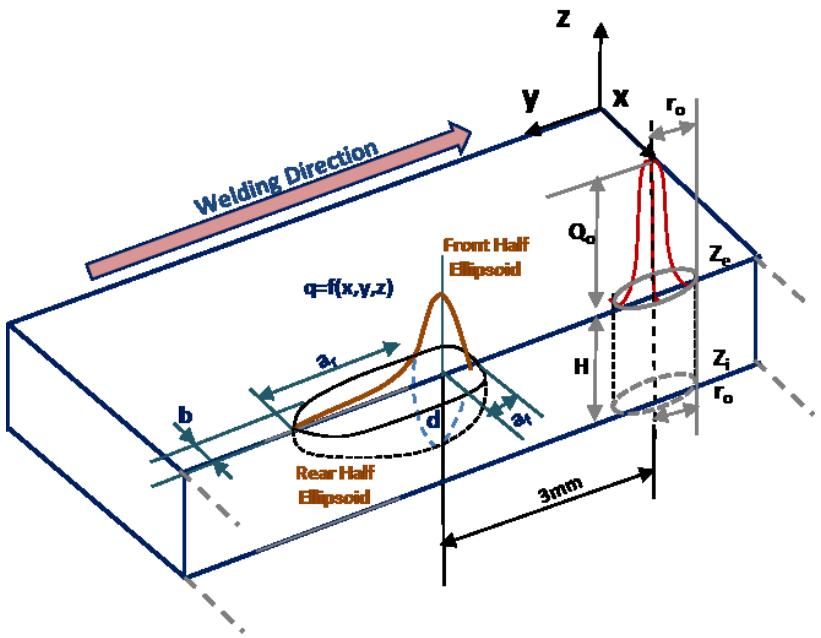

Fig. 102 *Cylindrical and double-ellipsoidal heat source model [201].*

7.4. Result and discussion

7.4.1. Calibration of the model

After the simulation, the fusion zone in transversal plane was compared with the experimental one for calibration purposes. In order to predict the dimensions of the weld transversal section by the numerical model, experimental welds were prepared and measurements were taken for their Width of Crown Zone (WCZ), Depth of Crown Zone (DCZ), Depth of Laser Zone (DLZ) and Width of Crown Zone (WCZ) (see Fig. 103 for display).

These measurements were used for the calibration of the heat sources to be used during the FEM simulation. The calibration process was a trial-and-error one.

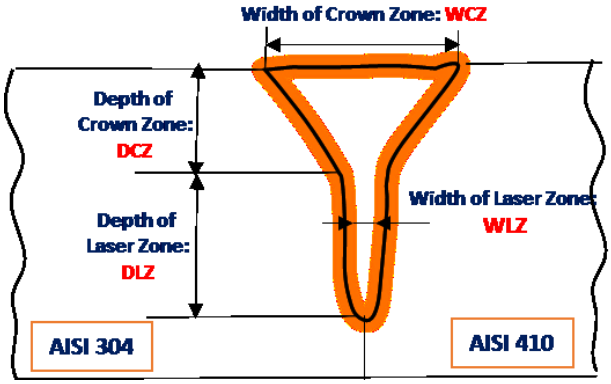

Fig. 103 *Sketch of weld cross section [201].*

In order to obtain the accuracy of the simulation, the heat source parameters must be manipulated to achieve the dimensions of the numerical cross section, which match those of the experiments. This phase is paramount because the accuracy of the FEM simulation depends strongly on its accuracy.

A cylindrical heat source model was chosen for the laser source and its dimensions were defined by three parameters. Otherwise, a double ellipsoidal heat source model was used for the arc source that required four parameters (see Fig. 102).

Tab. 22 and Tab. 23 display the adopted parameters for the two heat sources at the end of the calibration process.

Symbol	Meaning	S1	S2	S3	S4
r_0	Upper-lower radius (mm)	0.5	0.6	0.5	0.6
d	Depth (m)	4.0	5.0	4.5	5.0

Tab. 22 *Cylindrical heat source parameter [201].*

Symbol	Meaning	S1	S2	S3	S4
a_f	Front length (mm)	0.55	0.55	0.55	0.55
a_r	Rear length (mm)	2.0	3.0	2.0	3.0
b	Width (mm)	1.5	2.0	1.8	4.5
d	Depth (mm)	1.5	0.5	0.5	0.5

Tab. 23 *Double-Ellipsoidal heat source parameters [201].*

The calibration was obtained by comparing the cross sections obtained by the numerical simulations with the cross sections obtained during hybrid laser welding simulations.

In Tab. 24, Tab. 25, Tab. 26 the sizes of the fusion zones and HAZ the experimental measurements are reported. are shown in Tables 6-9. Otherwise, the dimensions of the FZ profiles can be observed in Fig. 104b and Fig. 105b. It was detected that the numerical models for the weld joints was in good agreement between the predicted and the measured study.

Fig. 104c and Fig. 105c displays a good match between the temperature field produced by fiber laser-TIG hybrid welding and those predicted by software.

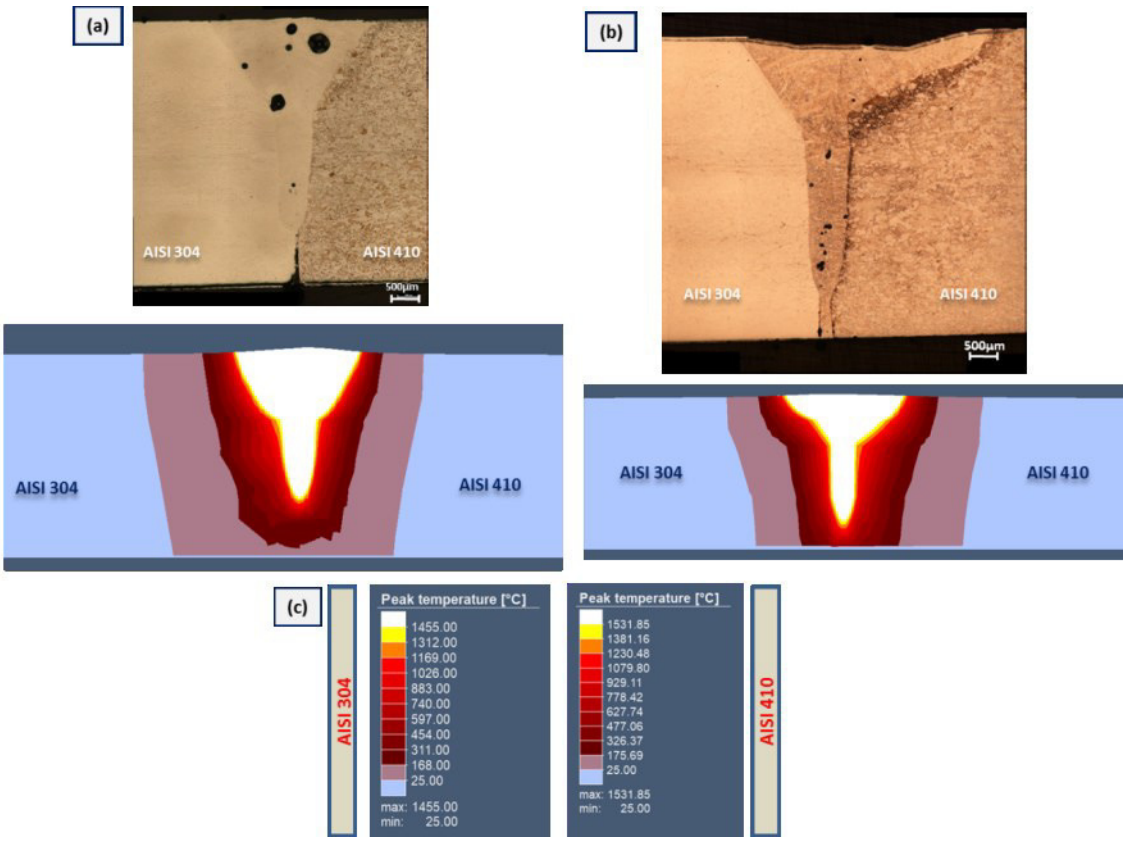

Fig. 104 *Welds (a) S1 and (b) S2 experimental and (c) numerical cross sections with temperature [201].*

S1	Experimental data (mm)	Numerical data(mm)
HAZ	0.4	0.3
WCZ	3.7	3.6
DCZ	2.1	2.1
WLZ	0.8	0.9
DLZ	2.3	2.3

Tab. 24 *Comparison of experimental and numerical weld dimensions for sample S1 [201].*

S2	Experimental data (mm)	Numerical data(mm)
HAZ	0.5	0.4
WCZ	4.5	4.3
DCZ	1.5	1.7
WLZ	0.8	0.8
DLZ	3.1	3.1

Tab. 25 *Comparison of experimental and numerical weld dimensions for sample S2 [201].*

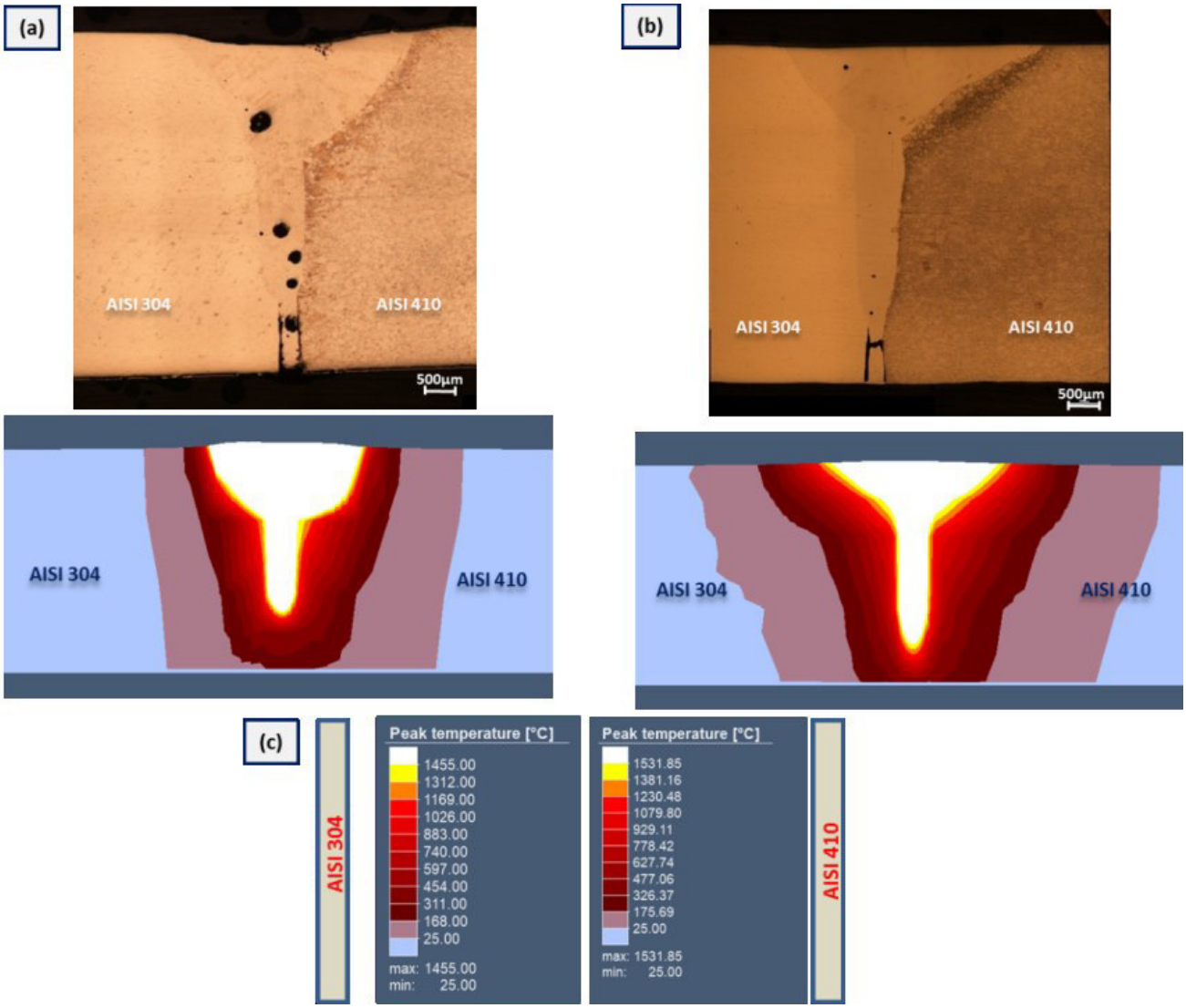

Fig. 105 *Welds (a) S3 and (b) S4 experimental and (c) numerical cross sections with temperature [201].*

S3	Experimental data (mm)	Numerical data(mm)
HAZ	0.3	0.2
WCZ	4.3	4.1
DCZ	1.9	2.0
WLZ	0.8	0.8
DLZ	2.5	2.4

Tab. 26 *Comparison of experimental and numerical weld dimensions for sample S3 [201].*

S4	Experimental data (mm)	Numerical data(mm)
HAZ	0.5	0.6
WCZ	5.0	4.7
DCZ	1.8	1.7
WLZ	0.9	0.8
DLZ	3.6	3.4

Tab. 27 *Comparison of experimental and numerical weld dimensions for sample S4 [201].*

The liquidus and solidus temperatures were 1455°C and 1400°C for AISI 304 and 1531°C and 1482°C for AISI 410, respectively.

Consequently, the calibration of heat source parameters depicts with accuracy the shapes of molten pool and HAZ.

7.4.2. Model validation

The model was validated by comparison of the microstructure in the HAZ of AISI 410 predicted using the thermal cycle with that coming from the CCT curve and the cooling speed (Fig. 106b). The thermal cycle was measured at a point in the HAZ of the AISI 410 (Fig. 106a).

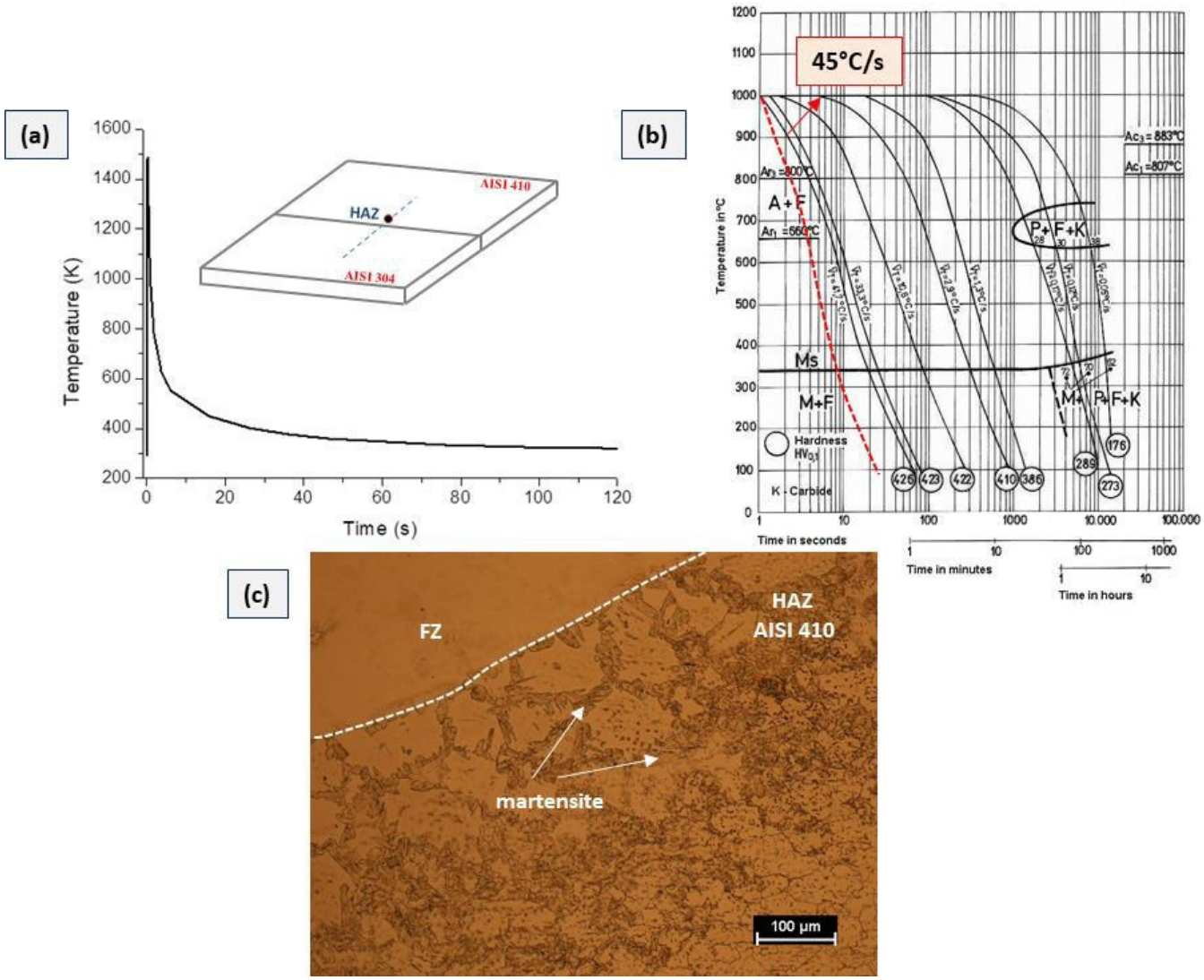

Fig. 106 (a) Thermal cycle evaluated in HAZ of AISI 410*; (b) CCT curve for AISI 410 and its respective cooling rate; (c) Detail view of HAZ shows continuous layer of martensite.*

Based on the CCT diagram [205], at high cooling rates (v=45°C/s) martensite and ferrite microstructures were observed. Optical micrograph displays the microstructures at interface (Fig. 106c).

During the hybrid laser welding, in the HAZ of AISI 410, the microstructure was partially martensitic. In the HAZ the thermal cycle induced by the process promotes the formation of a continuous layer of martensite at the ferrite grains boundaries during the heating (Fig. 106c). The transformation is incomplete due to the short time in temperature so, after cooling, the HAZ microstructure is only partially martensitic (Fig. 106c).

8. CHAPTER: Conclusions

The content of this thesis dealt with laser/hybrid laser welding of dissimilar metals, mostly used in the automotive industry. Laser welding offers many benefits, as it uses a concentrated heat source that allows high-quality junction ones. However, this junction process presents same limitations: for some alloys, susceptibility to cracks and porosity, strict tolerances for edges preparation, and high reflectivity. Hybrid laser arc welding overcomes some of those limitations. In fact, there are numerous advantages for this welding process. Hybrid laser welding is promising welding technique to join traditional and AHSS sheets in the automotive industry in order to obtain the best quality in terms of mechanical and metallurgical characteristics of the joint. Among dissimilar metal weld, aluminum/steel (Al/Fe), advanced high strength steel (AHSSs) /austenitic stainless steel present numerous difficulties, which are related to the metal properties. To improve the weldability, laser and arc welding of TWIP steels with DP steels (or TWIP/DP steel with austenitic stainless steel) require appropriate filler metals to avoid the occurrence of brittle metallurgical compound formation in the fusion zone, including manganese segregation and martensite formation, which reduces the weld ductility and toughness. Moreover, the use of an innovative fiber laser-TIG hybrid welding system to join dissimilar stainless steel permits to improve weldability and reduces the weld defects.

In the case of dissimilar stainless steel, a high efficiency fiber laser-TIG hybrid welding system was used to join AISI 304 and AISI 410 stainless steel plates. In this study, it was demonstrated that the use of a hybrid welding source allowed to solve many problems connected with the fabrication of dissimilar stainless steel joints. The microstructure of the weld fused zone, of dissimilar AISI 304/AISI 410 joints, was predominantly martensitic, also confirmed, by the increase in micro-hardness. The heat affected zone of the AISI 410, was only partially martensitic. The ferrite grain boundaries, in the HAZ of the AISI 410 had a continuous layer of martensite, which had formed at elevated temperature. While, in the HAZ of AISI 304, was generally constituted by an austenite matrix. At interface FZ/HAZ AISI 304 stringer of untreated ferrite delta has been observed. The formation of ferrite stringers along HAZ grain boundaries could limit the grain growth. However, porosity reached a minimum, when the maximum values were used for laser line energy and arc current. Therefore, it was possible improve the mechanical strength of dissimilar stainless steel the smallest percentage of martensitic. Eventually, this study demonstrated the good and easy weldability of dissimilar austenitic and martensitic stainless steel in annealed condition by fiber laser coupled with an electric arc.

Regards to hybrid laser-MAG welding of dissimilar DP/TWIP, the austenitic filler (316L-Si/SKR-Si austenitic stainless steel), was chosen in order to dilute the high Manganese content of TWIP steel, which can cause brittleness in the joints. However, the tensile test demonstrated that the hybrid welding and austenitic filler can have a positive effect on the weldability of the DP-TWIP dissimilar joint.

For hybrid laser welding DP/TWIP steels with austenitic stainless steel (AISI 316), the microstructures, mechanical properties and bending were analyzed. In particular, the heat affected zone on the TWIP side was fully austenitic and showed grain coarsening effect. In fact, HAZ hardness values was slightly lower than that of the corresponding base material, which was due to the coarsening of austenitic grains during the welding process. On DP steel side new martensite formed close to the fusion zone. The amount of martensite in the HAZ decreased with the distance from the fusion zone.

Hybrid laser-MAG welding can improve the mechanical strength. In fact, the bending tests confirmed the attitude of the weld towards ductility. Both samples show defect-free surface and cross section. Therefore, MAG-laser welding can be a valid means for real "tailor-made" solution for steel sheet welding in the automotive industry.

In the case of Al/Fe dissimilar welds obtained by fiber off-set and hybrid laser welding, due to of differences in the chemical composition of base metal and filler material the structures near the fusion line are very complex. Particularly the microstructure and the intermetallic compound formed, can affect significantly the mechanical properties of the joints. With thorough investigations on the intermetallic layer, its composition has been identifying. This layer is characterized by $FeAl_3$, FeAl, $FeAl_2$ Fe_2Al_5 and Fe_3Al compounds. Specifically, $FeAl_2$ nucleates on the aluminum side. The reason for this is that more stable compounds (such as Fe_2Al_5), being diffusion controlled, do not have enough time to growth during the cooling of the joint, while some other less stable compounds (such as $FeAl_2$) could nucleate and growth preferentially. However, full penetration and low defectiveness were reached by laser offset welding. Moreover, the high cooling rate enabled short reaction time and narrow IMC layer. Such a result is beneficial for enhancing mechanical properties. Consequently, hybrid laser-arc welding resulted less reliable. Because the large difference in thermal and fluid-dynamical properties of the two metals, promote the formation of irregular and non-homogeneous intermetallic layer. Excessive weld metal was observed at the top surface, while the bottom part presented a lack of penetration. It can be concluded that LOW effects on Al–Fe dissimilar metallurgy and IMC can be controlled better than those of the hybrid laser-arc welding. Therefore, further investigation on the weldability of Al–Fe dissimilar welds will focus on the LOW welding technique.

In order to evaluate the temperatures, distortions and metallurgical transformation during the welding process, a numerical model for the butt DP/TWIP with AISI 316 and AISI 304/AISI 410 stainless steel dissimilar weld was developed. 3D heat source was considered for both sources. 3D heat source with a Gaussian distribution was adopted for the laser welding simulation and Goldak heat source distribution was used for electric arc. Particularly, the calculations for the fusion zones dimensions and shapes were accurate for the 3D heat source. It was demonstrated that the 3D and a double-ellipsoidal heat sources can be used for hybrid welding simulation with satisfactory accuracy and a low time-consuming procedure. Further development of this investigation will concern the definition of a mathematical link between the welding parameters and the numerical parameters of the power distribution.

Graphical Abstracts

Study on the fiber laser/TIG weldability of AISI 304 and AISI 410 dissimilar weld

[G. Casalino, A. Angelastro, P. Perulli, K. Casavola, V. Moramarco, Study on the fiber laser/TIG weldability of AISI 304 and AISI 410 dissimilar weld, Journal of Manufacturing Processes, 35, (2018), 216-225]

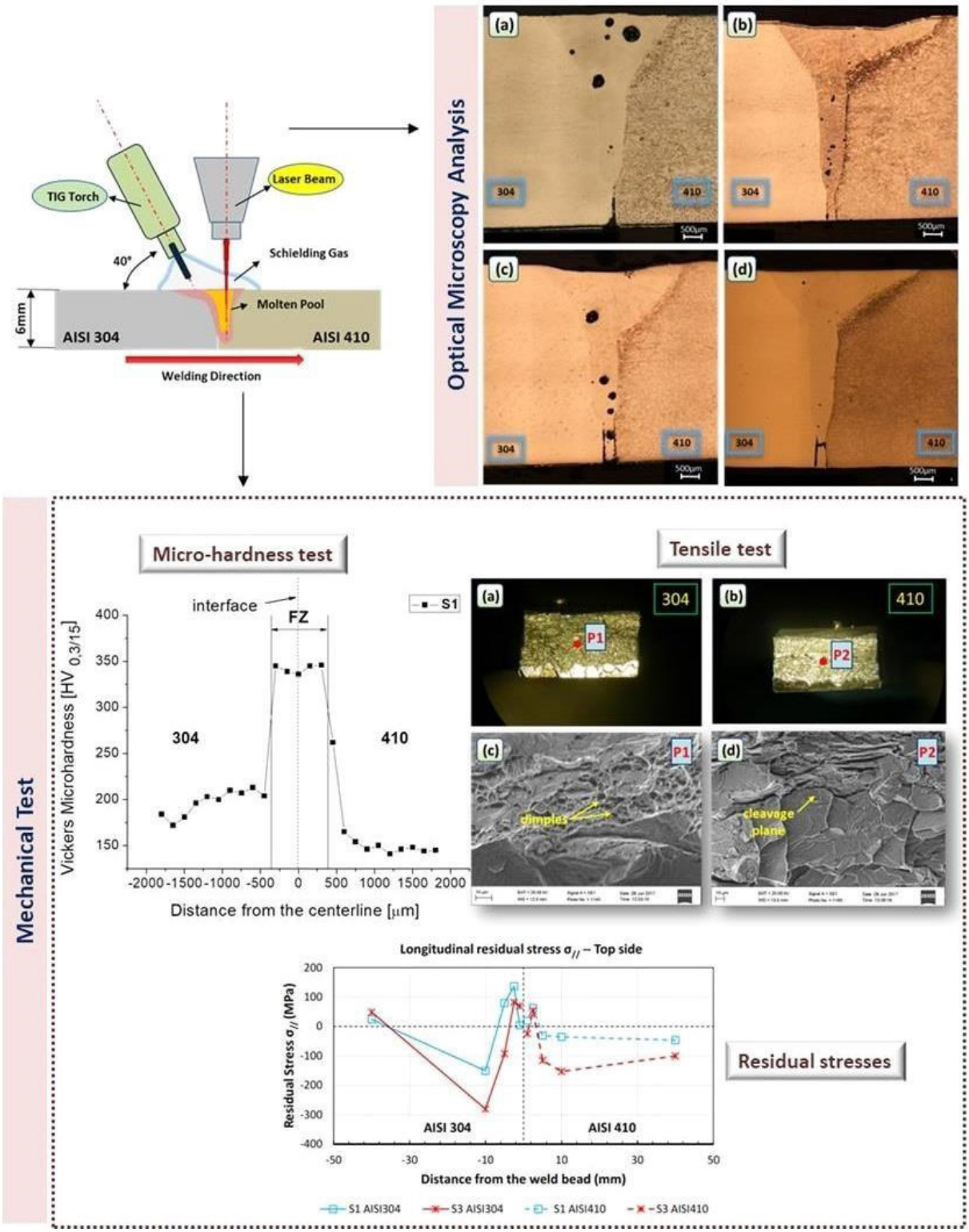

Weldability of TWIP and DP steel dissimilar joint by laser arc hybrid welding with austenitic filler

[A. Angelastro, G. Casalino, P. Perulli, P. R. Spena,– 11th CIRP Conference on Intelligent Computation in Manufacturing Engineering, CIRP ICME' 2017, Gulf of Naples, Italy, Procedia CIRP 67 (2018) 607 – 611]

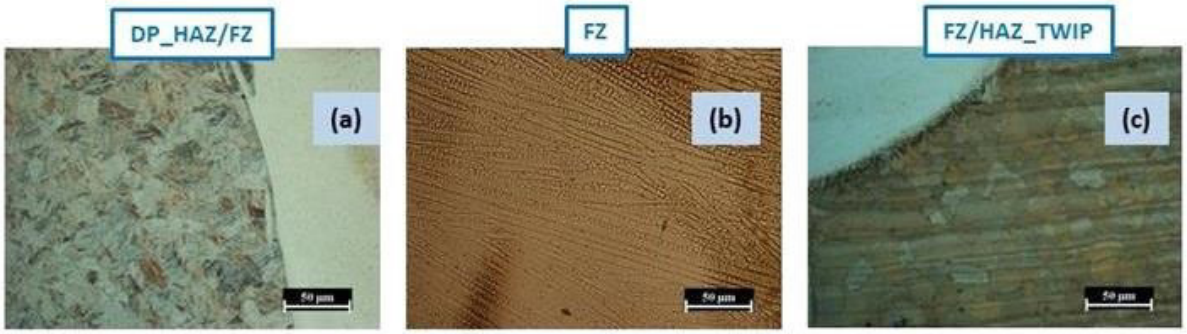

Metallographic Analysis

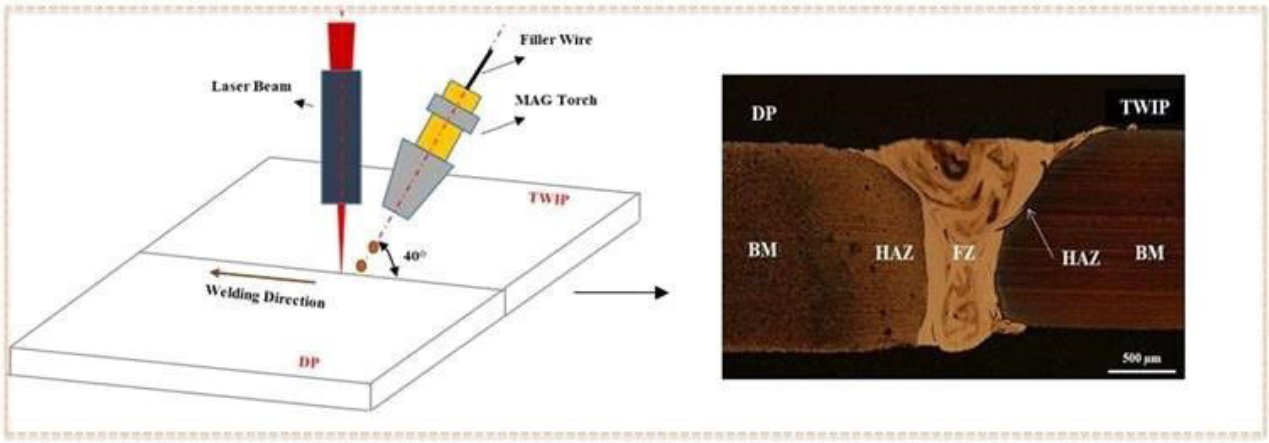

Mechanical Test

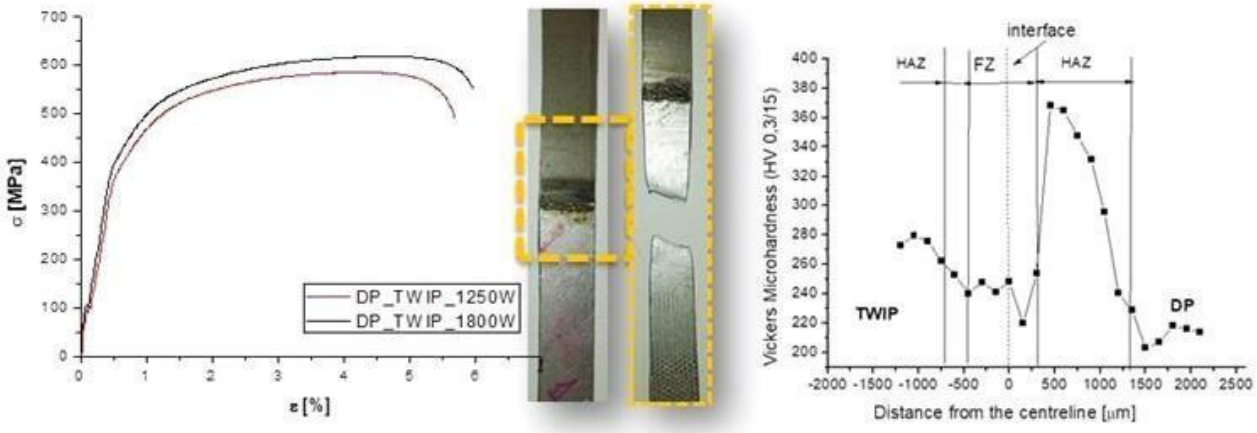

Fiber laser-MAG hybrid welding of DP/AISI 316 and TWIP/AISI 316 dissimilar weld

[G. Casalino, A. Angelastro, P. Perulli, P. Posa, P. R. Spena, 12th CIRP Conference on Intelligent Computation in Manufacturing Engineering, 18-20 July 2018, Gulf of Naples, Italy, Procedia CIRP 79 (2019) 153–158]

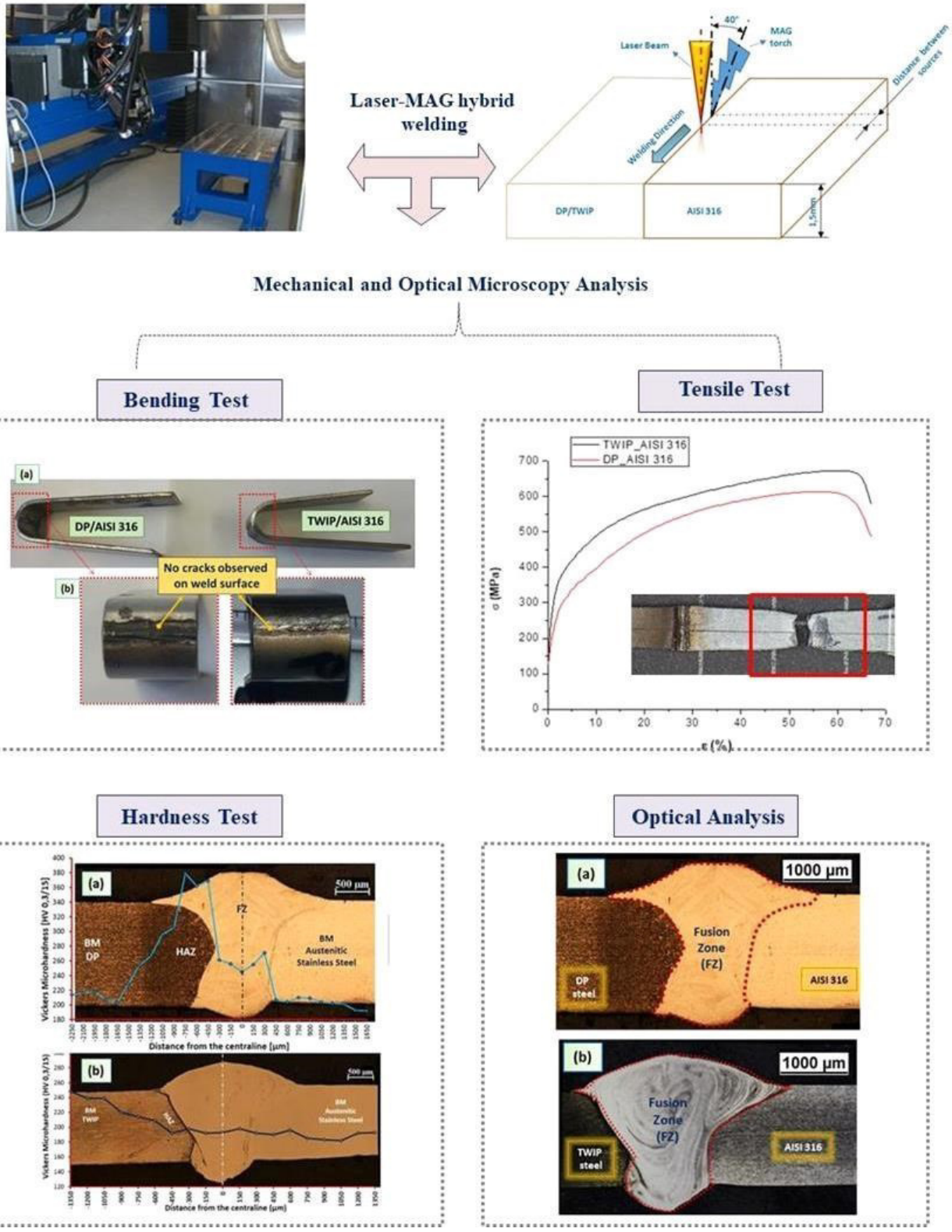

Effects of Laser Offset and HybridWelding on Microstructure and IMC in Fe–Al DissimilarWelding

[G. Casalino, P. Leo, M. Mortello, P. Perulli, A. Varone, Effects of Laser Offset and Hybrid Welding on Microstructure and IMC in Fe–Al Dissimilar Welding, Metals, 7, (2017), 282]

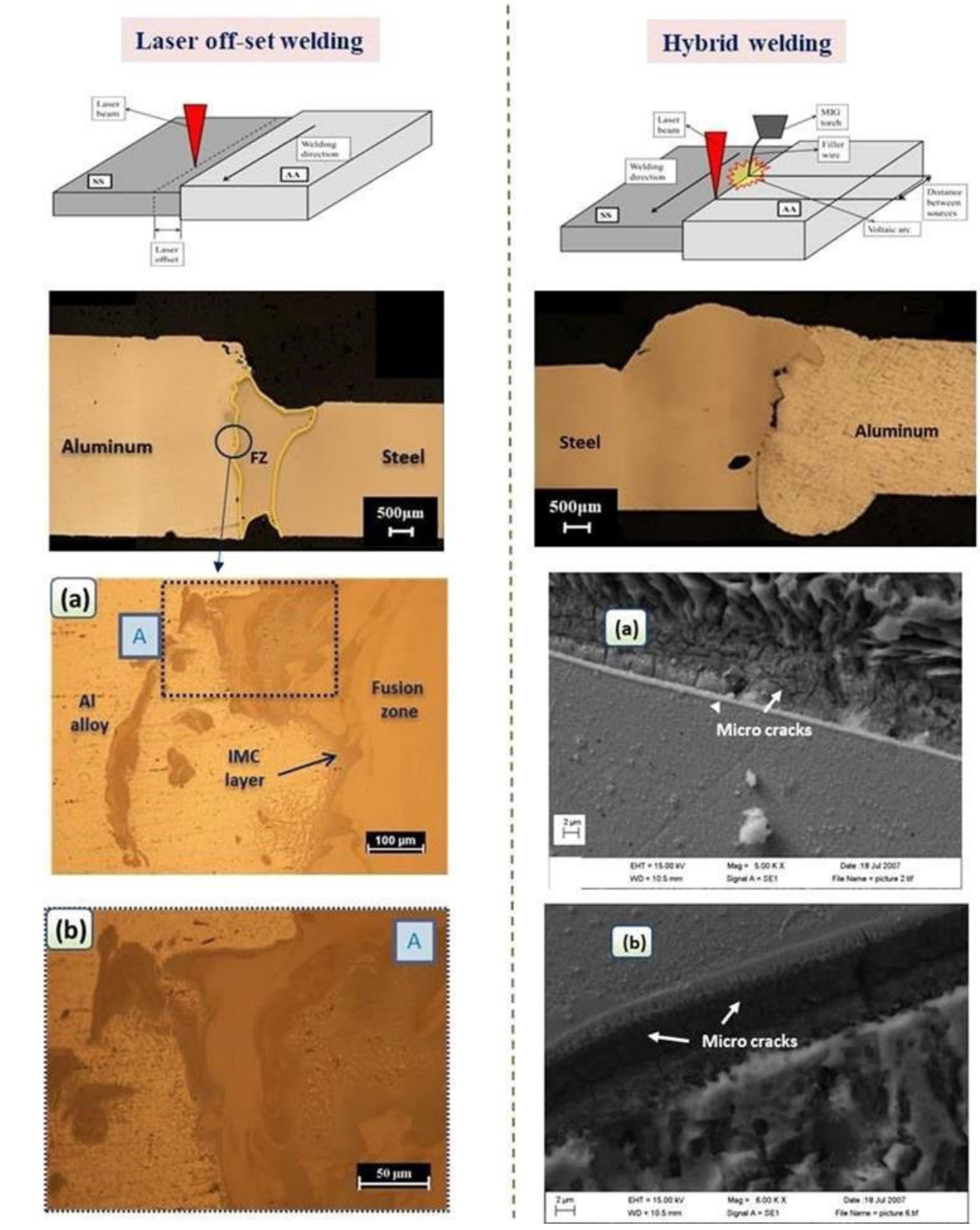

FEM model for TIG hybrid laser butt welding of 6 mm thick austenitic to martensitic stainless steels

[G. Casalino, M. Dassisti, P. Perulli, FEM model for TIG hybrid laser butt welding of 6 mm thick austenitic to martensitic stainless steel, 13th CIRP Conference on Intelligent Computation in Manufacturing Engineering, 17-19 July 2019, Gulf of Naples, Italy]

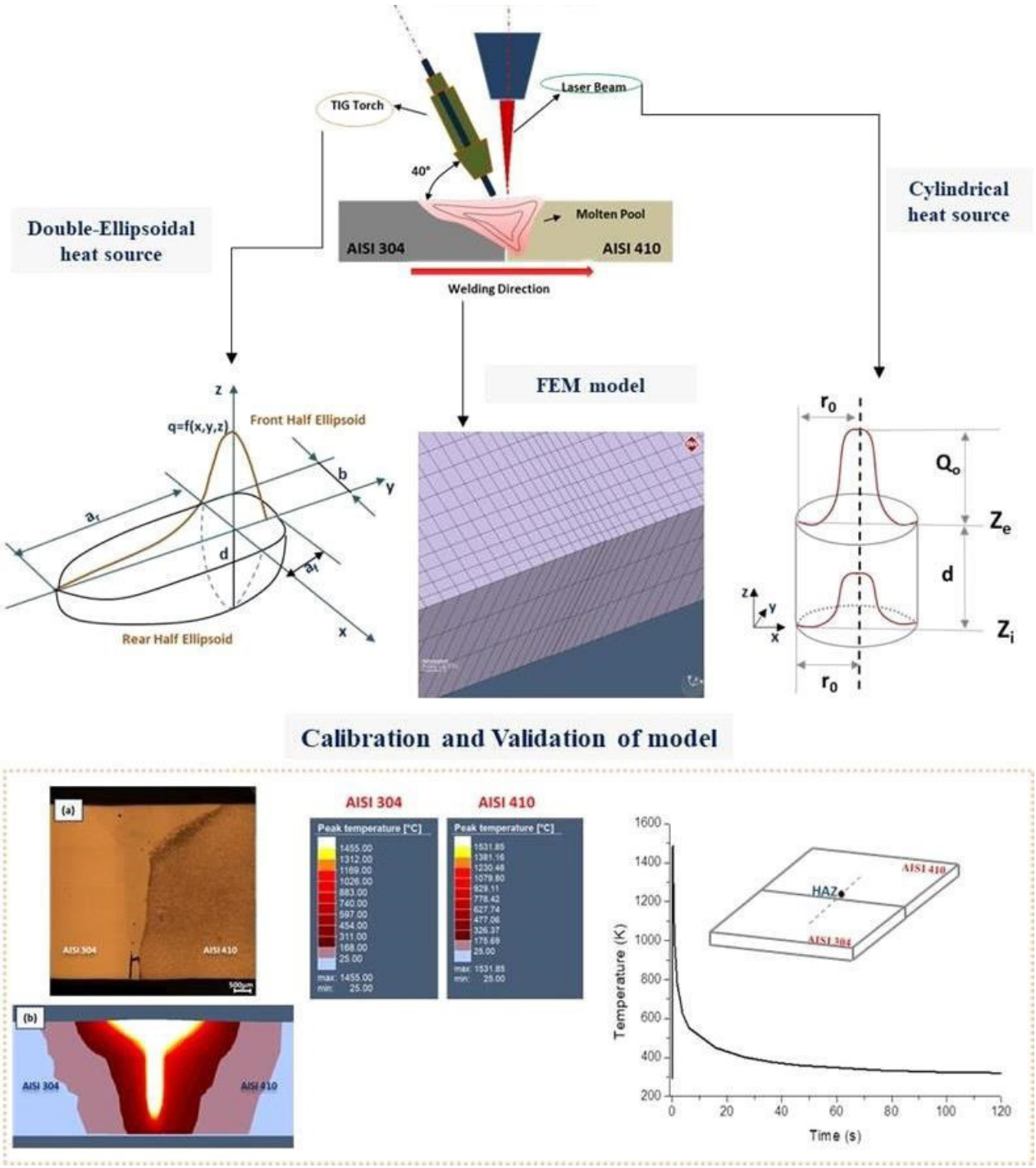

Thermo-mechanical simulation of fiber laser-arc welding of DP/AISI 316 and TWIP/AISI 316 dissimilar joints

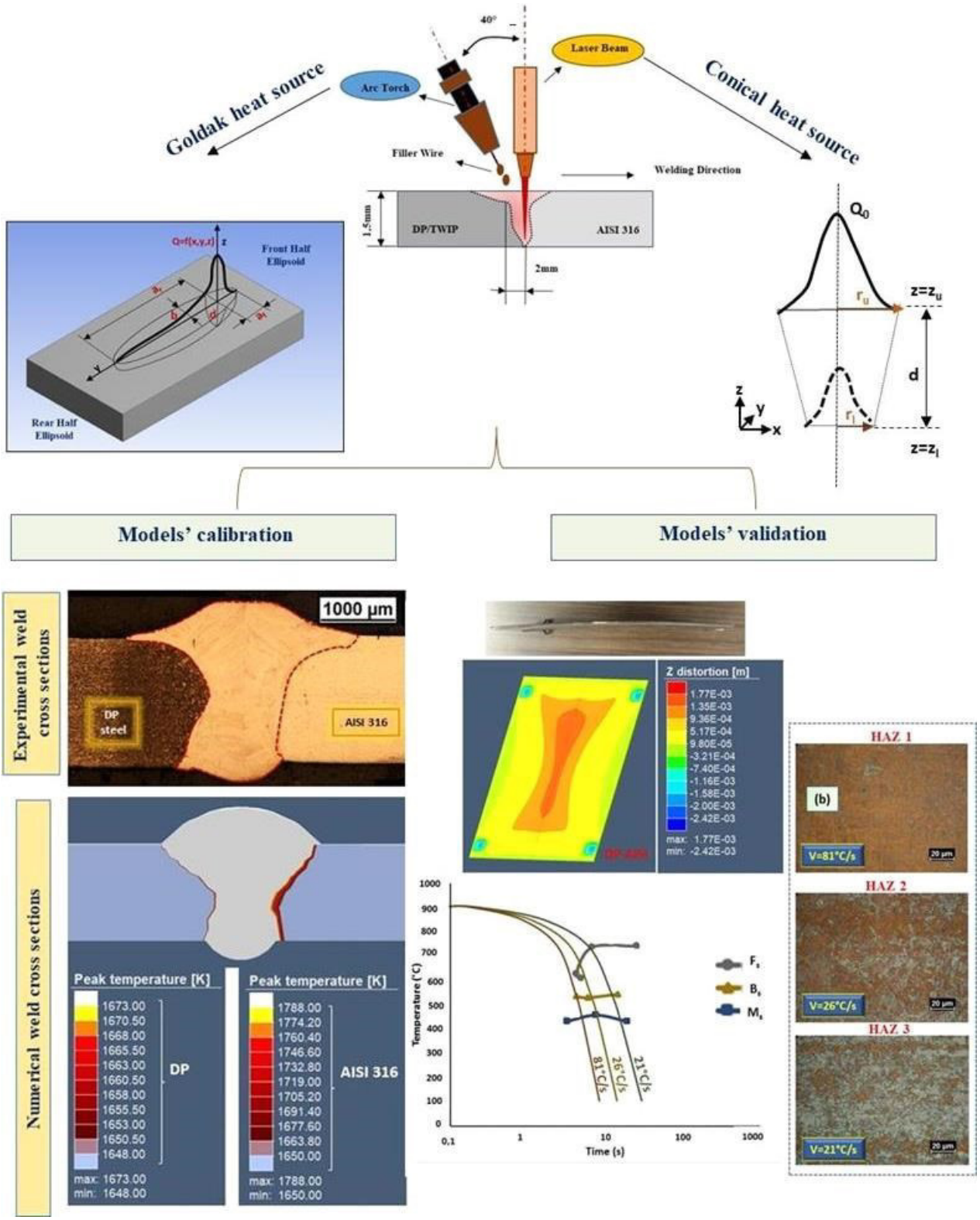

BIBLIOGRAPHY

[1] R.W. Messler, Principles of Welding, Wiley-VCH, 2004.

[2] G. Casalino, Advances in welding metal alloys, dissimilar metals and additively manufactured parts Metals, 7, (2017), p. 32.

[3] E. Kaiser, P. Schafer, Pulse sharping optimizes the quality of seam and spot welds, proceeding of the third international WLT, Conference on Lasers in Manufacturing (2005).

[4] F. Olsen, Hybrid Laser-arc Welding, Woodhead Publishing, Cambridge UK, 2009.

[5] I.N. Fridlyander, V.G. Sister, O.E. Grushko, V. Berstenev, L.M. Sheveleva, L.A. Ivanova, Aluminum alloys: Promising materials in the automotive industry. Metal Science and Heat Treatment, (2002), 44, 365–370.

[6] E. Evin, T. Miroslav, The Influence of Laser Welding on the Mechanical Properties of Dual Phase and Trip Steels. Metals 2017; 7, 239.

[7] S. D'Ostuni, P. Leo, G, Casalino, FEM Simulation of Dissimilar Aluminum Titanium Fiber Laser Welding Using 2D and 3D Gaussian Heat Sources, Metals, (2017), 7, 307

[8] T. Han, S. S Park, K-H. Kim, C.Y. Kang, I.-S. Woo and J. B. Lee, CO_2 Laser Welding Characteristics of 800 MPa Class TRIP Steel. ISIJ International, 45, (2005), pp. 60–65.

[9] C. J. Dawes, Laser Welding in Automobile Manufacture. Proc LAMP 87, May 1987, pp523-528.

[10] M. Junaid, F. N. Khan, K. Rahman, M. N. Baig, Effect of laser welding process on the microstructure, mechanical, properties and residual stresses in Ti-5Al-2.5Sn alloy, Optics and Laser Technology, 97, (2017), 405-419.

[11] E. Delord, G. Sayegh, Laser Welding Production of Transmission Shafts for the Automobile Industry, Proc ISATA 92, June 1992, pp439-446.

[12] R. Oyyaravelu, P. Kuppan, N. Arivazhagan, Metallurgical and mechanical properties of laser welded high strength low alloy steel, Journal of Advanced Research, 7, (2016), 463–472

[13] G. Hopf, Power Train/Transmission Laser Beam Welding of Gears - A Proven Technology with Further Potential, Proc MIWL Seminar on Laser Fabrication for the Automotive Industry, October 1995.

[14] I. B. Allemanna, J. Kaufman, Laser Principles, Physical and Electronic Properties of Lasers, 42, (2011), 7–23.

[15] C. Breck Hitz J. Ewing Jeff Hecht, Introduction to Laser Technology, Fourth Edition, IEE PRESS, United States of America ,26 March 2012.

[16] A. A Mudassar, Laser Physics, First Edition, 2015.

[17] E. Cappello, Le lavorazioni industriali mediante laser di Potenza, Maggioli Editore, Milano, (2008).

[18] W. Steen, J. Mazumder, Laser Material Processing, Springer-Verlag, 4th, London (2010).

[19] Handbook of laser welding technologies, Woodhead Publishing Limited, (2013).

[20] Y. Ai, X. Shao, P. Jiang, P. Li, Y. Liu, W. Liu, Welded joints integrity analysis and optimization for fiber laser welding of dissimilar materials, Optics and Lasers in Engineering, 86, (2016), 62–74.

[21] I. Bunaziva, O. M. Akselsena, A. Salminenc, A. Unt, Fiber laser-MIG hybrid welding of 5 mm 5083 aluminum alloy, Journal of Materials Processing Technology, 233 (2016), 107–114.

[22] J. Sundqvist, Heat Conduction Effects During Laser Welding, Luleå University of Technology Department of Engineering Sciences and Mathematics, Sweden, 2015.

[23] A. Paul, T. Debroy, Free Surface Flow and Heat Transfer in Conduction Mode Laser Welding, Metallurgical Transactions B, 19, (1988), 851–858.

[24] X.F. Liu, C.B. Jia, C.S. Wu, G.K. Zhang, J.Q. Gao, Measurement of the keyhole entrance and topside weld pool geometries in keyhole plasma arc welding with dual CCD cameras, Journal of Materials Processing Technology, 248, (2017), 39–48.

[25] T. Sibillano, A. Ancona, V. Berardi, E. Schingaro, G. Basile , P.M. Lugara, Optical detection of conduction/keyhole mode transition in laser welding, Journal of Materials Processing Technology, 191 (2007), 364–367.

[26] J. Svenungsson, I. Choqueta, A. F. H. Kaplan, Laser welding process – a review of keyhole welding modelling, Physics Procedia, 78, (2015), 182 – 191.

[27] S. Pang, X. Chen, X. Shao, S. Gong, J. Xiao, Dynamics of vapour plume in transient keyhole during laser welding of stainless steel: Local evaporation, plume swing and gas entrapment into porosity, Optics and Lasers in Engineering, 82, (2016), 28–40.

[28] J. Wang, R. Hu, X. Chen, S. Pang, Modeling fluid dynamics of vapor plume in transient keyhole during vacuum electron beam welding, Vacuum, 157, (2018), 277–290.

[29] M. Mazar Atabaki, N. Yazdian, R. Kovacevic, Partial penetration laser-based welding of aluminum alloy (AA 5083-H32), Optik, 127, (2016), 6782–6804.

[30] Z. M. Liua, Y. X. Fang, S. L. Cui, Z. Luo, W. D. Liu, Z. Y. Liu, Q. Jiang, S. Yi, Stable keyhole welding process with K-TIG, Journal of Materials Processing Technology, 238, (2016), 65–72.

[31] Z. M. Liu, Y. X. Fang, S. L. Cui, S. Yi, J. Y. Qiu, Q. Jiang, W. D. Liu, Z. Luo, Keyhole thermal behavior in GTAW welding process, International Journal of Thermal Sciences, 114, (2017), 352-362.

[32] J. Volpp, F. Vollertsen, Keyhole stability during laser welding—part I: modeling and evaluation, Production Engineering, 10, 2016, 443–457.

[33] J. Volpp, F. Vollertsen, Modeling keyhole oscillations during laser deep penetration welding at different spatial laser intensity distributions, Production Engineering, 9, (2015), 167–178.

[34] J. Kroos, U. Gratzke, G. Simon, Towards a self-consistent model of the keyhole in penetration laser beam welding, Journal of Physics D: Applied Physics, 26, (1993), 474-480.

[35] T. Kleint, M. Vicanekt, J. Kroosz, I. Deckers and G. Simont Oscillations of the keyhole in penetration laser beam welding J. Phys. D: Appt. Phys, 27, (1994), 2023-2030.

[36] R, Fabbro, S. Slimani, C. Frederic, F. Briand, Study of keyhole behaviour for full penetration Nd–Yag CW laser welding, Journal of Physics D Applied Physics, 38, (2005), 1881-1887.

[37] M. Chamim, Triyono, K. Diharjo, Effect of Electrode and Weld Current on The Physical and Mechanical Properties of Cast Iron Welding, International Conference on Engineering, Science and Nanotechnology, 2017.

[38] W. F. Savage, E. F. Nippes, E. S.Szekeres, A study of weld interface phenomena in a low alloy steel, Welding Research Supplement, 55, (1976), 260s–268s.

[39] J. C. Lippold, Welding Metallurgy and Weldability, Wiley, United States of America, 2005.

[40] E. J. Lavernia, T. S. Srivatsan, The rapid solidification processing of materials: science, principles, technology, advances, and applications, Journal of Materials Science, 45, (2010), 287–325.

[41] W. A. Tiller, K.A. Jackson, J. W. Rutter, B. Chalmers, The redistribution of solute atoms during the solidification of metals, Acta Metallurgica, 1, (1953), 428-437.

[42] M.C. Flemings, Solidification Processing, New York, McGraw Hill, 1974.

[43] W. Kurz, D.J. Fisher, Fundamentals of Solidification, Aedermannsdorf, Switzerland, Trans-Tech. Publications, 1986.

[44] J. Devletian, W. Woo, Weld Solidification, Metals Handbook, 6, (1983), 22-49.

[45] S. Kou, Welding Metallurgy, Wiley-VCH, 2003.

[46] S. Kou, Y. Le, Welding Parameters and the Grain Structure of Weld Metal A Thermodynamic Consideration, Metallurgical Transaction A, 19A, 1988-1075.

[47] S. Kou, Y. Le, Welding parameters and the grain structure of weld metal — A thermodynamic consideration, Metallurgical and Materials Transactions A, 19, 1075-1082.

[48] M. Kato, F. Matsuda, T. Senda, Weld. Res. Abroad, 19, (1973), 26.

[49] Y. Arata, F. Matsuda, A. Matsui, Trans. Jpn.Weld. Res. Inst., 3: 89, 1974

[50] T. Ganaha, B. P. Pearce, H.W. Kerr, Grain Structures in Aluminum Alloy GTA Welds, Metallurgical Transactions A, 11, (1980), 1351–1359.

[51] S. Kou, Y. Le, unpublished research, University of Wisconsin, Madison, 1985.

[52] S. Katayama, Formation mechanisms and preventive procedures of laser welding defects', 2004 LMP Symposium on High Quality and New Trend of Laser Welding, Laser Materials Processing (LMP) Research Committee of Japan Welding Engineering Society (JWES), January, (2015) 8-1–8-15 (in Japanese).

[53] Katayama S and Matsunawa A (1998) 'Laser weldability of aluminum alloys', Proc. 43rd Laser Materials Processing Conference, Japan Laser Processing Society (JLPS), 43, 33–52 (in Japanese).

[54] W. Dongsheng, X. Hua, L. Fang, L. Huang, Understanding of spatter formation in fiber laser welding of 5083 aluminum alloy, International Journal of Heat and Mass Transfer, 113, (2017), 730–740.

[55] S. Katayama Solidification phenomena of weld metals (2) – Solidification theory, solute redistribution and microsegregation', J. Light Metal Welding & Construction, 38(4), (2000) 168–180 (in Japanese).

[56] S. Katayama, Laser welding of dissimilar materials, The Review of Laser Engineering, (2010), 38(8), 594–602 (in Japanese).

[57] P. Vondrous, S. Katayama, J. Dunovsky, Specifics of laser welding of ductile iron, Cr-Mo steel and their dissimilar butt joints, Proc. 74th Laser Materials Processing Conference, JLPS, (2010) 74, 89–98.

[58] S. Katayama, Solidification phenomena of weld metals (3) – Mechanism and susceptibility of solidification cracking', J. Light Metal Welding & Construction, (2000), 38(9), 417–427 (in Japanese).

[59] R. Oyyaravelu, P. Kuppan, N. Arivazhagan, Metallurgical and mechanical properties of laser welded high strength low alloy steel, Journal of Advanced Research, 7, (2016), 463–472.

[60] Mandal, N. R., Aluminum Welding, 1st edition, Narosa Publishing House, pp. 1-19 Martukanitz, R. P., Smith, D. J. (1995) Laser beam welding of aluminum alloys. Proc 6th Int. Conf. on Aluminum Weldments, (2002) AWS, pp. 309-323.

[61] Duley, W. W., Laser Welding, 1st edition, John Wiley & Sons, Inc., (1999) pp. 4-65.

[62] G. Casalino, M. Mortello, P, Peyre, Yb–YAG laser offset welding of AA5754 and T40 butt joint, Journal of Materials Processing Technology, 223, (2015), 139–149.

[63] G. Casalino, M, Mortello, Modeling and experimental analysis of fiber laser offset welding of Al-Ti butt joints, International Journal of Advanced Manufacturing Technology, 83, (2016), 89–98.

[64] L. Karagiannis, G. Chryssolouris, Nd:YAG laser welding: an overview, Third GR-I international conference on new laser technologies and applications, Proceedings of SPIE, San Diego, CA, United States, 2003.

[65] D. R. G. Achar, J. Ruge, S. Sundaresan, Metallurgical and mechanical investigations of aluminum-steel fusion welds, Aluminum, 56(6), (1980),391–397.

[66] M.J. Torkamany, S. Tahamtan, J. Sabbaghzadeh, Dissimilar welding of carbon steel to 5754 aluminum alloy by Nd:YAG pulsed laser. Material Design, 2010, 31, 458–465.

[67] H. Oikawa, S. Ohimiya, T. Yoshimura, T. Saitoh, Resistance spot welding of steel and aluminum sheet using insert metal sheet. Science Technoly Welding Joining, 1999, 4, 80–88.

[68] M. Gao, C. Chen, S.W. Mei, L. Wang, X.Y. Zeng, Parameter optimization and mechanism of laser–arc hybrid welding of dissimilar Al alloy and stainless steel, The International Journal of Advanced Manufacturing Technology, 2014, 74, 199–208.

[69] G. Casalino, S. D'Ostuni, P. Guglielmi, P. Leo, G. Palumbo, A. Piccininni, Off-Set and Focus Effects on Grade 5 Titanium to 6061 Aluminum Alloy Fiber Laser Weld, Materials 2018, 11, 2337.

[70] G. Casalino, P. Guglielmi, V.D. Lorusso, M. Mortello, P. Peyre, D. Sorgente, Laser offset welding of AZ31B magnesium alloy to 316 stainless steel, Journal of Materials Processing Technology, 2017, 242, 49–59.

[71] J. Tusek, M. Suban, Hybrid welding with arc and laser beam, Science and Technology of Welding and Joining, 4, (1999), 308-311.

[72] A. Mahrle, E. Beyer, Hybrid laser beam welding – Classification, characteristics, and applications, Journal of Laser Applications, 18, (2006), 169-180.

[73] W.M. Steen, Arc-augmented laser processing of materials, Journal of Applied Physics, 51, (1980), 5636–5641.

[74] B. Hu, I.M. Richardson, Microstructure and mechanical properties of AA7075(T6) hybrid laser/GMA welds, Material Science Engineering A, 459, (2007),94-100,

[75] Z. L. Feng, Processes and mechanisms of welding residual stress and distortion, Woodhead Publishing Ltd, Cambridge, England, 2005.

[76] A. Fellman, V. Kujanpaa, The effect of shielding gas composition on welding performance and weld properties in hybrid CO_2 laser-gas metal arc welding of carbon manganese steel, Journal of Laser Applications, 18, (2006), 12–20,.

[77] P. T. Swanson, C. J. Page, E. Read, H. Z. Wu, Plasma augmented laser welding of 6 mm steel plate, Science and Technology of Welding & Joining, 12,(2007), 153–160,.

[78] E. A. Metzbower, P. E. Denney, D. W. Moon, C. R. Feng, S.G. Lambrakos, Thermal analysis and microharness maping in hybrid laser welds in a structural steel, Materials Science Forum, 426-432, (2003), 4147-4152.

[79] S. Katayama, S. Uchiumi, M. Mizutani, J. Wang, K. Fujii, Penetration and porosity prevention mechanism in YAG laser-MIG hybrid welding', Welding International, 21, (2007), 25–31,.

[80] M. Eboo, W.M. Steen, J. Clarke, Arc-augmented laser welding, Advances in Welding Processes, Proc. of the 4th Int. Conf., Harrogate, UK, (1978), 257–265.

[81] W. M. Steen, M. Eboo. Arc augmented laser welding, Metal Construction, 11, (1979), 332– 335.

[82] C. Bagger, F.O. Olson, Review of laser hybrid welding, Journal of Laser Applications, 17, (2005), 2-14.

[83] K. Nilsson, S. Heimbs, H. Engström, A.F.H. Kaplan, Parameter influence in CO2-laser/MIG hybrid welding, in: Proc. of 56th Annual Assembly of the International Institute of Welding, Bucharest, Romania, 2003, IIW Doc. IV- 843-03.

[84] R. Li, Z. Li, Y. Zhua, L. Ronga, A comparative study of laser beam welding and laser–MIG hybrid welding of Ti–Al–Zr–Fe titanium alloy, Material Science Engineering A 528, (2011) 1138–1142.

[85] L.J. Zhang, J. Ning, X.J. Zhang, G.F. Zhang, J.X. Zhang, Single pass hybrid laser– MIG welding of 4-mm thick copper without preheating, Material Design, 74,(2015), 1–18.

[86] D.Y. Kim, Y.W. Park, Weldability evaluation and tensile strength estimation model for aluminum alloy lap joint welding using hybrid system with laser and scanner head, Transactions of Nonferrous Metals Society of China, 22,(2012), 596–s604.

[87] M. Gao, X.Y. Zeng, Q.W. Hu, Effects of welding parameters on melting energy of CO2 laser-GMA hybrid welding, Science and Technology of Welding and Joining, 11 (5) (2006) 517–522.

[88] L. Bidia, P.L. Masson, E. Cicala, C. Primault, Experimental design method to the weld bead geometry optimization for hybrid laser-MAG welding in a narrow chamfer configuration, Optics & Laser Technology, 89, (2017), 114–125.

[89] Z. Gao, X. Shao, P. Jiang, L. Cao, Q. Zhou, C. Yue, Y. Liu, C. Wang, Parameters optimization of hybrid fiber laser-arc butt welding on 316L stainless steel using Kriging model and GA, Optics & Laser Technology, 83, (2016), 153–162.

[90] Z. Shenghai, S. Yifu, Q. Huijuan, The technology and welding joint properties of hybrid laser-TIG welding on thick plate, Optics & Laser Technology,48,(2013), 381– 388.

[91] E.L. Guen, R. Fabbro, M. Carin, F. Coste, P.L. Masson, Analysis of hybrid Nd: Yag laser-MAG arc welding processes, Optics & Laser Technology, 43, (2011), 1155–1166.

[92] L. Bidi, S. Mattei, E. Cicala, H. Andrzejewski, P.L. Masson, J. Schroeder, The use of exploratory experimental designs combined with thermal numerical modeling to obtain a predictive tool for hybrid laser/MIG welding and coating processes, Optics & Laser Technology,43, (2011), 537–545.

[93] G. Casalino, S.L. Campanelli, U.D. Maso, A.D. Ludovico, Arc leading versus laser leading in the hybrid welding of aluminum alloy using a fiber laser, in: Proc. of 8th CIRP Conference on Intelligent Computation in Manufacturing Engineering, (2013), 151–156.

[94] S. Liu, Y. Li, F. Liu, H. Zhang, H. Ding, Effects of relative positioning of energy sources on weld integrity for hybrid laser arc welding, Optics and Lasers in Engineering, 81, (2016), 87–96.

[95] P. Kah, A. Salminen, J. Martikainen. The influence of parameters on penetration, speed and bridging in laser hybrid welding, MECHANIKA. 17, (2011), 324-333.

[96] W. Zhang, X. Hua, W. Liao, F. Li, M. Wang, The effect of the welding direction on the plasma and metal transfer behavior of CO2 laser + GMAW-P hybrid welding processes, Optics and Lasers in Engineering, 58, (2014), 102–108.

[97] Shuangyu Liu, Yanqing Li, Fengde Liu, Hong Zhang, Hongtao Ding, Effects of relative positioning of energy sources on weld integrity for hybrid laser arc welding, Optics and Lasers in Engineering, 31, (2016) 87-96.

[98] M.M. Atabaki, M. Nikodinovski, P. Chenier, J. Maa, W. Liu, R. Kovacevic, Experimental and numerical investigations of hybrid laser arc welding of aluminum alloys in the thick T-joint configuration, Optics & Laser Technology, 59, (2014), 68–92.

[99] S. Liu, F. Liu, H. Zhang, Y. Shi, Analysis of droplet transfer mode and forming process of weld bead in CO2 laser–MAG hybrid welding process, Optics & Laser Technology, 44, (2012), 1019–1025.

[100] L. Liu, R. Xu, Investigation of corrosion behavior of Mg-steel laser-TIG hybrid lap joints, Corrosion Science, 54, (2012), 212–218.

[101] L. Liu, X. Hao, G. Song, A new laser-arc hybrid welding technique based on energy conservation, Materials Transactions, 47, (2006), 1611–1614.

[102] K. Zhang, Z. Lei, Y. Chen, M. Liu, Y. Liu, Microstructure characteristics and mechanical properties of laser-TIG hybrid welded dissimilar joints of Ti– 22Al–27Nb and TA15, Optics & Laser Technology, 73, (2015), 139–145.

[103] M. Gao, X. Zeng, Q. Hu, Effects of gas shielding parameters on weld penetration of CO2 laser-TIG hybrid welding, Journal of Materials Processing Technology, 184, (2007), 177–183.

[104] W. Piekarska, M. Kubiak, Three-dimensional model for numerical analysis of thermal phenomena in laser–arc hybrid welding process, International Journal of Heat and Mass Transfer, 54, (2011), 4966–4974.

[105] S. Yan, Y. Nie, Z. Zhu, H. Chen, G. Gou, J. Yu, G. Wang, Characteristics of microstructure and fatigue resistance of hybrid fiber laser-MIG welded Al–Mg alloy joints, Applied Surface Science, 298, (2014), 12–18.

[106] M.M. Alam, Z. Barsoum, P. Jonsen, A.F.H. Kaplan, H.A. Haggblad, The influence of surface geometry and topography on the fatigue cracking behaviour of laser hybrid welded eccentric fillet joints, Applied Surface Science, 256, (2010), 1936– 1945.

[107] S. Liu, F. Liu, C. Xu, H. Zhang, Experimental investigation on arc characteristic and droplet transfer in CO2 laser–metal arc gas (MAG) hybrid welding, International Journal of Heat and Mass Transfer, 62, (2013), 604–611.

[108] E.L. Guen, M. Carin, R. Fabbro, F. Coste, P.L. Masson, 3D heat transfer model of hybrid laser Nd:Yag-MAG welding of S355 steel and experimental validation, International Journal of Heat and Mass Transfer, 54, (2011), 1313–1322.

[109] J. Frostevarg, A.F.H. Kaplan, Undercuts in laser arc hybrid welding, Physics Procedia, 56, (2014), 663–672.

[110] L. Liu, X. Hao, Improvement of laser keyhole formation with the assistance of arc plasma in the hybrid welding process of magnesium alloy, Optical Lasers Engineering, 47, (2009), 1177–1182.

[111] Z. Shenghai, S. Yifu, Q. Huijuan, The technology and welding joint properties of hybrid laser-tig welding on thick plate, Optics & Laser Technology, 48, (2013), 381–388.

[112] E. Le Guen, R. Fabbro, M. Carin, F. Coste, P. Le Masson, Analysis of hybrid Nd:Yag laser-MAG arc welding processes, Optics & Laser Technology,43,(2011), 1155–1166.

[113] L. J. Zhang, J. Ning, X. J. Zhang, G. F. Zhang, J. X. Zhang, Single pass hybrid laser–MIG welding of 4-mm thick copper without preheating, Materials and Design, 74, (2015), 1–18.

[114] L. Bidi, S. Mattei, E. Cicala, H. Andrzejewski, P. Le Masson, J. Schroeder, The use of exploratory experimental designs combined with thermal numerical modelling to obtain a predictive tool for hybrid laser/MIG welding and coating processes, Optics & Laser Technology, 43, (2011), 537–545.

[115] H. S. Bang, Y. C. Kim, H. S. Bang, S. M. Joo, Analysis of residual stress on AH32 butt joint by hybrid CO2 laser-GMA welding, Computational Materials Science, 49, (2010), 217-221.

[116] F. Kong, J. Ma, R. Kovacevic, Numerical and experimental study of thermally induced residual stress in the hybrid laser–GMA welding process, Journal of Materials Processing Technology, 211, (2011), 1102-1111.

[117] T. Liu, F. Yan, S. Liu, R. Li, C. Wang, X. Hu, Microstructure and mechanical properties of laser-arc hybrid welding joint of GH909 alloy, Optics & Laser Technology,80, (2016), 56–66.

[118] I. Bendaoud, S. Matteï, E. Cicala, I. Tomashchuk, H. Andrzejewski, P. Sallamand, A. Mathieu, F. Bouchaud, The numerical simulation of heat transfer during a hybrid laser–MIG welding using equivalent heat source approach, Optics & Laser Technology, 56, (2014), 334–342.

[119] P. Leo, G. Renna, G. Casalino, A.G. Olabi, Effect of power distribution on the weld quality during hybrid laser welding of an Al–Mg alloy, Optics & Laser Technology, 73, (2015), 118–126.

[120] B. Acherjee, Hybrid laser arc welding: State-of-art review, Optics and Laser Technology, 99 (2018) 60–71.

[121] E. Le Guen, R. Fabbro, M. Carin, F. Coste, P. Le Masson, Analysis of hybrid Nd:Yag laser-MAG arc welding processes, Optics & Laser Technology, 43, (2011), 1155-1166

[122] P. Leo, S. D'Ostuni, G. Casalino, Hybrid welding of AA5754 annealed alloy: Role of post weld heat treatment on microstructure and mechanical properties, Materials and Design 90 (2016) 777–786.

[123] P. Russo Spena, P. Matteis, G. Scavino Dissimilar Metal Active Gas Welding of TWIP and DP Steel Sheets, Steel Reserch Internetional Journal, (2015), 495-501.

[124] F. Cappelli, V. Boneschi, P. Viganò, Vehicle architectures: evolution towards improved safety, low-weight, ergonomics and flexibility, 9th International Conference & Exhibition, FLORENCE ATA 2005.

[125] E.I. Aniekan, O. E. Kelly, G. Abdulsamad, Engineering Material Selection for Automotive Exhaust Systems Using CES Software, INTERNATIONAL JOURNAL of ENGINEERING TECHNOLOGIES-IJET, Vol.3, No.2, 2017.

[126] J. B. Emmons, L. J. Blessing, Ultralight Stainless steel Urban Bus Concept, SAE TECHNICAL PAPER SERIES, Washington, D.C. May 14-16, 2001.

[127] HT. Lee, SL. Jeng, Characteristics of dissimilar welding of alloy 690 to 304L stainless steel. Science Technology Welding Joining, (2001), 6(4), 225-234.

[128] AH. Jamshidi, A. Farzadi, S. Serajzadeh, AH. Kokabi. Theoretical and experimental study of microstructures and weld pool geometry during GTAW of 304 stainless steel. The International Journal of Advanced Manufacturing Technology, (2009), 42(11-12): 1043–1051.

[129] S. Keeler, M. Kimchi, 2014 Advanced High Strength Steel Application Guidelines Version 5.0. WorldAutosteel.

[130] J. Fansi, Prediction of DP steel fracture by FEM simulationsusing an advanced Gurson model, These, university of Liege, 2013.

[131] S. Liu, Numerical and experimental study on residual stresses in laser beam welding of dual phase DP600 steel plates, Hal archives-ouvertes.

[132] M. K. Singh, Application of Steel in Automotive Industry, International Journal of Emerging Technology and Advanced Engineering, Volume 6, Issue 7, July 2016.

[133] P. Russo Spena, F. D'Aiuto, P. Matteis, G. Scavino, Dissimilar Arc Welding of Advanced High Strength Car-Body Steel Sheets. Journal of Materials Engineering and Performance (2014) 23, 3949–3956.

[134] W.S. Miller, L. Zhuang, J. Bottema, A.J. Wittebrood, P. De Smet, A. Haszler, A. Vieregge, Recent development in aluminum alloys for the automotive industry, Materials Science and Engineering A280, (2000), 37–49.

[135] T. Sakurai, The Latest Trends in Aluminum Alloy Sheets for Automotive Body Panels, KOBELCO TECHNOLOGY REVIEW NO. 28 OCT. 2008.

[136] J. R. Hirsch, Aluminum Alloys for Automotive Application, Materials Science Forum, 242, (1997), 33-50.

[137] E. Romhany, M. Popovic, D. Glisic, M. Stefanovic, M. Milovanovic, On the Al-Mg alloy sheets for automotive application: Problems and solutions, January 2004.

[138] T.Y. Kuo, Lin, H.C. Effects of pulse level of Nd-YAG laser on tensile properties and formability of laser weldments in automotive aluminum alloys, Materials Science & Engineering A: Structural, (2006) 416, 281–289.

[139] J.M. Sánchez-Amaya, T. Delgado, J.J. De Damborenea, V. López, F.J. Botana, Laser welding of AA 5083 samples by high power diode laser, Science and Technology of Welding and Joining, 14(1), (2009) 78–86.

[140] O. Hiroaki, M.E. Schlesinger, E.M. Mueller, Alloy Phase Diagrams, 3rd ed.; ASM International: Geauga County, OH, USA, 1992;

[141] F. Kong, J. Ma, R. Kovacevic, Numerical and experimental study of thermally induced residual stress in the hybrid laser–GMA welding process, Journal of Materials Processing Technology, 211, (2011), 1102–1111.

[142] J. R. Chukkana, M. Vasudevan, S. Muthukumaran, R. Ravi Kumar, N. Chandrasekhar, Simulation of laser butt welding of AISI 316L stainless steel sheet using various heat sources and experimental validation, Journal of Materials Processing Technology, 219,(2015), 48–59.

[143] F. Farrokhi, B. Endelt, M. Kristiansen, A numerical model for full and partial penetration hybrid laser welding of thick-section steels, Optics and Laser Technology, 111, (2019), 671–686.

[144] D. Radaj Heat Effects of Welding: Temperature Field, Residual Stress, Distortion: Springer-Verlag, 1992.

[145] M. Azizpour, M. Ghoreishi, A. Khorram, Numerical simulation of laser beam welding of Ti6Al4V sheet. Journal of Computational and Applied Research in Mechanical Engineering, 4, (2015), 145–154.

[146] J. Goldak, A. Chakravarti, M. Bibby. A New Finite Element Model for Welding Heat Sources, Metallurgical Transactions B, 15, (1984), 299-305.

[147] J. Goldak, M. Bibby, J. Moore, R. House, B. Patel. Computer Modeling of Heat Flow in Welds, Metallurgical Transactions B, 17, (1986), 587-600.

[148] F. Farrokhi, B. Endelt, M. Kristiansen, A numerical model for full and partial penetration hybrid laser welding of thick-section steels, Optics and Laser Technology, 111, (2019), 671–686.

[149] E. D. Derakhshan , N. Yazdian, B. Craft, S. Smith, R. Kovacevic, Numerical simulation and experimental validation of residual stress and welding distortion induced by laser-based welding processes of thin structural steel plates in butt joint configuration, Optics and Laser Technology, 104, (2018), 170–182.

[150] N. S. Shanmugam, G. Buvanashekaran , K. Sankaranarayanasamy , S. Ramesh Kumar, A transient finite element simulation of the temperature and bead profiles of T-joint laser welds, Materials and Design, 31, (2010),4528–4542.

[151] W. Piekarska, M. Kubiak, Three-dimensional model for numerical analysis of thermal phenomena in laser–arc hybrid welding process , International Journal of Heat and Mass Transfer, 54, (2011), 4966–4974.

[152] C. R. Xaviera, H. G. D. Juniorc, J. A. de Castro, An Experimental and Numerical Approach for the Welding Effects on the Duplex Stainless steel Microstructure, Materials Research, (2015).

[153] W. Liu, J. Ma, MM. Atabaki, R. Pillai, B. Kumar, U. Vasudevan, H. Sreshta, R.Kovacevic, Hybrid Laser-arc Welding of 17-4 PH Martensitic Stainless steel. Journal of Manufacturing and Materials Processing, (2015), 2(2), 74-90.

[154] ASM Handbook volume 6: Welding, Brazing and Soldering. 9th. USA; 1993.

[155] G. Casalino, P. Leo, M. Mortello, P. Perulli, A. Varone, Effects of Laser Offset and Hybrid Welding on Microstructure and IMC in Fe–Al Dissimilar Welding, Metals, 7, (2017), 282;

[156] G. Casalino, A. Angelastro, P. Perulli, K. Casavola, V. Moramarco, Study on the fiber laser/TIG weldability of AISI 304 and AISI 410 dissimilar weld, Journal of Manufacturing Processes, 35, (2018), 216-225

[157] A. H. Farajia, M. Moradi, M, Goodarzi, P. Colucci, C. Maletta. An investigation on capability of hybrid Nd:YAG laser-TIG welding technology for AA2198 Al-Li alloy, Optical Lasers Engineering, 96, (2017),1–6.

[158] M. Moradi, M. Ghoreishi, A. Khorram. Process and outcome comparison between laser, tungsten inert gas (TIG) and Laser-TIG hybrid welding. Lasers in Engineering, 39(3-6), (2018), 379–91.

[159] M. Gao, T. Cao, XY. Zeng, TX. Lin Mechanical properties and microstructures of hybrid laser MIG welded dissimilar Mg–Al–Zn alloy, Science Techonoly Welding Joining, 15, (2010) 638–45.

[160] P. Kah Overview of the exploration status of laser- arc hybrid welding processes, Reviews on Advanced Materials Science, 30, (2012), 112–32.

[161] M. Gao, XY. Zeng, QW. Hu, J. Yan, Weld microstructure and shape of laser-arc hybrid welding, Science Technoly Welding Joining, 13, (2008), 106–13.

[162] G. Casalino, M. Mortello, P. Leo, KY. Benyounis, AG. Olabi, Study on arc and laser powers in the hybrid welding of AA5754 Al-alloy, Material Design, 61, (2014),191–8.

[163] HU. Hong, BS. Rho, SW. Nam, A study on the crack initiation and growth from dferrite/ c phase interface under continuous fatigue and creep–fatigue conditions in type 304L stainless steel, International Journal of Fatigue, 24, (2002),1063–70.

[164] G. Casalino, F. Panella. Microstructural analysis of AISI 304 bars welded with high speed pulsed discharges. Journal of Materials Processing Technology, 191, (2007),149–52.

[165] M. Arivarasu, DR. Kasinath, A. Natarajan, Effect of continuous and pulsed current on the metallurgical and mechanical properties of gas tungsten arc welded AISI 4340 aeronautical and AISI 304 L austenitic stainless steel dissimilar joints, Materials Research, 18, (2015),59–77.

[166] MC. Tsai CS. Chiou, JS. Du R. Yang. Phase transformation in AISI 410 stainless steel, Materials Science and Engineering, A332, (2002), 1–10.

[167] JD. Tucker, TK. Nolan, AJ. Martin, GA. Young, Effect of travel speed and beam focus on porosity in alloy 690 laser welds, Journal of the Minerals, Metals, and Materials Society, (2012),64,1409–17.

[168] A. Matsunawa, JD. Kim, S. Katayama Porosity formation in laser welding-mechanisms and suppression methods. Int. Cong. on Applications of Lasers and Electro- Optics-ICALEO 1997:73–82. Miami, Fl.

[169] Y. Kawahito, M. Mizutani, S. Katayama, Elucidation of high power fiber laser welding phenomena of stainless steel and effect of factors on weld geometry, Journal of Physics D, 40, (2007),5854–9.

[170] H. Kyung-Min, C. S. Yung, Prospects of laser welding technology in the automotive industry: A review. Journal of Materials Processing Technology (2017) 245:46–69.

[171] K. Martinsen, S.J. Hu, B.E. Carlson, Joining of dissimilar materials. CIRP Annals - Manufacturing Technology, (2015) 64:679–699.

[172] G. Casalino, M. Mortello, S.L. Campanelli, Ytterbium fiber laser welding of Ti6Al4V alloy. Journal of Manufacturing Processes, (2015) 20: 250-256.

[173] G. Casalino, M. Mortello, Modeling and experimental analysis of fiber laser offset welding of Al-Ti butt joints. International Journal of Advanced Manufacturing Technology, (2016) 83:89-98.

[174] A. Angelastro, G. Casalino, P. Perulli, P. R. Spena, Weldability of TWIP and DP steel dissimilar joint by laser arc hybrid welding with austenitic filler, 11th CIRP Conference on Intelligent Computation in Manufacturing Engineering, CIRP ICME' 2017, Gulf of Naples, Italy

[175] L. Mujicaa, S. Weber, H. Pinto, C. Thomye, F. Vollertsene, Microstructure and mechanical properties of laser-welded joints of TWIP and TRIP steels. Materials Science and Engineering: A, 527, (2010), 2071–2078.

[176] M. Xia, E. Biro, Z. Tian, Y. Zhou, N. Effects of Heat Input and Martensite on HAZ Softening in Laser Welding of Dual Phase Steels. ISIJ International, 48, (2008) 809–814.

[177] K. Kunishige, N. Yamauchi, T. Taka, N. Nagao, Softening in Weld Heat Affected Zone of Dual Phase Steel Sheet for Automotive Wheel Rim. SAE International Congress and Exposition in Detroit, MI, 1983.

[178] G. Casalino, A. Angelastro, P. Perulli, P. Posa, P. R. Spena, Fiber laser-MAG hybrid welding of DP/AISI 316 and TWIP/AISI 316 dissimilar weld, Procedia CIRP 79, (2017), 153-158.

[179] D.A. Porter, Easterling, K.E. Phase Transformations in Metals and Alloys; Chapman & Hall: London, UK, 1992

[180] N. Farabi, D.L. Chena, Y. Zhou, Microstructure and mechanical properties of laser welded dissimilar DP600/DP980 dual-phase steel joints. Journal of Alloys and Compounds, 509, (2011), 982–989.

[181] J.R. Davis, Aluminum and Aluminum Alloys, 1st ed.; ASM International: Geauga County, OH, USA, 1993.

[182] S. Kumar, H.B. Nadendla, G.M. Scamans, D.G. Eskin, Z. Fan, Solidification behavior of an AA5754 alloy ingot cast with high impurity content, International Journal of Materials Research, 103, (2012), 1228–1234.

[183] W.F. Smith, Structure and Properties of Engineering Alloys, 1st ed.; McGraw-Hill: New York, NY, USA, 1992; pp. 186–191.

[184] M.J. Rathod, M. Kustuna, Joining of aluminum alloy 5052 and low carbon steel by laser roll welding. Welding Journal Research Supplement, 83, (2004), 16–26.

[185] Y.G. Miao, D.F. Han, J.Z. Yao, F.Li, Microstructure and interface characteristics of laser penetration brazed magnesium alloy and steel, Science and Technology of Welding and Joining, 15, 2010, 97–103.

[186] S. Kobayashi, T. Yakou, Control of intermetallic compound layers at interface between steel and aluminum by diffusion-treatment, Materials Science and Engineering: A, 338, 2002, 44–53.

[187] J. Sun, Q. Yan, W. Gao, J. Huang, Investigation of laser welding on butt joints of Al/steel dissimilar materials. Material Design, 83, 2015, 120–128.

[188] R. Qiu, H. Shi, K. Zhang, Y. Tu, C. Iwamotoc, S. Satonaka, Interfacial characterization of joint between mild steel and aluminum alloy welded by resistance spot welding, Materials Characterization, 61, 2010, 684–688.

[189] J. Yang, L.Y. Long, H. Zhang, Microstructure and mechanical properties of pulsed laser welded Al/steel dissimilar joint, Transactions of Nonferrous Metals Society of China, 26, 2016, 994−1002.

[190] N. Kumar, M. Mukherjee, A. Bandyopadhyay, Comparative study of pulsed Nd:YAG laser welding of AISI 304 and AISI 316 stainless steel. Optic Laser Technoly, 88, 2017, 24–39.

[191] J. Brooks, J. Lippold, Welding, Brazing, and Soldering, 1st ed.; ASM International: Geauga County, OH, USA, 1993.

[192] Welding, Brazing, and Soldering, ASM Handbook, Volume 6,1993

[193] N. S. Shanmugam, G. Buvanashekaran, K. Sankaranarayanasamy, S. R. Kumar, A transient finite element simulation of the temperature and bead profiles of T-joint laser welds, Material Design, (2010), 31,4528–4542.

[194] E. D. Derakhshan, N. Yazdian, B. Craft, S. Smith, R. Kovacevic, Numerical simulation and experimental validation of residual stress and welding distortion induced by laser-based welding processes of thin structural steel plates in butt joint configuration, Optical Laser Technology, (2018), 104, 170–182.

[195] W. Piekarska, M. Kubiak, Three-dimensional model for numerical analysis of thermal phenomena in laser–arc hybrid welding process , International Journal of Heat and Mass Transfer, (2011), 54, 4966–4974.

[196] Z.; Gao, P. Jiang, G. Mi, L. Cao, W. Liu, Investigation on the weld bead profile transformation with the keyhole and molten pool dynamic behavior simulation in high power laser welding, International Journal of Heat and Mass Transfer, (2018**)**, *116*, 1304-1313.

[197] G.A. Moraitis, G.N. Labeas, Prediction of residual stresses and distortions due to laser beam welding of butt joints in pressure vessels, International Journal of Pressure Vessels and Piping. (2009), *86*, 133–142.

[198] Nezamdost, M. R.; Nekouie Esfahani, M. R.; Hashemi, S. H.; Mirbozorgi, S. A.; Investigation of temperature and residual stresses field of submerged arc welding by finite element method and experiments, International Journal of Heat and Mass Transfer, (2016), 87, 615–624

[199] M. C. Padgett, Phase Transformations During Cooling of Automotive Steels, a Thesis, TUSCALOOSA, ALABAMA.

[200] AA. Bhatti, B. Zuheir, M. Hidekazu, B. Imad, Influence of thermo-mechanical material properties of different steel grades on welding residual stresses and angular distortion, Material and Design, 65, (2015), 878–889.

[201] G. Casalino, M. Dassisti, P. Perulli, FEM model for TIG hybrid laser butt welding of 6 mm thick austenitic to martensitic stainless steel, 13th CIRP Conference on Intelligent Computation in Manufacturing Engineering, 17-19 July 2019, Gulf of Naples, Italy.

[202] M. Azizpour, M. Ghoreishi, A. Khorram. Numerical simulation of laser beam welding of Ti6Al4V sheet JCARME, (2014) 4: 145-154.

[203] V. Harinadh, G. Edison, A. Suresh, KB. Ramesh, Simulation of hybrid laser-TIG welding process using FEA. JESTEC (2018), 13:1782 – 1792.

[204] R. Swapnil, Deogade, Prof. Sachin P, Ambade, Dr. Awanikumar P. Finite Element Analysis of Residual Stresses on Ferritic Stainless steel using Shield Metal Arc Welding, IJERGS (2015), 3(2).

[205] https://steelselector.sij.si/steels/PK330.html.